optimization and integration of bio-inspired anodesin a platinum-free pemfc

Nathan Coutard

THÈSE

Pour obtenir le grade de

DOCTEUR DE L'UNIVERSITÉ GRENOBLE ALPES

Spécialité : **Chimie inorganique et bio-inorganique**

Arrêté ministériel : 7 août 2006

Présentée par

Nathan Coutard

Thèse dirigée par **Vincent Artero**

préparée au sein du **Laboratoire de Chimie et Biologie des Méta** dans **l'École Doctorale de Chimie et Sciences du Vivant**

Optimisation et intégration d'anodes bio-inspirées dans une pile à combustible sans platine

Optimization and integration of bio-inspired anodes in a platinum-free fuel cell

Thèse soutenue publiquement le **28 septembre 2018** devant le jury composé de :

Mme. Elena Savinova
Professeure, Université de Strasbourg, Rapportrice
Mme. Kylie Vincent
Professeure, University of Oxford, Rapportrice
Mme. Carole Duboc
Directrice de recherche, Université Grenoble Alpes, Présidente du jury
M. Frédéric Jaouen
Chargé de recherche, Université de Montpellier, Examinateur
M. Vincent Artero
Directeur de recherche, CEA, Directeur de thèse
Mme. Pascale Chenevier
Chercheure, CEA, Membre invitée

Voici l'heure des remerciements qui arrivent non par ordre d'importance ni même suivant une quelconque convention savamment préétablie, mais dans l'ordre auquel j'ai pensé à vous, ce qui n'est sans doute pas aussi innocent que ce que l'on pourrait souhaiter. J'ai quand même gardé Vincent pour la fin et le suspens… A ma famille, que nous vîmes cinq mille en arrivant dans la salle de soutenance, je vous dirai peut-être ce que je pense ce soir en mangeant de l'aligot. Je vous aime tous. Marianne, heureusement que t'étais là parce que putain sans une amie trois ans ça aurait été long, dur, chiant et terriblement sobre. Merci pour tout ce bonheur. Henry David Thoreau dit qu'il suffit grosso modo de 4 trucs sur terre : la bouffe, le feu, les vêtements et une maison. Alors jsuis pas mal d'accord avec lui, mais je pense qu'il passe à côté de l'essentiel. Et l'essentiel, c'est les occupants de la maison parce qu'une baraque vide c'est déprimant. Thomas, Nico, Marie, Cécile et Arthur : on a partagé tellement plus qu'un loyer. Des bières principalement. Aux p'tits copains dits « de la pause-café » : Sarah, Steve, Chloé (petit ange parti trop tôt) et Lulu : un burne-out c'est quoi déjà ? Merci. Merci d'avoir été un public patient et attentif, merci pour la bouffée d'air frais qui rend possible le travail acharné des heures vespérales, inhérent à la recherche presque publique et merci d'éteindre la lumière en partant le vendredi. Jojo, merci pour les conseils rando et les câbles, pétés tout en douceur, allant en s'intensifiant vers la fin de nos contrats respectifs. Un jour on ira marcher ensemble, peut-être ? Pour des déjeuners toujours agréables passés à parler dans 14 langues simultanément, je tiens à remercier Jaione et Marila. J'espère que vous allez survivre à votre séparation imminente. Olivier, Steph Torelli et Lulu merci pour les conseils bricolage et les bons plans de fournisseurs, ça fait plaisir de causer avec des gens qui font des choses. Caroline, merci pour les conseils vestimentaires et capillaires mais jsuis majeur et vacciné et je fais ce que je veux avec mon ptit corps. A tout SolHyCat, merci pour un labo agréable et pour des discussions scientifiques de haut vol. Merci à Jenni et Adina pour toute l'aide logistique et de rendre tout facile tous les jours chez SolHyCat. C'est fou à quel point ça change la vie quand un labo tourne comme une machine bien huilée. Murielle, désolé de pas aimer la mousse au chocolat mais merci d'avoir essayé, merci pour les discussions scientifiques de haut vol. Matthieu, bravo, presque 3 ans dans le même bureau que moi c'est pas tout le monde qui survit pour en parler. Et tu n'as eu besoin de déménager qu'une fois ! Désolé pour les chants de Noël en russe et les guirlandes épileptiques. Prends soin des plantes quand je serai parti. Toutes les plantes. Pas seulement celle que tu aimes. Ne laisse pas mourir mon sapin moche. Bertrand, tu me rappelles Georges politiquement. Tim, thanks for brexit. Was about time. Nick, thanks for major pop culture enhancing discussions. Stéphane Ménage, futur ex-directeur du meilleur LCBM, mort à l'intérieur durant l'exercice de ses fonctions, merci pour votre sacrifice vous ne serez pas oublié. Roger, de la part des presque 80 personnes non concernées mais contactées par courrier électronique, tout le monde s'en fout de qui a pissé dans une centrifugeuse au bâtiment K. Nico et Nico, merci pour le flambeau, j'ai essayé d'être en même temps parisien, impertinent, grand et niais, de mauvaise foi quand ça m'arrange, électrochimiste, spécialiste des machins rugueux qui marchent pas et des blagues de mauvais goût et surtout un mec sympa. J'ai fait de mon mieux et j'espère que ça passe, si ça passe pas c'est le même tarif de toute façon. Juju, merci pour les duos lyriques et les conseils avisés concernant à peu près tout. Et la culture footballistique. Parce qu'une famille normale selon Christine Boutin c'est un papa et une maman, Pascale tu fus tout ce que Vincent ne pouvait pas être. Intelligente, brillante, disponible, intéressée et intéressante. Si je peux me permettre un conseil maintenant que je suis docteur ? Continue à t'intéresser à tout, tout le temps. C'est malheureusement pas valorisé par les hautes sphères de financement de la recherche publique, mais c'est tellement nécessaire. Vincent, merci de m'avoir fait confiance. Je partais pas gagnant avec ma photo de profil skype mais j'espère avoir été à la hauteur. Jsuis assez content d'avoir réussi à te faire faire des trucs que tu ne comprenais pas complètement, parce que dieu sait que c'est rare les choses que tu ne comprends pas. Merci d'avoir été tout ce qu'on est en droit d'attendre d'un directeur de thèse, et je ne ferai pas d'inventaire car je n'ai pas la plume de Pérec ou Prévert, mais aussi d'avoir été beaucoup de ce qu'on peut attendre d'un ami. J'ai vu autour de moi des doctorants pas contents, je suis tombé au mieux. Ce mélange en proportions toujours bien dosées d'encadrement et de liberté qui fait les grands mentors. Tu serais parfait si t'étais pas en marche. Merci pour trois ans de science et plus car affinités. A tous les autres, désolé de vous avoir oubliés mais merci, merci mille fois merci de ne pas m'en tenir rigueur, c'est vraiment sympa.

"Que diable allait-il faire dans cette galère ?"

Molière, *Les fourberies de Scapin*, **II**, 7

"I'm being quoted to introduce
something, but I have no idea what
it is and certainly don't endorse it."

Randall Munroe

Illustration on previous page © Bill Waterson

Abbreviations

atm.: atmospheric

BET: Brunauer-Emmett-Teller

Cy: cyclohexyl

CV: cyclic voltammetry

DCM: dichloromethane

dist.: distilled

DMF: N,N-dimethylformamide

DMSO: dimethylsulfoxide

EDX: energy-dispersive X-ray specroscopy

EIS: electrochemical impedance spectroscopy

equiv.: equivalent

EXAFS: extended X-ray absorption fine structure

$E_{1/2}$: mid-wave potential

GCE: glassy carbon electrode

GDL: gas diffusion layer

Gly: glycine

HER: hydrogen evolution reaction

HEPES: 2-[4-(2-hydroxyethyl)piperazin-1-yl]ethanesulfonic acid

HOR: hydrogen oxidation reaction

HRTEM: high-resolution transition electron microscopy

LSV: linear sweep voltammetry

MEA: membrane-electrode assembly

MeCN: acetonitrile

MES: 2-(N-morpholino)ethanesulfonic acid

MWNT: multi-wall carbon nanotube

NHE: normal hydrogen electrode

NMR: nuclear magnetic resonance

ORR: oxygen reduction reaction

PEIS: potentiostatic electrochemical impedance spectroscopy

PEM: proton-exchange membrane

PEMFC: proton-exchange membrane fuel cell

PGM: platinum group metals

Ph: Phenyl

ppm: parts per million

RT: room temperature

SEM: scanning electron microscopy

SWNT: single-wall carbon nanotube

TEM: transition electron microscopy

TOF: turnover frequency

TOF_{max}: maximum turnover frequency

TON: turnover number

XANES: x-ray absorption near edge structure

XAS: X-ray absorption spectroscopy

Constants

F: faraday constant (96485 $C \cdot mol^{-1}$)

R: ideal gas constant (8.314 $J \cdot K^{-1} \cdot mol^{-1}$)

Preamble

In a never-ending, exponentially growing thirst for expansion and technological improvements originating with the first tool and snowballing since the industrial revolution, mankind seems to have placed itself in a bit of a pickle. We are going to need much more than what the exploitable universe has to offer to quench that thirst. Our global economy model, based on unending growth, is not viable with our limited natural resource and before we run out of breathable air and start worrying about much more serious problems, we will start running out of fossil fuels. They seemed an unlimited amount of energy even a few decades ago, easily accessible, set aside for us with a kind thought by cyanobacteria, plants and dinosaurs over millions of years. As it turns out, they are neither unlimited nor very easily regenerated unless you have a couple millions of years and a couple millions of dinosaurs on hand. Nuclear energy is not sustainable either. It could be viable over the next hundreds of years if we knew how to get rid of the waste, but sending it to space is not economically viable and burying it, even very deep, in third-world countries is hopefully not going to be acceptable forever. Sustainable energy sources such as sunlight or wind inundate our planet with large amounts of easy to harvest energy and present an obvious alternative to nuclear and fossil fuels. One of the inconveniences of those green energy sources is their inherently intermittent nature, which creates a requirement for new energy vectors, that need to be both energy-dense to be used in the transportation sector and easily produced in a user-friendly state, to allow for easy and modular grid use. We need to be able to store green energies in a convenient fuel.

« It seems that perfection is attained, not when there is nothing more to add, but when there is nothing more to take away » wrote Antoine de Saint-Exupéry in “Terre des Hommes” in 1939. Why – that sounds great! Instead of those complicated to synthesize, long aliphatic chains that leave so much residue when incompletely burnt in a combustion engine, why not remove every single superfluous atom and go down to the simplest molecules? One could think that using the simplest molecules would mean doing the simplest chemistry. However, most small molecule activation reactions are often kinetically sluggish because of the high symmetry of such bonds, which are difficultly polarized. Small molecule activation is a multi-electron process which requires co-substrates. This could make them unattractive fuels as they require so much extra energy to be activated, however the energy stored in the very stable bonds of those simple molecules is tremendous and the controlled formation and breaking of such bonds presents the opportunity for very interesting research.

It would be pretty difficult to remove anything from dihydrogen, the simplest molecule made of the simplest element. The amount of energy (−286 kJ/mol) contained in the H-H bond makes it a very energy-dense compound. In fact, H_2 has the highest octane rating of all known compounds which would theoretically make it the ultimate fuel, be it for the fact that it is a gas at room pressure and temperature and is difficulty liquefiable. This makes it less attractive than slightly less simple molecules such as methane, methanol or ethanol, especially for transport applications. Nevertheless, the virtuous H_2/H_2O interconversion cycle is one of great interest and its mastering bring the promise of a brand new energy vector that renders a sustainable world more believable. How do we use H_2 as a fuel in a sustainable, renewable fashion? We hope that the following work can begin to answer this question, as well as several others that came up along the way.

Introduction

Small molecule activation remains one of the major challenges of catalytic chemistry. Reactions of interest in the fields of energy, health, commodity chemical synthesis and many others rely on the ability of chemists and materials scientists to find clever ways to activate, in a controlled fashion and if possible in mild conditions, stable bonds such as C-H, O_2, N_2 or H_2.[1] This is done with the help of appropriate catalysts which lower the activation barrier of these reactions of interest. The example of the Haber-Bosch process, which represents 1% of the worldwide energy consumption could be sufficient to convince one of the importance of finding new, more sustainable pathways for such reactions at the industrial scale.

The use of new energy vectors as alternatives to the fossil and nuclear fuels is of interest solely at the condition that said vectors be produced from renewable energy sources. Of all the possible fuels, hydrogen gas[2] stands out for several reasons: it is extremely energy-dense, lightweight, storable as a pressurized gas or as metal hydrides and participates in the virtuous water splitting cycle:

$$H_2O \rightleftharpoons H_2 + \frac{1}{2}O_2$$

During the endothermic water splitting, protons from water are reduced to form H_2 gas during the hydrogen evolution half-reaction (HER). The reverse exothermic reaction is the hydrogen oxidation half-reaction (HOR), which yields water.

The idea of using H_2 as an energy vector, albeit not a new one, has seen an impressive increase in interest over the past two decades.[3] One major problem of the use of H_2 gas is that nowadays, more than 90% of the worldwide production comes from oil cracking and natural gas reforming. However, alternatives exist and as you are reading these lines, researchers from all over the world including in the SolHyCat team are working on finding sustainable alternatives to split water in H_2 and O_2, be it in electrolysers with the help of platinum, novel materials or bio-inspired catalysts, or through photo-electrochemical cells (PEC) in an effort to develop artificial photosynthesis.[4] Once a renewable source of production of hydrogen has been found comes the need for controlled H_2 oxidation in order to retrieve, at the appropriate time and in the appropriate form, the energy that was invested in its making. Functional prototypes of heat engines which employ H_2 as a fuel have been made, albeit with very low efficiency.

Furthermore, poorly controlled oxidation reactions in a heat engine can lead to the formation of radicals and nitrogen oxide species. Ideally, this energy should be harnessed in the way of well-behaving electrons rather than loud explosions. This can be done in so-called fuel cells, which oxidize hydrogen at the anode and reduce oxygen at the cathode to form water and heat as the sole products of the reaction. Such technologies are mature and market-ready, notably the so-called proton-exchange membrane fuel cells (PEMFCs) which employ platinum group metals (PGMs) as catalysts at both the anode and cathode. However, as worldwide energy demands keep increasing, it has become obvious that the limited resources of PGMs will not be sufficient for a worldwide adoption of H_2 as an energy vector.[5-7]

In this introduction, we will try to take a global look at what mastering H_2 oxidation entails, from the kinetics of the reaction to the implementation of functional electrocatalytic materials in customer-ready systems, while describing some of the most relevant catalytic systems and their shaping into functional electrodes.

1. Hydrogen fuel cells

Since William Grove first proposed a fuel cell prototype in 1839 (Figure 1),[8] its shape and fuels have slightly varied. However, the concept has remained the same: two electrochemical reactions (oxidation of a fuel at the anode and reduction of an oxidizer at the cathode) happen on either side of an electrically-insulating, ion-permeating electrolyte.

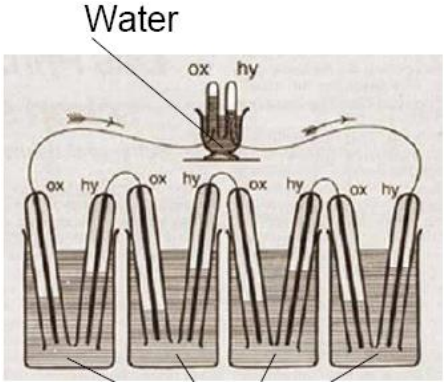

Figure 1. Early fuel cell prototype by William Grove. The fuel is H_2, the oxidizer is O_2 and the electrolyte is a sulphuric acid solution. It showcases the splitting of water in H_2 and O_2 and the reverse reaction.

This drives electrons from the anode to the cathode through a payload, such as an electrical engine or light bulb, where they expend their excess energy. The difference in potential between the two electrical reactions constitutes the electromotive force of the fuel cell and, along with the amount of reactions per unit or time, i.e. current density, determines its power output.

Nowadays, multiple fuels can be used and with them come multiple electrolytes and operating conditions,[9] but for the sake of clarity and brevity, our focus in this introduction shall remain on the use of H_2 gas as a fuel. Two main technologies coexist for H_2/O_2 or H_2/air fuel cells that differ in the operating pH and nature of the ions exchanged through the ionomer membrane.

a. Anion-exchange membrane fuel cells (AEMFCs)

In AEMFCs, O_2 is reduced at the cathode following the reaction:

$$O_2 + 2\,H_2O + 4\,e^- \rightarrow 4\,OH^-$$

Hydroxide ions migrate to the anode through a selective membrane to form water at the anode according to the following reaction:

$$H_2 + 2\,OH^- \rightarrow 2\,H_2O + 2\,e^-$$

AEMFCs offer the advantage that, as they operate at a very basic pH, the kinetics of the oxygen reduction reaction (ORR) are much less demanding than in acidic conditions,[10] allowing the use of alternatives to platinum as catalysts for the ORR. These include silver or some metal oxides,[10] or molecular catalysts such as iron or cobalt phtalocyanines and porphyrins,[11] and the basic pH allows the use of nickel-based alloy materials for HOR. However, they suffer one major drawback in the current lack of a technologically viable anion exchange membrane: OH^- diffusion is twice as sluggish (in water) than that of H^+ and increasing the amount of OH^- transporting, cationic functions in the membrane causes swelling issues which can in turn lead to mechanical failures. Additional problems include degradation of the membrane at high pH and temperature as well as difficult water management. Furthermore, AEMFCs suffer from long start-up times and are therefore more difficult to implement in applications where energetic demands can surge rapidly, such as electric vehicles.

b. Proton-exchange membrane fuel cells (PEMFCs)

On the other hand, PEMFCs rely on the transport of protons and not hydroxide ions through a selective membrane, from the anode to the cathode where they will participate in the ORR to form water (Figure 2). PEMFCs present many advantages: fast start-up (one to a few seconds), a somewhat wide operating temperature range (from RT to about 100 or 120°C depending on the nature of the exchange membrane), as well as a compact membrane-electrode assembly (assembly of an anode and a cathode separated by an electrolyte membrane, MEA) that enables efficient stacking of cells. This compactness is possible thanks to the discovery by DuPont in

the early 1960s of Nafion, a proton-specific ionomer that presents the particularity of being available in both film and solution forms, allowing its use within the electrode's thickness in addition to the electrolyte membrane, which enables good proton transport within the whole system. The composition, structure and functioning of Nafion are discussed in Chapter I.

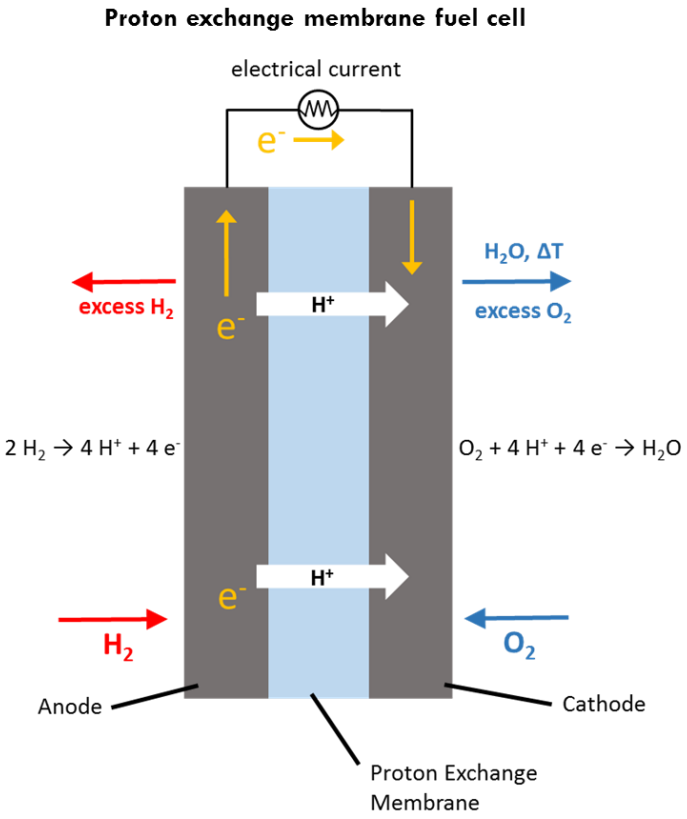

Figure 2. Schematic representation of a proton-exchange membrane fuel cell.

Current mature PEMFCs technologies employ Pt catalysts at both the anode and cathode, but commercial products with alternative catalysts are starting to appear. Ballard Power Systems released in late 2017 a compact, 30 W fuel cell stack that does not contain any PGM at the cathode, but still uses platinum at the anode. State of the art Pt fuel cells have an energetic efficiency of about 40 to 60 %, slightly higher than that of gas (25 to 50 %) or diesel engines (up to 45 %). However, with a proper heat cogeneration setup, efficiencies of up to 85% can be obtained.[12]

2. Activity markers of hydrogen interconversion catalysts

In this part, we briefly enumerate and define several important factors that will be used throughout this manuscript when describing catalysts for the hydrogen/proton interconversion reaction. It should be noted that, although they are here separated, some of them are inherently connected. It is therefore a global picture of all those figures of merit rather than each of them

individually that should be considered, while keeping in mind that each application has different specifications and that the nature of the most important activity marker is hence application-dependent.

a. Equilibrium potential and overpotential

The reversible potential of hydrogen interconversion in water is given by the equation below:

$$E_{H^+/H_2}^{0,app,H_2O} = -0.059\ pH\ (in\ V\ vs. SHE)$$

This arises from the simplification, with the Nernst equation, of the expression of a standard potential when $E_{H^+/H_2}^{0} = 0\ V\ vs. SHE$. In this work however, unless otherwise mentioned, the vast majority of the experiments being done in water at pH values very close to 0, we therefore approximate that:

$$E_{H^+/H_2}^{0,app,H_2O} \approx 0\ V\ vs. SHE$$

In the case of H_2/H^+ interconversion, overpotential, noted η, is the difference between $E_{H^+/H_2}^{0,app,H_2O}$ and E, the potential at which the reaction is studied:

$$\eta = \left| E_{H^+/H_2}^{0,app,H_2O} - E \right|$$

η is by convention a positive value and should be thought of as another scale for looking at the potential of observation of a reaction from the equilibrium potential of this reaction. As the equilibrium potential is in our conditions approximated at 0 vs. SHE, η is simply the absolute value of E and is quoted vs HER or HOR:

$$\eta = |E|$$

Better catalysts require low or even null overpotential. Of note, the electrochemical results in this work are formatted following the IUPAC convention, with the oxidation currents as positive values and positive values of E on the right hand side.

b. Turnover frequency

Turnover frequency (TOF) is the rate of reaction per unit of time happening at one catalytic site, expressed in s^{-1}, or Hz. Its value is only comparable for two catalysts if the environments in which it was measured are identical, as TOF depends tremendously on the conditions of

catalysis. Better catalysts display higher TOF and hence higher current densities. For an electrocatalytic reaction the TOF is related to the current density through the relation:

$$j = \frac{TOF \times SL}{n\mathcal{F}}$$

In which j is the current density in $A.cm^{-2}$, TOF is in h^{-1}, SL the site loading defined below in $mol.cm^{-2}$, n the number of electrons involved in the reaction and $\mathcal{F}$ the faraday constant in $A.h.mol^{-1}$. In the case of H_2/H^+ interconversion, n = 2. TOF over a certain time gives a turnover number (TON) in moles, which is to say the amount of converted substrate.

c. Site density and loading

In order to be able to estimate the TOF from current densities, the number of catalytic sites must be known. Two common metrics are site density (SD) and loading (SL). SD is the number of sites per unit volume that can be electrochemically addressed and SL the same value per unit of geometric area of the electrode. In this work we will mainly use SL values because the variation in thickness of the electrodes is yet not our main concern, as even our thickest electrodes remain within the 10-20 µm range which is not detrimental to MEA stacking. In future work we hope to show that much thicker electrodes, up to 100 µm thick, can be made with accessible sites throughout the electrode. SD and SL can be measured with the help of cyclic voltammetry (CV) under non-catalytic conditions. Of note, this method of SL determination yields an amount of sites connected electronically without regard to whether these sites are capable of catalysis. Indeed, a site might be connected electronically yet not reached by the gaseous substrate.

d. Catalytic bias

A catalyst is said reversible for hydrogen interconversion if it is able to catalyse both HOR and HER with no apparent overpotential, indicative of a fully reversible catalytic cycle. Not all catalysts are capable of perfectly reversible catalysis, and the reaction can be favoured one way or the other. This is the case for asymmetrical catalytic mechanisms such as those encountered in hydrogenases or bio-inspired catalysts.[13] This is termed "catalytic bias", which can be defined as the ratio of $\frac{TOF_{HOR}}{TOF_{HER}}$, originally used to describe hydrogenase enzymes.[14] When considering fuel cells, all other things equal, a catalyst with a bias towards hydrogen oxidation should be chosen, and this is part of our discussion in Chapter I. However, it could be interesting, in the case of unitized regenerative fuel cells (URFCs, which in regeneration mode

produce H_2 and O_2 and in fuel cell mode consume them) to consider pairing two catalysts with opposite catalytic biases. Of note, although catalytic bias is an intrinsic characteristic of one given catalyst, we show in this work that the ability of a given catalyst to perform a reaction one way or the other can be affected, to sometimes determining extents, by its environment. As a matter of fact, access to substrates, efficient removal of products and even the positioning of catalytic sites relative to one another within a catalytic layer are determining factors of efficacy.

e. Stability

Stability is often the most important factor for the industry. Discussions with engineers from the industrial private sector during the time of this thesis have revolved around the fact that even with low efficiency or selectivity, a catalyst could be of interest if it was simple to implement for a long term and did not need frequent replacing.

Stabilities issues can arise from either poisoning, degradation of the catalyst, mechanical failure of the electrode support or leaching of the catalyst. In the case of platinum for instance, slow dissolution of nanoparticles in acidic conditions and subsequent recrystallization in the membrane as well as poisoning from contaminants found in commercial H_2 gas are foremost. Stability can be assessed in different ways, with some of the most important considerations for fuel cell anodes being: number of hours of functioning at the rated power output of the stack, number of cold air/air start-ups, resilience to fuel starvation and presence of O_2 at the anode. One method of choice to assess degradation of a platinum catalyst is the so-called CO-stripping method in which a monolayer of CO is adsorbed onto the Pt catalyst and subsequently electrochemically removed, allowing quantification of the active Pt surface, and monitoring of the evolution of SL or SD with aging.[15]

f. Tafel plots

As mentioned above, some of those parameters are connected. Away from equilibrium, current densities may follow the Tafel law:

$$\eta = b \times \ln(\frac{j}{j_0})$$

In which j in mA/cm² is the current density at an overpotential η in mV, j_0 in mA/cm² is the exchange current density and b is the Tafel slope, in mV/decade.

A good way of comparing the overall electrocatalytic ability of a catalysts for a specific reaction and in a specific environment is Tafel plots, which relates in a linear way the current densities, and therefore TOF, to the overpotential by plotting ln (j) = f (η). Tafel plots were originally developed to describe electrocatalysis at catalytic surfaces. They then have been applied to the benchmarking of homogeneous hydrogen-evolving catalysts by Savéant and co-workers, with modifications to address homogeneous catalysis,[16] and can yield information on the catalytic mechanisms at play. The linearization of a Tafel equation yields direct access to both j_0, which represents the ability of a catalyst to do H^+/H_2 interconversion at the equilibrium and can be thought of as the "idle catalytic speed" of a system, a representation of its unhindered catalytic ability and can be helpful to understand the influence of environment on catalysis; and b, the Tafel slope which represents the linear response of the system to overpotential in ideal catalytic conditions.[17,18]

3. Pt catalysts

Accounts of platinum or PGMs as catalysts for hydrogen oxidation (and other reactions) date back to the middle of the 20th century, and much research has been and still is being done to optimize these systems.[19] Platinum presents the advantage of being able to perform both oxidation and reduction reactions without losing it metallic character, making it a catalyst of choice for many industrial applications. HOR on nanoparticular Pt electrodes usually follows the Tafel-Volmer mechanism, which begins with the adsorption of a hydrogen molecule on the surface of the nanoparticle, followed by its almost barrier-free dissociation into two H atoms before electron transfers.[20] Nowadays, mature electrolyser and fuel cell technologies employ platinum catalysts and show great power outputs with very little overpotential requirements as platinum catalyses hydrogen interconversion fully reversibly at the thermodynamic potential.

With the very high affinity of platinum for H_2 comes an affinity for molecules with similar properties such as CO and H_2S, which are unfortunate by-product contaminants of commercial H_2 from fossil sources. However, the conversion of such substrates is only partial and residual species can remain on the surface of platinum particles, causing a poisoning of the surface that strongly hinders catalysis. CO-resistant catalysts in particular are very sought after, although it should be noted that those contaminants are present in H_2 obtained from oil reforming and not from electrolysis, which means that if H_2 could be obtained in large amounts by water splitting, for instance through artificial photosynthesis or photovoltaic panels coupled to electrolysers, this problem could be resolved.

	Catalyst amount (mg/cm²)		*Normalized catalyst amount (g/kW)*
	Anode	Cathode	Whole PEMFC
Status	0.05	0.2	0.25
2020 target	0.025	0.1	0.125
Optimal	0.0125	0.05	0.0625

Table 1. State of the art and DoE 2020 targets for the Pt loadings of a PEMFC.

Table 1 presents the targets of the US Department of Energy regarding the amounts of Pt in PEMFCs. Even if the optimal targets were reached, it is estimated that a worldwide adoption of fuel cell vehicles is not a viable option given the current knowledge on worldwide stocks of Pt (estimated at 40 000 tons). It should be noted that Pt mining in itself is not economically viable: it is a by-product of Ni and Co mining, with cobalt representing the vast majority of the financial benefits of such mining operations. The yearly production of Pt is currently in the neighbourhood of 200 tons/year, and would need to be quintupled to be able to launch and maintain a fleet of a 100 million of electric vehicles.[21] This is not even taking in consideration the possible use of fuel cells as an alternative energy vector in other domains than transportation, such as a grid alternative in the eventuality of a massive decentralization of electricity production. In addition to purely quantitative considerations, several geopolitical and economic factors weigh in heavily on the consideration of wide-scale adoption of platinum fuel cells. About 70 % of platinum is mined in South Africa. It is a risk for manufacturers to rely on a material that is at the hands of a single entity, for its price is subject to strong, arbitrary variations. This can represent a non-negligible economic variable, as the cost contribution of platinum catalysts was estimated in 2013 at about 17% of the price of a 80kW fuel cell stack.[22]

4. Alternative catalysts

The bulk of research aimed at replacing platinum has been done on materials for the oxygen reduction reaction (ORR), as the cathode of a fuel cell represents nowadays 75% of the overall platinum loading (Table 1). Hence, few alternatives to platinum exist for H_2 oxidation materials. Among the most notable are nickel and CoNiMo alloys,[15,23,24] as well as some tungsten and molybdenum carbides.[25] The perks and drawbacks of such alternatives are briefly discussed here but their benchmarking results are listed further down in this introduction, under part 7. Ni (and CoNiMo) alloys present activity comparable to that of platinum in basic media as HOR on Pt is slower by about two orders of magnitude in basic media compared to acidic media.[26] However, due to dissolution issues, these materials cannot be implemented in the acidic

conditions required by a PEMFC. On the other hand, tungsten (WC) and molybdenum carbides (MoC) and others, such as CoWC and MoWC, are stable in acidic conditions as they were first implemented in fuel cells as a support material for platinum catalysts and are now studied as catalysts.[25,27] In addition to being made from abundant resources, they show good tolerance to CO and H_2S, thermal and mechanical stability and resistant to corrosion.

5. Inspiration from nature

a. Hydrogenase enzymes

Although hydrogen is rarely found in its gaseous form on Earth, it is a critical energy vector for some forms of life. Many micro-organisms rely, in part or solely, on the hydrogen present in their environment as a source of energy, a process made possible by the production of extremely efficient enzymes, hydrogenases, which facilitate hydrogen/proton interconversion close to the thermodynamic equilibrium potential.[28-30] Hydrogenases, the first structures of which have been reported in the late 90's,[28,31] display finely tuned active sites. Two main classes of hydrogenases exist ([NiFe] and [FeFe]-hydrogenases), defined by the metal cluster present at their active site. The active site of [FeFe]-hydrogenases (Figure 3, left) is made of 2 iron atoms, bearing CN^- and CO ligands, quite unusual as constitutive components of enzymatic active sites. An azadithiolate (adt^{2-}) ligand bridges both iron atoms in a bidentate manner.[32] This binuclear subsite is connected to a [4Fe-4S] cluster through a cysteinate ligand, forming the hexanuclear H-cluster. The active site of [NiFe]-hydrogenases (Figure 3, right) is an asymmetric heterodinuclear Ni-Fe cluster. The nickel atom is in a highly distorted environment formed by four cysteinate ligands, two of them bridging with an organometallic dicyanocarbonyl iron centre. Those unusual CO and CN ligands have provided very useful spectroscopic handles to elucidate the redox and geometric features of the active sites at different stages of catalysis, termed enzymatic states, allowing for a thorough understanding of the catalytic cycles followed by those natural catalysts.

Figure 3. Active sites of [FeFe]- (left) and [NiFe]- (right) hydrogenases. Blue: metal atoms that participate in metal-hydride bond formation; green: pendent bases; red: open coordination sites.

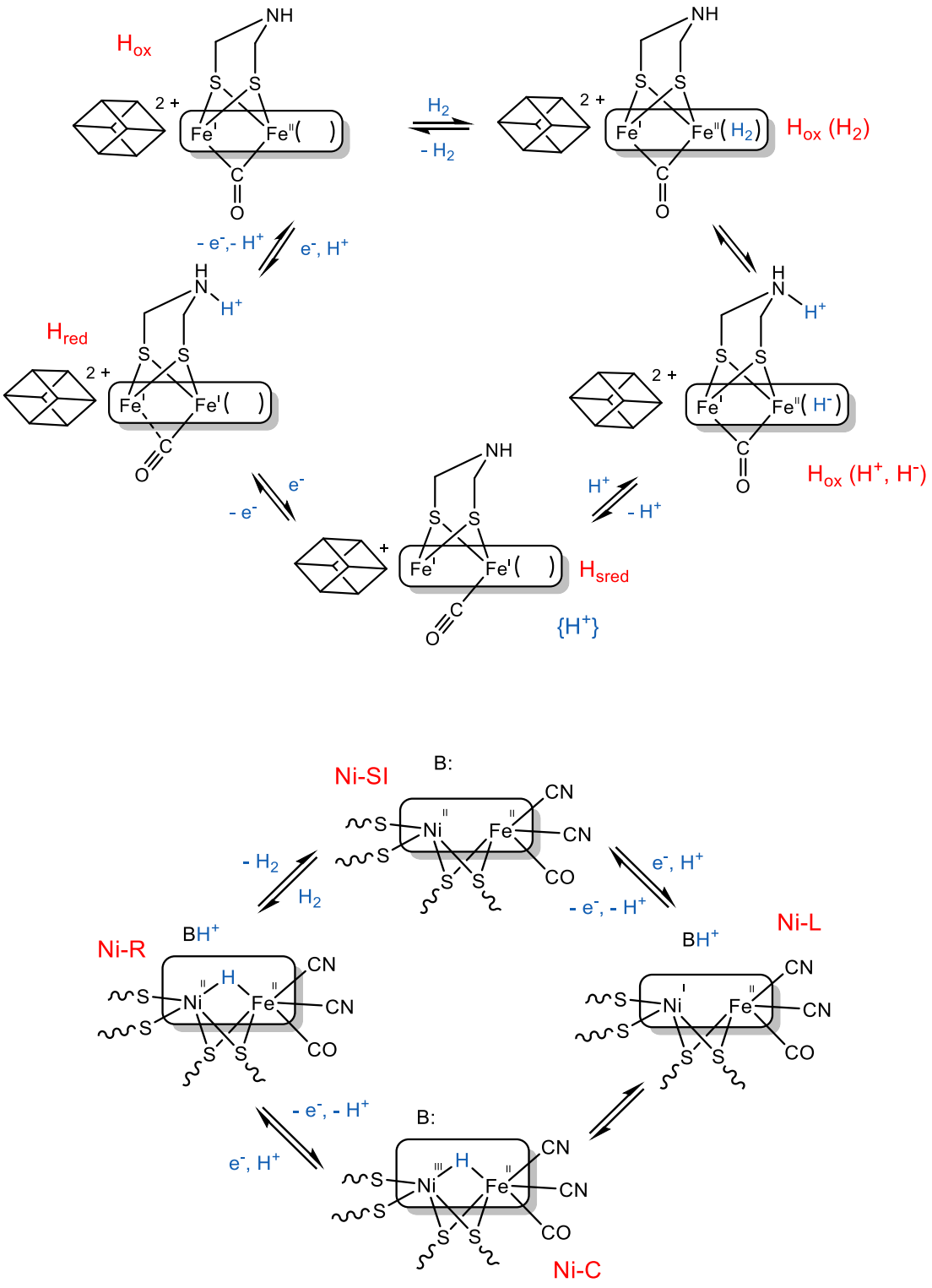

Figure 4. Proposed catalytic mechanism for H_2 evolution and uptake at [FeFe]-hydrogenase active site[28] (top) and [NiFe]-hydrogenase active site (bottom);[33] the cube in the top panel represents the proximal [4Fe-4S] centre with one or two positive charges; B represents a basic site in the vicinity of the active site of [NiFe] hydrogenase, which can be either a terminal thiolate ligand[28] of Ni or an arginine residue.[34]

The HOR, a 2-electron, 2-proton process, occurs at the hydrogenase active site through the heterolytic splitting of an H_2 molecule into a metal-bound hydride and a proton.[35] This process is permitted thanks to, at least, three important features of the active site that we will first exemplify for [FeFe]-hydrogenases (Figure 4, top). The redox cycling necessary for HOR catalysis occurs at the furthest Fe atom with regard to the [4Fe-4S] cluster, termed distal or Fe_d. This iron atom displays redox properties appropriately tuned by the nearby metal atom and the ligands. An open coordination site is also available on Fe_d thanks to a specific conformation of the cluster, favoured by the protein scaffold. A H_2 molecule can coordinate and is polarized by the presence of a nearby pendent base which will be protonated, yielding a hydride ligand onto Fe_d. This first proton is brought to the surface of the protein from the pendent base through a subsequent network of H-bonds.[28,36,37] The hydride is then oxidized using one electron from the iron atom and one from the [4Fe-4S] cluster to form a proton. A single electron transfer followed by a proton-coupled electron transfer completes proton elimination and restores the active site to its resting state. Similar features are also found in [NiFe]-hydrogenases with redox cycling taking place at the nickel atom in this case. The sulphur atoms of terminal thiolate ligands have been considered for long to act as basic sites,[28] however a recent study by the Armstrong group has demonstrated through site-targeted mutagenesis the important role played by the guanidine head group of an arginine residue suspended above the nickel and iron atoms for H_2 interconversion in *E. coli* Hyd-1 (Figure 3, right).[34] Work in the Vincent group has given further insight about the electron and proton transfer processes in the same enzyme, highlighting the relevance of the Ni-L state with a $Ni^{I}Fe^{II}$ electronic structure during hydrogen uptake catalysis.[33] Dissymmetrical bridging coordination of a hydride ligand between the two metals occurs in two other intermediate states, Ni-C[38,39] and Ni-R.[40] Such fundamental understanding of mechanisms has proven critical to enable synthesis of bio-inspired catalysts.

b. Bio-mimicry and bio-inspiration

This growing insight into the finesse of the catalytic mechanisms at play in natural systems as well as their further structural characterization has paved the way of two synthetic roads, bio-mimicry and bio-inspiration, which, although they have been at the core or mankind's technological progress for ages, have only relatively recently been coined as terms that apply to design of molecules.[41]

Bio-mimicry is trying to replicate the structure of the whole or part of a biological system. In the case of hydrogenase enzymes, chemical bio-mimicry of the active site has yielded several notable dinuclear complexes, some of which are depicted hereafter.

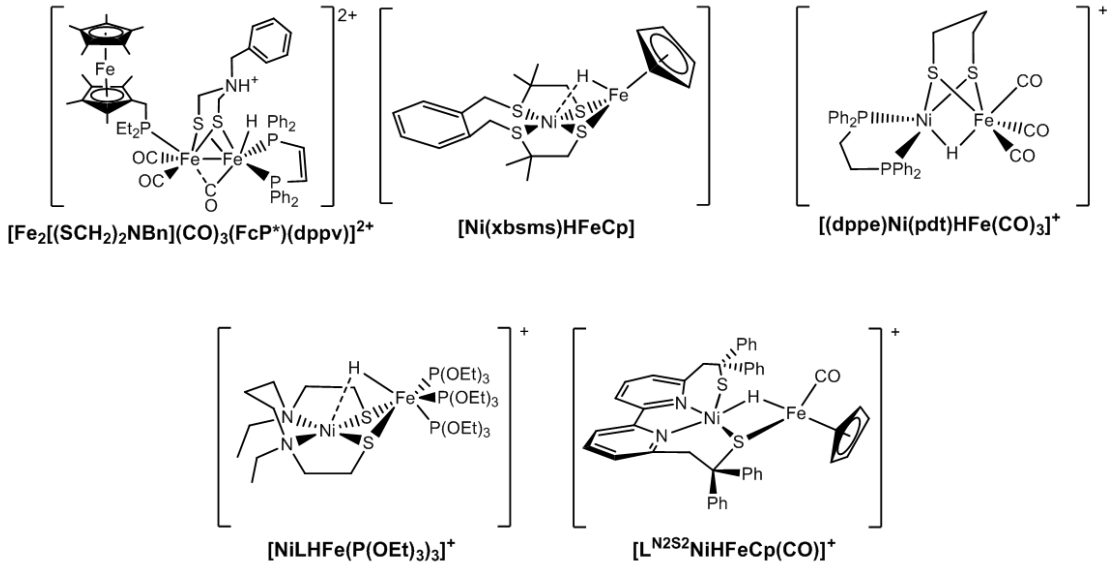

Figure 5. Selected biomimetic complexes of the active sites of [FeFe]- and [NiFe]-hydrogenases.[42,43]

The complexes presented in Figure 5 display some capability for hydrogen evolution, although they are not among the best performing catalysts: they often suffer from poor stability and high overpotential requirements. Furthermore, few are capable of hydrogen oxidation catalysis which is done by most hydrogenases. Indeed, structure is but one of the multiple facets of the evolutionary optimization of biological systems and by tending towards structural precision only, one may miss out on other aspects crucial to catalysis. However, should a biomimetic complex display binding affinity for a substrate or, *a fortiori*, stoichiometric or catalytic activity for the conversion of this substrate, it then provides a tremendous tool to further investigate reactivity as it can be equipped with practical spectroscopic handles such as CO ligands.

Bio-inspiration, on the other hand, is to try and replicate function before shape and composition. By identifying key features involved in catalysis, that is what needs to be preserved and what are mere useless motifs, molecular chemists can design a range of potential catalysts, synthetically accessible and which should behave somehow like the original biological system. The features that have been widely recognized as keys to design molecular bio-inspired hydrogen oxidation catalysts (HOCs) are: (1) a coordination site for a H_2 molecule located onto (2) a metal centre, with moderate redox potentials and (3) a pendent base on a somewhat flexible arm in the vicinity of the coordination site, capable to polarize the H-H bond and then protonate, leaving a hydride ligand bound to the metal site.

c. Bio-inspired molecular catalysts

Implementation of such functions in HOCs has been done over the past fifteen years or so in a very thorough work by Daniel DuBois and co-workers first at the National Renewable Energy Laboratory, then at the Pacific Northwest National Laboratory.[44-51] While writing an exhaustive literature review and detailed accounts of all compounds prepared over this period would be an unnecessary and daunting task, some of them are presented in Figure 6 below.

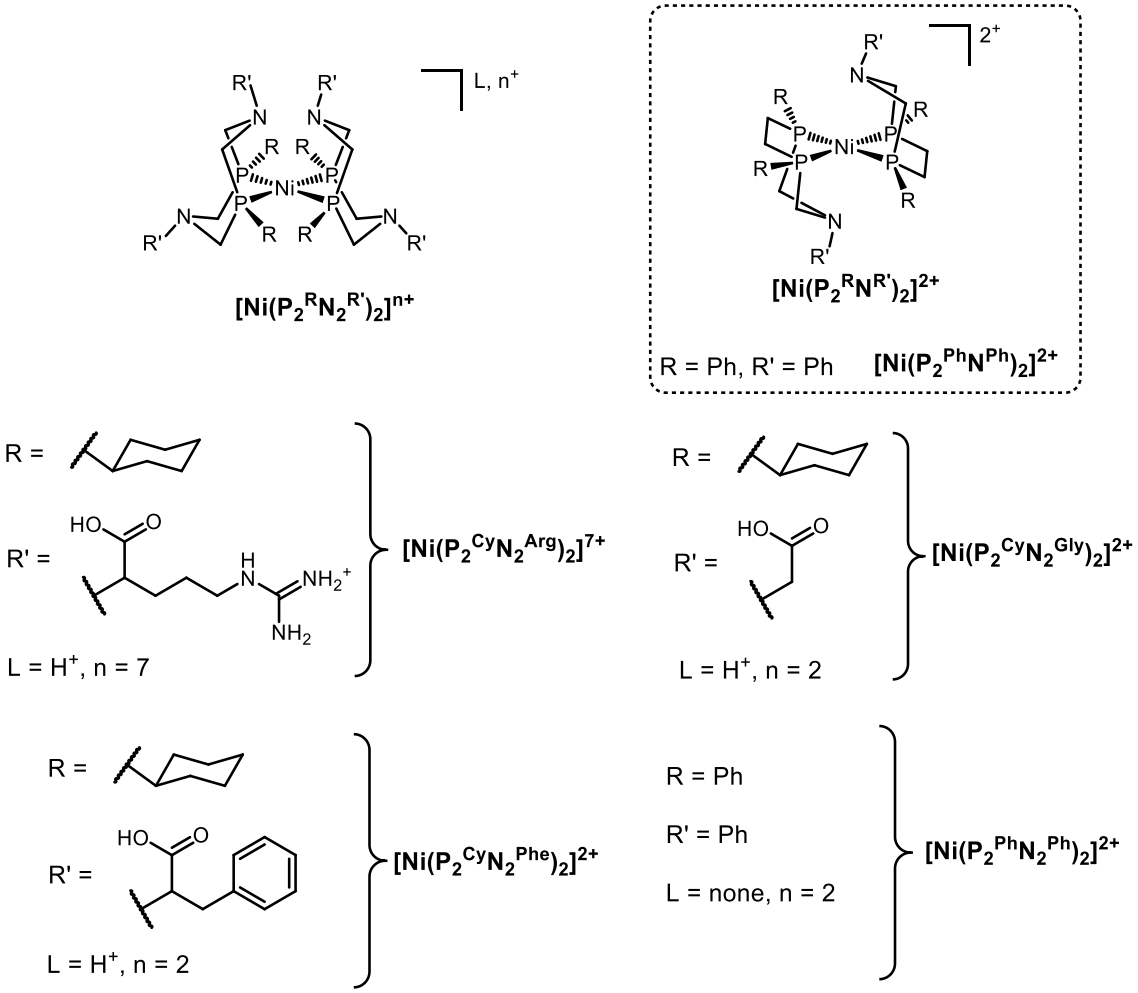

Figure 6. Selected examples of nickel-based DuBois catalysts.

These catalysts are based on a nickel(II) centre coordinated to two diphosphine ligands in a distorted square planar geometry. Ligands bear one or two pendent amine groups, referring to the $[Ni(P_2^RN_2^{R'})_2]^{n+}$ or to the $[Ni(P_2^RN^{R'})_2]^{n+}$ type, respectively. One of the many advantages of the so-called DuBois catalysts is the versatility of functionalization brought by their elegant and quite facile synthetic process: a primary phosphine bearing a chosen function is

bishydroxymethylated and easily bound to a primary amine thanks to Schiff-base chemistry to form a seven- or eight-member ring with remarkable chelating properties.[45,51,52]

Different functionalization on the P and N atoms has enabled a systematic study of the catalytic contributions of three well-defined coordination spheres (termed inner, second and outer spheres),[46,51] which all play crucial yet different roles. In brief and surely oversimplified terms, the inner sphere, which contains the P atoms, tunes the redox potential of the metal and hence its ability to form a hydride when reached by H_2, as well as the potential of catalysis; the second sphere, which contains the pendent amine groups, enables polarization of the H_2 molecule, tunes substrate-specificity and reaction rate; and the outer sphere, which holds the amine substituents, matters for bulk diffusion of substrates and this is where functions can be added to a catalyst for grafting onto electrodes.[53] In this work, we first focus on three DuBois catalysts with three anchoring strategies, described a bit further below.

6. Grafting of molecular catalysts onto electrode materials

The grafting of catalysts onto a conductive surface is the next natural step towards integration. It hopefully enables fast and quantitative electron transfer between the catalyst and the electrode material and allows for stabilization of catalytic sites. Ideally, all the grafted catalysts will take part in catalysis and therefore optimal use of the metal content of the electrode can be attained. Going from a catalyst in solution to its grafted equivalent is however often not a straightforward process. Depending on the grafting strategy, many of its characteristic features can be modified and the catalyst's intrinsic properties can change: catalytic sites coerced in close vicinity can aggregate and/or deactivate, geometric restrictions can induce a change in TOF, specificity for a substrate or even overall catalytic ability. Parasitic phenomena such as substrate/product diffusion or sluggish electron transfer can appear, hindering catalytic efficiency. In this part, some common strategies to attach molecular catalysts to a conductive surfaces are described, along with their most important perks and drawbacks. The synthetic versatility of DuBois complexes indeed allows for their functionalization towards grafting, as demonstrated by work in our lab and others[48,54,55] which employ various grafting handles on the nitrogen atoms to load conductive surfaces with catalyst. Such graftable complexes along with the grafting strategy are further detailed in the next paragraph. Here, we do not limit our scope to bio-inspired catalysts for hydrogen oxidation but also give an example of the attachment of a hydrogenase enzyme or HER catalysts onto electrodes.

a. Physical adsorption: entrapment in a polymeric layer

In this approach, the catalyst is merely physically adsorbed onto the surface, stabilized within a polymeric matrix. These matrixes are usually Nafion™ (which structure will be more thoroughly discussed in Chapter I) or polyvinyl and/or hydrophilic polystyrene derivatives. The catalyst can either be drop-casted onto the carbon electrode, then covered in the matrix or mixed to the matrix prior to deposition, which can lead to differences in film stability and catalyst access to substrates.

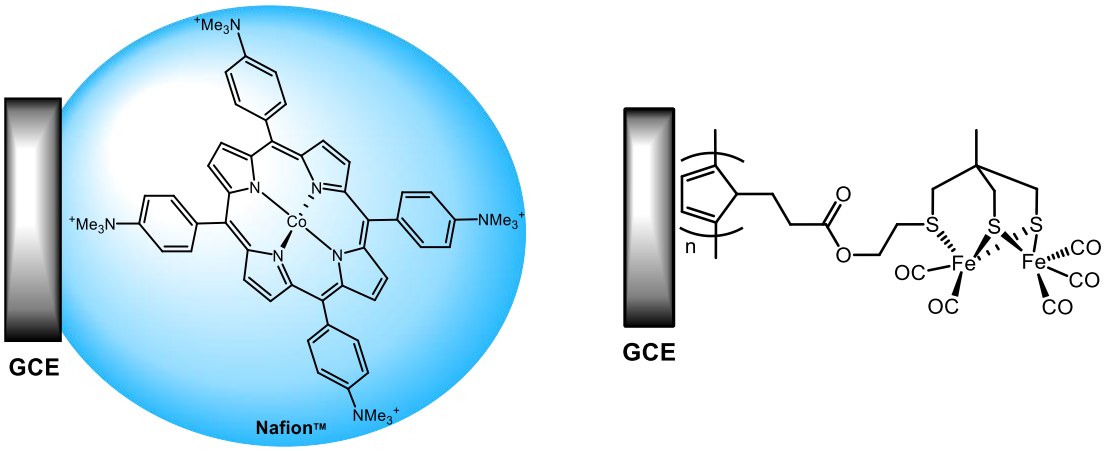

Figure 7. Example of a charged Cobalt porphyrin entrapped into Nafion™ deposited onto GCE (left) and biomimetic diiron catalyst immobilized onto a glassy carbon electrode (GCE) through attachment to a polypyrrole film (right).

This strategy was already implemented in 1985 by Spiro and co-workers to introduce charged Co porphyrin derivatives into Nafion™ films (Figure 7 left) to catalyse the hydrogen evolution reaction (HER).[56] Electrodes can also be coated with conducting polymers obtained via an electropolymerization process. Films are obtained that expose pendent reactive moieties designed to achieve covalent coupling with the molecular backbones of hydrogen evolving catalysts. This methodology was initially used to immobilize a rhodium complex.[57] More recently Pickett and co-workers synthesized a bisthiolate-bridged hexacarbonyl diiron complex using a dithiolate bridging ligand carrying a hydroxyl moiety.[58] This hydrogenase mimic was reacted with a glassy carbon electrode coated with a functionalized polypyrrole film, containing electrophilic groups and covalently attached through transesterification (Figure 7, right). The supported complex shows an electrochemical behaviour similar to that of its homogeneous equivalent. A catalytic peak assigned to proton reduction is observed at 120 mV more positive than the unmodified electrode. In such approaches, the moderate activity is believed to result from a slow electron transfer within the matrix. These studies show that although a major perk

of matrix entrapment is its facile implementation, it comes with a number of drawbacks that can severely impede catalysis. It is a great tool to perform the initial assessment of "graftability" and electrocatalytic behaviour of catalysts but should be replaced with a dedicated grafting strategy if satisfying efficiency and stability are to be reached. Of note, Plumeré and co-workers have used redox-active polymeric matrixes to anchor hydrogenase enzymes onto electrodes while protecting them from oxidative stress,[59] showcasing the versatility of functionalization of polymers in order to bring new properties to electrode materials.

b. Diazonium reduction of anchoring moieties

i. Covalent grafting

Among other methodologies,[55,60] the electroreduction of diazonium salts[61] has proven a popular and efficient way to anchor diverse hydrogen oxidation catalysts onto electrodes.[54,62-66] For instance, an amino-decorated aryldiazonium salt generates upon reduction an oligomeric layer covalently bound to an electrode surface and exposing amino functions towards the electrolyte (Figure 8).

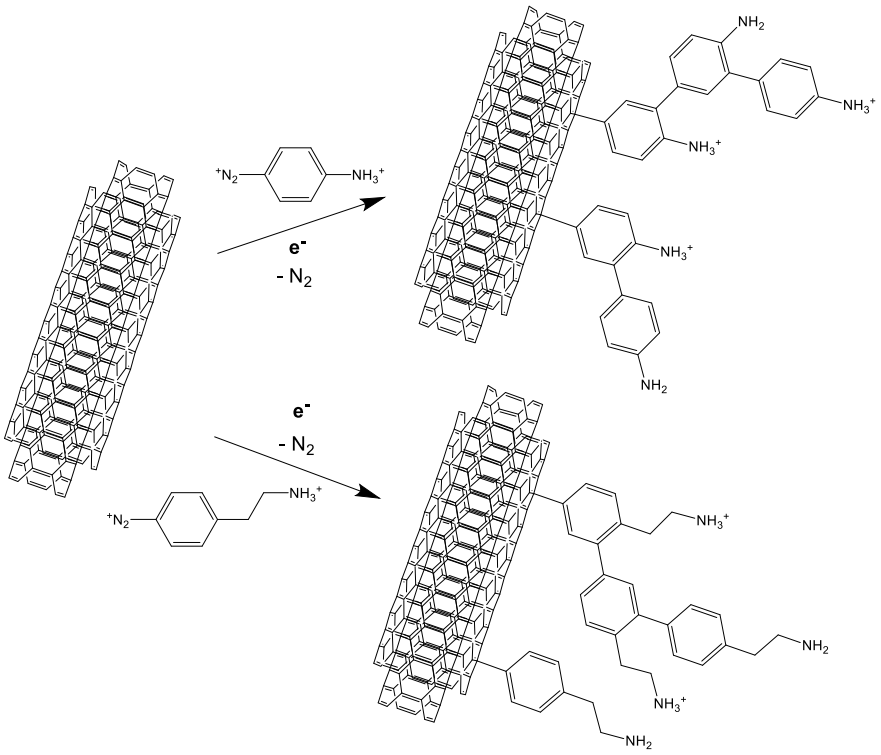

Figure 8. Functionalization of conductive surfaces by an amino-polyphenylene layer via diazonium salt reduction.[61]

Work in our group in collaboration with B. Jousselme and S. Palacin,[54,65,67-69] showed that, when performed onto multi-wall carbon nanotubes (MWNTs), the electroreduction of

diazonium salts provides a quite unique way of grafting a significant amount of redox probes on the electrode surface. This finding was further exploited to attach nickel bis-diphosphine complexes, resulting in efficient and stable cathode materials for H_2 oxidation operating in aqueous electrolytes. In both cases, the supporting material is first elaborated by filtering a suspension containing MWNTs onto a gas diffusion layer (GDL). GDLs have been specifically developed PEM-based technologies and are made of carbon cloth coated in a gas-permeable yet watertight carbon conductive membrane. The electroreduction of 4-(2-aminoethyl)-benzene diazonium on the mesoporous GDL/MWNTs substrate creates an oligomeric film with pendent amino groups, yielding the GDL/MWNT-amino electrode (Figure 8). These modified electrodes were then reacted with a DuBois catalyst decorated by phthalimide ester moieties, $[Ni(P_2^{Cy}N_2^{Ester})_2]^{2+}$, termed **CyEster**, in the presence of an a weak base (2,6-lutidine) in DMF. This procedure yields a GDL/MWNT electrode with the catalyst covalently linked to the surface of the substrate through amide linkages (Figure 9).[54,65]

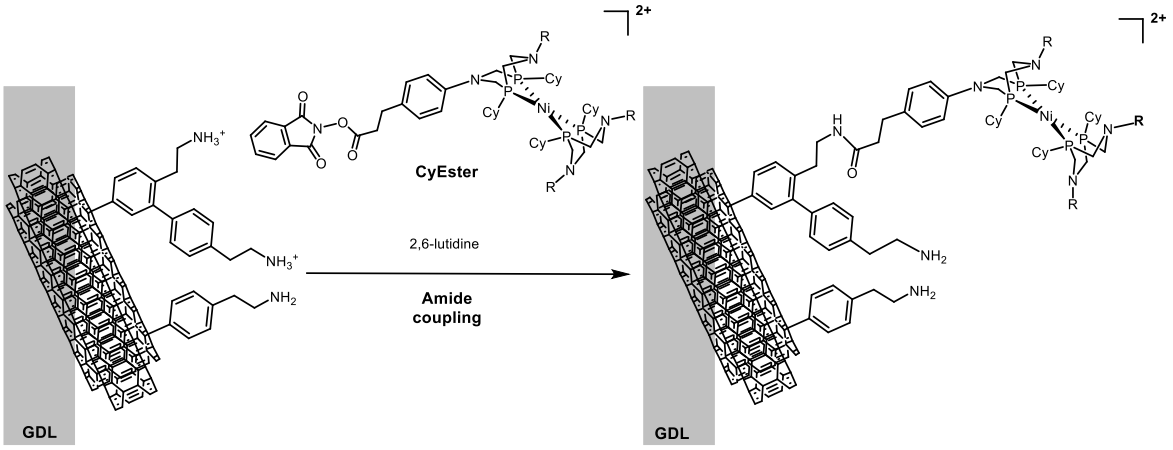

Figure 9. Reaction of the GDL/MWNT-amino electrode with a DuBois complex bearing an activated ester function, ***CyEster****.*

An alternative procedure can be used to construct the molecular catalytic sites in a stepwise manner, in which the diphosphine ligand was firstly immobilized *via* amide coupling, then the nickel centre was introduced in a second step with either the $[Ni(CH_3CN)_6](BF_4)_2$ complex or $[Ni(H_2O)_6](BF_4)_2$, which work in our laboratory has shown to be equally good for formation of $[Ni(P^R{}_2N^{R'}{}_2)_2]^{n+}$ type complexes. The latter option has the advantage of commercial availability, further simplifying the synthetic process.[70] It also notably increased the amount of grafted catalytic sites (SL), benefiting the catalytic activity per surface area of the electrode.

ii. Polycationic/polyanionic grafting

Similarly, in collaboration with Alan Le Goff at Univ. Grenoble Alpes, MWNTs were modified, following published procedures,[71] to bear naphthoic acid functions in order to accommodate a

DuBois complex bearing multiple positive charges, $[Ni(P_2^{Cy}N_2^{Arg})_2]^{7+}$, abbreviated **CyArg** through a polyanionic/polycationic interaction (Figure 10). In contrast with the previous diazonium functionalization, this one is done in solution, chemically rather than electrochemically, following work by Tour *et al*. This presents obvious perks for industrial applications as convenient batch chemical reactions can be employed to prepare large amounts of modified MWNTS.

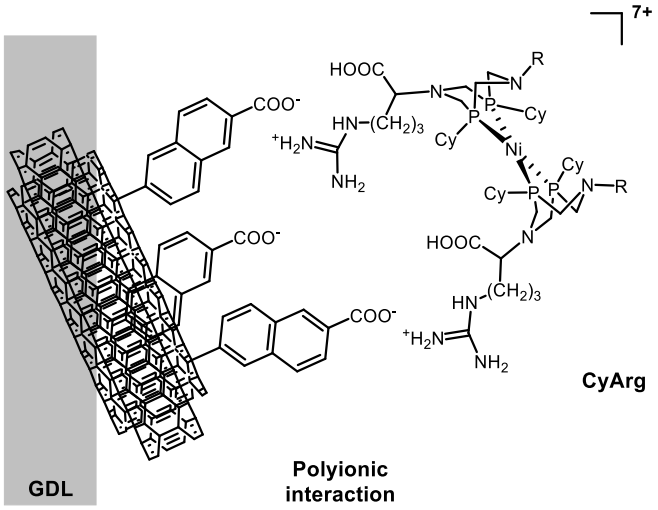

Figure 10. $[Ni(P_2^{Cy}N_2^{Arg})_2]^{7+}$ grafted onto a GDL/MWNT-COOH electrode.

It should be noted that in the operating conditions of a PEMFC, which require acidic pH, the carboxylic groups are expected to be protonated and therefore unable to serve as anionic anchors. However, stable catalyst grafting is observed even in pH 0 electrolyte, which we attribute to two things. First, the highly cationic catalyst could display strong affinity for the graphitic regions of the MWNT through π-cation interactions. Second, both the catalyst and the MWNT-COOH are very hydrophilic, so that hydrogen bonds could be formed between the amine and carboxylic acid functions.

c. π-stacking interaction

Lastly, catalysts can be grafted onto pristine nanotubes by incorporating pyrene moieties in their outer coordination sphere that create some reasonably strong π-π interactions with the graphitic regions of carbon nanotubes. This was done in 2011 in our team for a DuBois catalyst capable of H_2/H^+ interconversion, $[Ni(P_2^{Cy}N_2^{CH_2Pyrene})_2]^{2+}$, termed **CyPy** (Figure 11).[68] Such an electrode was implemented in 2015 in the proof of concept of a functional noble metal-free compact fuel cell.[72]

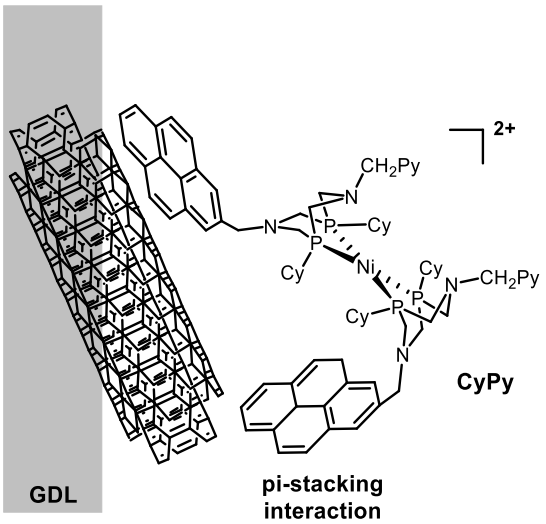

Figure 11. $[Ni(P_2^{Cy}N_2^{CH2Pyrene})_2]^{2+}$ grafted onto a GDL/MWNT electrode.

The above grafting strategies have proven effective at placing catalytic sites at a so called triple point (illustrated in Figure 12), where the three networks for gas, proton and electron transport are interconnected. In this way, the catalyst is electronically connected, can be reached by the gas substrate and efficiently gets rid of protons via the electrolyte, all of which are necessary for good catalytic performance. Chapter II is in part focused on optimizing the amount of catalytic sites placed at this triple point.

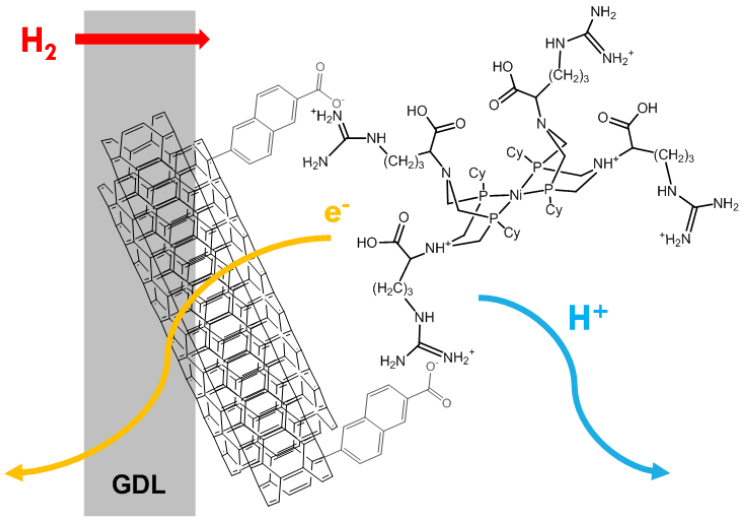

*Figure 12. Schematic representation of a **CyArg** catalyst placed at the triple point in a catalytic layer.*

The three catalysts, **CyEster**, **CyArg** and **CyPy**, were our main candidates throughout this work because of the afore-mentioned qualities. Chapter I compares their perks and drawbacks in more detail, and leads to the contextualized choice of the best one, **CyArg**, for optimization and integration. The catalytic cycle for HOR interconversion by **CyArg**, as proposed by the group of Wendy Shaw, is discussed in Chapter III.

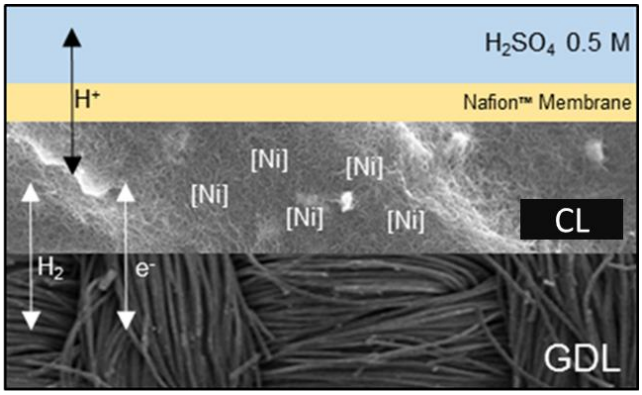

Figure 13. Schematic representation of a fuel cell anode. GDL is a gas diffusion layer and CL the catalytic layer.

Figure 13 present a schematic representation of a finished electrode, composed of a porous, conductive backing material, the GDL, onto which the catalytic layer (CL) containing the catalyst and carbon nanotubes is deposited. In some cases, a proton exchange Nafion membrane (yellow) is added between the CL and the electrolyte (blue). In order to enable integration in fuel cells, Nafion is added as an ionomer throughout the thickness of the CL in order to ensure a thorough proton relay in the entire thickness of the electrode in the absence of electrolyte.

7. State of the art of anodes for HOR

We here give the current densities of several anodes in context (experimental conditions and electrolyte), in so-called liquid electrolyte half-cell experiments. In this setup, the anode catalyst is deposited onto a GDL, secured within a sample holder that enables gas diffusion from the back as well as electrical conductivity and a known surface of the electrode is exposed to a liquid electrolyte such as an acid in water (See Figure 14). Current densities are then assessed in a classical three-electrode electrochemical setup. This allows comparison of the capacities of standalone anodes for HOR. One way of giving the benchmarking values for a supported HOR catalyst is either current density at a given overpotential, or overpotential required to reach a given current density.[73] In our case, we note j_{ox} the current density for HOR at a given potential. This is the common benchmarking metric used in our lab for bio-inspired catalytic materials. However, for Pt-based catalysts which display a fully micro-reversible mechanism for HOR and HER, the benchmarking value is the so-called exchange current density (either j_0 in A/cm^2_{geo} in which the surface in the geometric surface of the electrode, or $i_{0,s}$ in A/cm^2_{Pt} in which the surface is the specific surface of Pt in the electrode). It represents a sort of "idle speed" of the catalyst, and describes its full catalytic capacity independently of environmental factors. We determine j_0 values for our best electrodes in Chapter III.

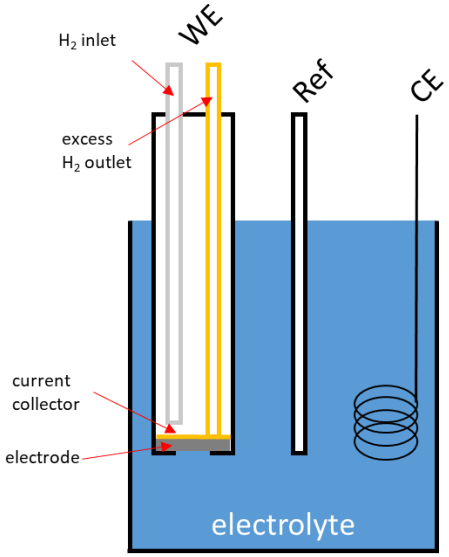

Figure 14. Schematic representation of a half-cell setup. WE = Working Electrode, Ref = reference electrode, CE = Counter Electrode.

Table 2 hereafter gathers the j_{ox} values for several catalysts and j_0 values for state of the art, ultra-low loading platinum catalysts (ULL-Pt). It appears from this table that the best current densities of **CyEster** bio-inspired anode which sit at 10 % of the best performances of an ULL-Pt electrode. Literature on Pt-based anode catalysts in half-cell setup is quite rare, due to the fact that most of the research effort is focused on the ORR along with the very high exchange current densities of HOR on Pt, which are very difficult to measure accurately. The first two entries in this table showcase the improvement over seven years in design and benchmarking of Pt/C catalysts for HOR: with a six-fold decrease in Pt loading, similar j_{ox} are observed with a threefold increase in j_0. According to the authors, this increase in j_0 is rather due to better measurement conditions and fitting of the data than to an intrinsic difference between catalysts. The other non-noble metal-based catalyst for HOR presented here, a tungsten carbide, shows an activity about 20 % as good as that of the ULL-Pt electrode at 150 mV of overpotential.

Catalyst	***j_0 (mA/cm²)***	***j_{ox} (mA/cm²)***	***η_{jox} (mV)***	***T (°C)***	***Electrolyte***	***Year^{ref}***
Pt/C 10 µg/cm²	26	210 400	150 350	50	H_2SO_4 1 M	2008[74]
Pt/C 1.7 µg/cm²	70	250	200	25	H_2SO_4 0.5 M	2015[75]
CyEster	-	13 40	350	25 85	H_2SO_4 0.5 M	2016[76]
WC	-	40	150	65	Nafion 212	2009[24,25]

Table 2. Values of j_0 and j_{ox} for different catalytic systems for the HOR. For jox, the overpotential (η_{jox}) is given. The temperature and electrolyte columns are for both the j_0 and j_{ox} values.

The state of the art of $i_{0,s}$ values for Pt/C catalysts is very well reported in two papers by the group of Gasteiger,[77,78] however they are of little use for comparison with our systems. Indeed the value of $i_{0,s}$ relies on the specific surface area of the catalytic nanoparticles and is quite meaningless when describing molecular catalysts. Instead, we compare in Chapter II our best performing catalysts to Pt/C as shown in Table 2 using j_{ox} and j_0 as benchmarking metrics.

8. Ambitions of this work

In this work, we focus on bioinspired DuBois-type HOR catalysts, but rather than try and design further, more efficient catalysts, we aim instead to investigate the optimization of some of the most promising bio-inspired electrocatalytic materials as well as their implementation in fuel cells. Our current point of view, based on previous work in our group and others, is that there is little interest in finding the "perfect" molecular catalyst without an idea of how to make the best out of it. More generally, it is our idea that studying a catalyst destined for practical applications in a technologically irrelevant environment may be of great interest to elucidate mechanical aspects of the reaction but does not yield great insight as to the practicality of its use in real life. We hope to have shown in this introduction that the diversity of catalysts available and their intrinsic properties are such that it is now of interest to try and increase the technology-readiness level of some of these. In this thesis, we first consider the choice of a "champion" bio-inspired catalyst as well as the effects of catalytic ink formulation and ionomer implementation on catalytic activity, and look at the optimization of the environment of the catalyst on its activity. Then, we take a closer look at a particular type of electrode prepared during this project that shows qualitatively new results at high overpotentials and characterize the physical chemistry of its unique behaviour, rationalizing it with regard to previous results. Finally, we describe the implementation of those optimized electrodes in fully functional, noble metal-free PEMFCs.

Chapter I – Catalyst choice and effect of ionomer

In this first chapter, we present several techniques to characterize the molecular catalysts and their support materials described in the introduction, in particular the three DuBois catalysts on which this work focuses. We then take a close look at the use of Nafion, a PTFE-based ionomer which serves as a proton relay. Its use in fuel cell electrodes is as critical as it is problematic: Nafion can be detrimental to the activity of most catalytic sites but is required for good interfacing of the electrode with the proton-exchange membrane, and at the present time any molecular catalyst susceptible of integration has to be compatible with Nafion.

1. Characterization of the molecular catalysts

The three DuBois catalyst based electrodes presented in the introduction are shown together in Figure 1. In this part, electrodes containing these three catalysts are characterized, described and benchmarked.

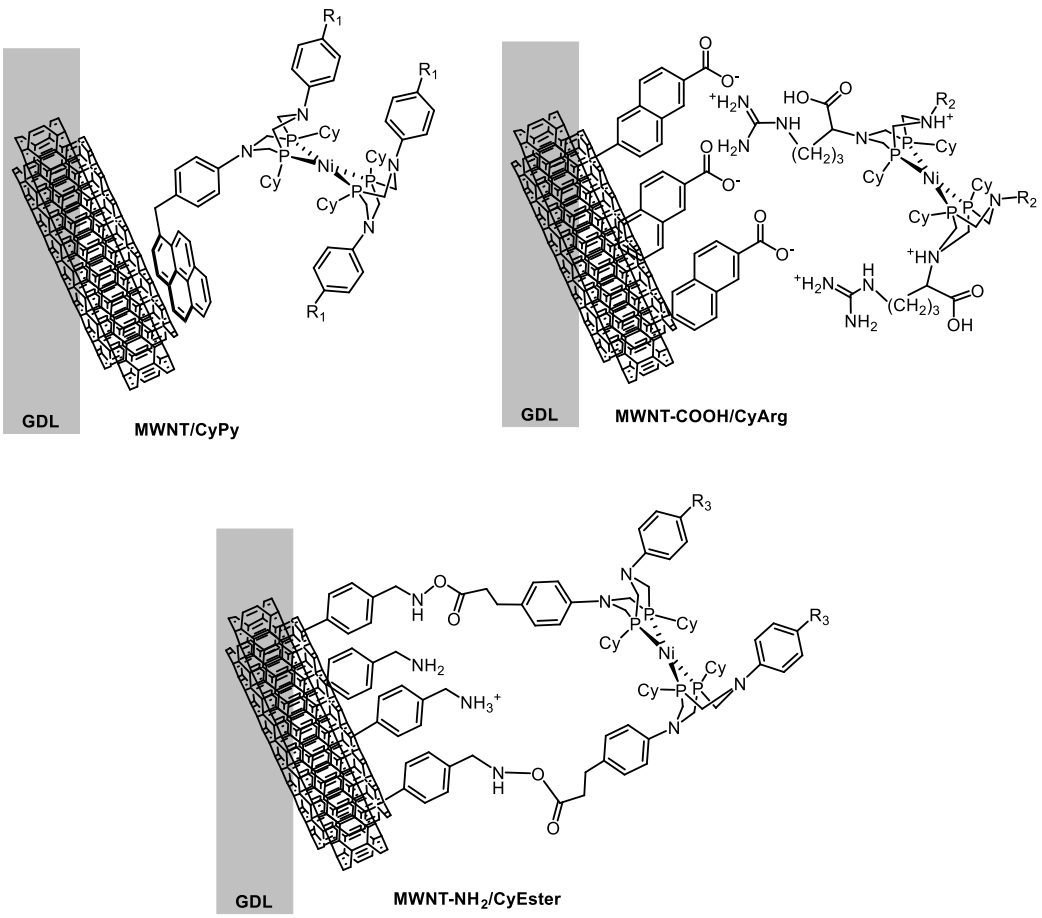

*Figure 1. Clockwise, from top left: MWNT/**CyPy**, MWNT-COOH/**CyArg** and MWNT-NH_2/**CyEster** deposited onto a GDL. R_1 = CH_2-pyrene, R_2 = Arginine, R_3 = Ph-CH_2CH_2COOH or Ph-CH_2CH_2COO-phtalimide*

a. Catalytic activity

The preparation of these three types of electrodes is different because of the intrinsic differences in the grafting strategies. It is described in detail in the experimental section, but hereafter is a succinct description for each electrode.

MWNT-NH_2/**CyEster** is prepared as previously described,[69] by first filtering a suspension of MWNT onto the GDL to form a mat onto which a diazonium salt is reduced to decorate the MWNT with amino functions, yielding MWNT-NH_2. This electrode is then soaked in a solution of **CyEster** in DMF in the presence of a weak base, 2,6-lutidine, to enable covalent amide bonding.

MWNT/**CyPy** is prepared by drop casting a suspension of the pristine MWNTs in EtOH onto the GDL, letting it dry and then drop casting a solution of **CyPy** in DCM onto the MWNT mat. This is in contrast with what was previously done in the group, where the MWNT were vacuum-filtered onto the GDL and the obtained electrode was soaked in a solution of the catalyst.[79] This new method is preferred as it allows easier quantification and control of the amount of **CyPy** deposited as well as economy of catalyst.

Finally, MWNT-COOH/**CyArg** is prepared as an all-in-one ink, by premixing the suspension of MWNT-COOH in ethanol with the solution of **CyArg** in pH 6 MES:HEPES buffered water. This ink is simply drop-casted onto the GDL and air-dried. Previous reports in our group used a similar method to that used for MWNT-**CyPy** in which the MWNT-COOH were deposited first,[80] however we have found better reproducibility with our current method.

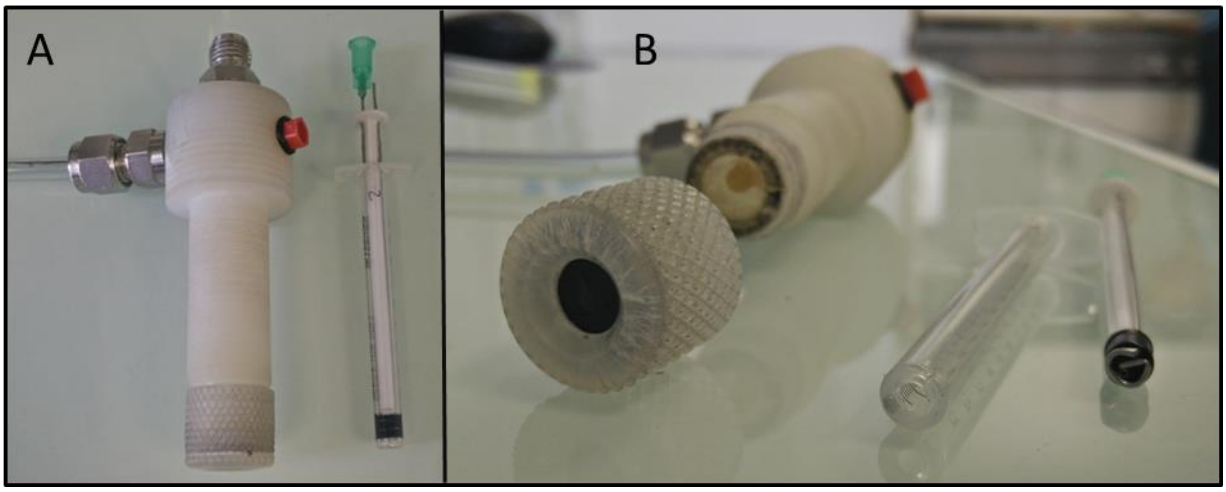

Figure 2. Comparison of the two half-cell setups, side (A) and front (B) views. Classical half-cell, S = 0.5 cm² on the left and so-called micro half-cell, S = 0.06 cm² on the right of each picture.

Catalytic activity is assessed through cyclic voltammetry experiments. A simple half-cell apparatus (see Figure 2) was made in house, with a small surface area (of the order of 0.06 cm², on the right in panels A and B, Figure 2).) which allows facile and efficient benchmarking while using very small amounts of catalyst. No notable changes in catalytic performance were observed compared to the previous experimental setup in our lab, a similar half-cell with a surface area of 0.5 cm² (on the left in panels A and B, Figure 2). In Figure 3, the catalytic behaviour of these catalytic materials is compared at pH 0.3 in aqueous 0.5M H_2SO_4 electrolyte, in the presence of a 100% atmosphere of H_2 gas fed through the back of the working electrode.

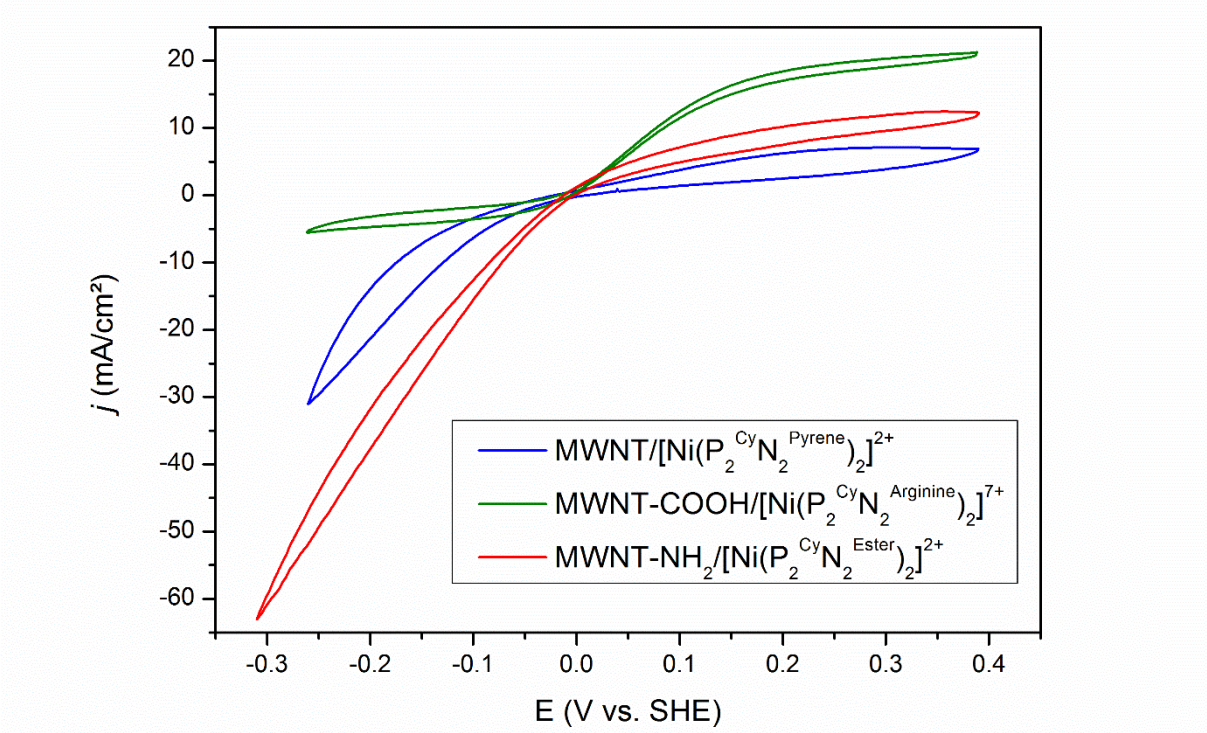

*Figure 3. Comparison of the catalytic behaviours of the three systems, **CyPy**, **CyEster** and **CyArg**, grafted on their respective nanotubes: MWNT, MWNT-NH_2, MWNT-COOH. Half-cell setup, S = 0.063 cm², electrolyte is H_2SO_4 0.5 M in H_2O, pH 0.3, 298K and P_{H2} = 1 atm.*

MWNT/**CyPy** and MWNT-NH_2/**CyEster** display similar shapes with an overall reversible HER/HOR catalytic ability, and a similar catalytic bias towards the HER. This is in line with previous results from our group.[72,76,81] The current densities of MWNT-NH_2/**CyEster** are larger for both HER and HOR, despite similar site loadings. MWNT-COOH/**CyArg**, on the other hand, while it still displays reversible catalytic activity, shows a very strong bias for HOR, as described in solution at this pH[52,82] or after grafting onto SWNT-COOH.[80] However, catalytic HOR activity reaches a catalytic plateau above 100 mV of overpotential.

b. Catalyst loading

In order to assess the ratio between deposited and electrochemically active catalysts, one can use electrochemistry in non-catalytic conditions. Collecting a CV of a catalytic material in an aprotic, degassed solvent such as CH_3CN allows to quantify the amount of electrochemically connected catalysts through integration of the reversible redox cycles at the active site. In Figure 4, this is exemplified for MWNT-COOH/**CyArg**.

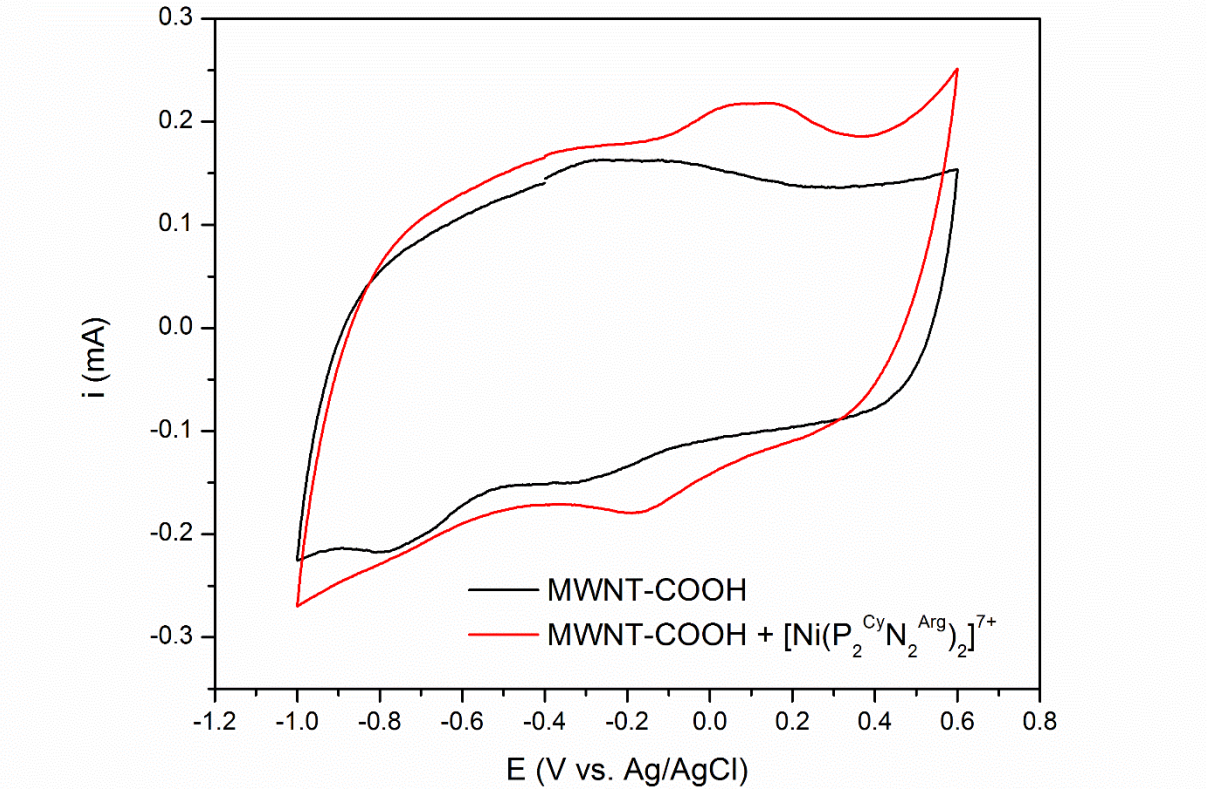

*Figure 4. CVs of MWNT-COOH deposited on a GDL with and without **CyArg** in dry CH_3CN. Half-cell setup, S = 0.063 cm², electrolyte salt is nBu_4NBF_4 0.1 M, 298K and N_2 is fed in the back of the working electrode.*

By measuring Q, the charge passed during a reversible electrochemical phenomenon inherent to the catalyst and knowing the surface S of the electrode, the site loading (SL)[18] can be obtained through the following relation, for a process with n electrons, with SL in mol/cm², S in cm², Q in C and *F* the Faraday constant:

$$SL = \frac{Q}{n\mathcal{F}S}$$

When catalytic loadings are given in this manuscript, this is how they have been assessed unless otherwise mentioned. We assessed SL both before and after catalysis for most of our electrodes and unless otherwise mentioned, the amount of catalyst measured by this method after turning

over for one hour was virtually identical to that before turnover. Hence, current losses over time, if observed, are rather explained by phenomena happening in the nanostructure of the electrode, such as structural failure or flooding rather than degradation or washing off of the catalyst.

Figure 4 shows CVs of the bare MWNT-COOH (black) and of MWNT-COOH/**CyArg** (red) deposited onto a GDL. The reversible phenomenon around $E_{1/2}$ = 0.05 V vs. Ag/AgCl is attributed to the almost superposed Ni^{II}/Ni^{I} and Ni^{I}/Ni^{0} redox couples[80] and its integration yields SL = 2.5 nmol/cm². The initial amount of deposited catalyst was about 50 nmol/cm², meaning that about 5 % of the deposited catalyst is connected. This could be a target for improvement, however the material used, carbon nanotubes, is already notoriously conductive.

Interestingly, this is coherent with a report by Pascale Chenevier et al. on the preparation of bio-hybrid materials employing hydrogenase enzymes which estimated that while the enzyme constituted 40 % in mass of the bio-hybrid, less than 1 % of the expected catalytic activity was observed.[83] The same problem was reported very recently by the group of Elisabeth Lojou, for the grafting of a hydrogenase onto carbon nanotubes, with only 10 % of the loaded enzyme that is electronically connected.[84] It seems that grafting of enzymes or molecular catalysts is not a trivial task and it would be interesting to investigate further the reasons for these low yields.

As for the previous observation (Figure 3) that the HER and HOR current densities of MWNT-NH_2/**CyEster** were larger than that of MWNT/**CyPy**, SL determination yielded values of 3.1 and 2.7 nmol/cm², respectively. While this can account for a portion of the observed difference in current, it cannot be the sole explanation. **CyEster** has not been studied in solution and hence we cannot compare the intrinsic catalytic properties of the two non-grafted catalysts. Perhaps the much more hydrophilic MWNT-NH_2/**CyEster** assembly allows for a better penetration of the electrolyte within the carbon nanotube electrode, hence allowing better current densities for both HOR and HER, whereas the hydrophobic MWNT/**CyPy** assembly rejects electrolyte strongly. Furthermore, when comparing the SLs, it has to be taken in consideration that **CyPy** is expected to be found homogenously throughout the thickness of the electrode while expect the majority of **CyEster** is expected to be positioned on the surface, due to the differences in grafting strategies described above. Hence, a number of the **CyPy** sites might not be catalytically active at all if not properly interfaced with the electrolyte.

c. Molecular structure of the active sites: XAS studies

Among the questions frequently asked about molecular catalysts is whether the molecular motif is retained, whole and properly grafted, throughout the catalytic process. A first indicator could be whether the catalytic activity remains stable over time: if it does not, this could indicate a degradation or a washing off of the molecular catalyst. However, stable activity, as reviewed for molecular catalysts for synthesis of solar fuels,[85,86] does not necessarily mean a stable molecular catalyst. In some cases, the formation of nanoparticles of metal or metal oxide was shown and it was proven that they contributed to the observed activity. Therefore, the structure of the active sites needs to be characterized both after grafting and in turnover conditions (operando) or post-operando. In our case however the formation of Ni^0 or Ni oxide is unlikely at the experimental potentials and pH, given the Pourbaix diagram of Ni.[87]

X-ray absorption near edge structure (XANES) and extended X-ray fine structure (EXAFS), the two complementary parts of X-ray absorption spectroscopy (XAS), are techniques of choice for characterizing molecular catalysts based on a single metal atom as they afford great insight on its redox state and the atomic structure around the metallic centre.

Characterization of some of our catalytic materials was done in collaboration with Paul Kubella from the group of Holger Dau at Freie Universität Berlin and Solène Gentil, working both in our group and the group of Alan Le Goff at DCM, Université Grenoble Alpes. Table 1 below describes some of the electrodes and reference samples measured during a visit at the BESSY-II synchrotron at the Helmholtz Zentrum Berlin in November 2015. **CyPy** was already characterized in previous work from our group.[72]

	Sample name	***Sample composition***
Reference samples	**CyEster** P4 powder	$[Ni^{II}(P^{Cy}_2N^{Ester}_2)_2]^{2+}$ powder
	CyEster P2 powder	$[Ni^{II}(P^{Cy}_2N^{Ester}_2)(CH_3CN)_2]^{2+}$ powder
	Ni-hexaaqua	$[Ni^{II}(H_2O)_6]^{2+}$
Electrode samples	**CyEster** grafted	$[Ni^{II}(P^{Cy}_2N^{Ester}_2)_2]^{2+}$ on MWNT-NH_2
	CyEster grafted after turnover	$[Ni^{II}(P^{Cy}_2N^{Ester}_2)_2]^{2+}$ on MWNT-NH_2 after 1h turnover for HOR at pH = 0.3

Table 1. Some of the samples characterized in XAS. Reference samples are powders of the complexes as synthesized. Electrode samples are either before or after one hour of turnover at 300mV overpotential for HOR in aqueous H_2SO_4 at pH = 0.3

The data from the electrode samples was fitted with a linear combination of the relevant reference samples. In this table, P2 and P4 refer to the amount of bis-diphosphine ligands coordinated to the metal, respectively one and two. In the case of the P2 coordination, the two vacant coordination sites are expected to be occupied by solvent molecules, in our case H_2O or CH_3CN. The goals of this study were as follows: first, to confirm that Ni remained complexed and did not aggregate in nanoparticles; second, to characterize the first coordination sphere of Ni right after grafting and to compare it to that of the well-characterized complex powder; third, to assess any changes in coordination sphere after extended catalytic turnover. These three goals were attained as described below. It should be noted however that XAS cannot be used to provide information on the nature of the grafting of the complexes to the surface as the pendent anchoring groups are situated too far outside of the coordination sphere of Ni. However, this limitation can also be an advantage as this technique is insensitive to the support material, and allows us to use spectra of powdered complexes to fit the data of grafted complexes.

iii. Molecular aspect of the catalytic sites

The first information obtained from the XAS spectra comes from the energy of the K pre-edge of Ni in our samples which, at a value of about 8340 eV is consistent with an isolated Ni^{2+} ion and not Ni nanoparticles. This was true for all samples, both before and after catalysis, confirming that Ni retained its ionic character. Thanks to a calibration curve relating the Ni oxidation number to the edge position (Figure 5), the average oxidation number for each sample was calculated. Values fell between + 1.6 and + 2.5, also in accordance with a DuBois type complex.[44,46,47] The exact values for each sample are tabulated in the annex to this chapter.

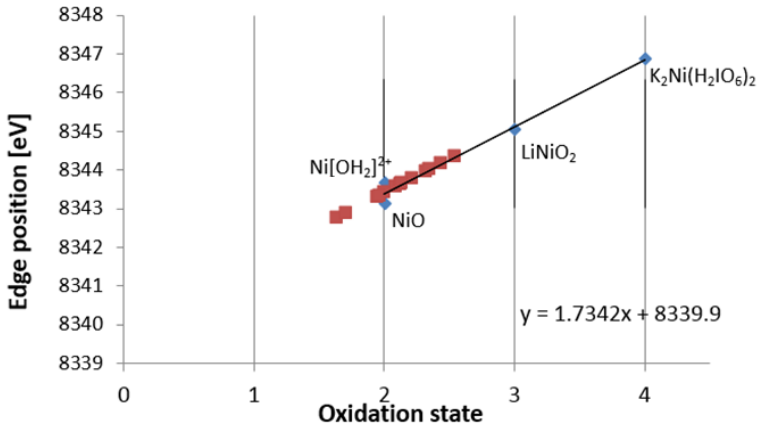

Figure 5. Calibration curve for calculation of Ni-oxidation states, defined by a linear fit to Ni integral edge positions of reference materials (blue). In red are shown the edge position of the samples.

In order to elucidate the molecular structure of the complexes on the surface, three reference spectra of standalone complexes, presented in Figure 6, were measured. The fits of the reference

spectra as well as the numerical values for number and distance of the first coordinating neighbours of Ni can be found in the annex to this chapter. The data of the samples was fitted as a linear combination of the Ni-hexaaaqua coordination and either the P2 or P4 coordination.

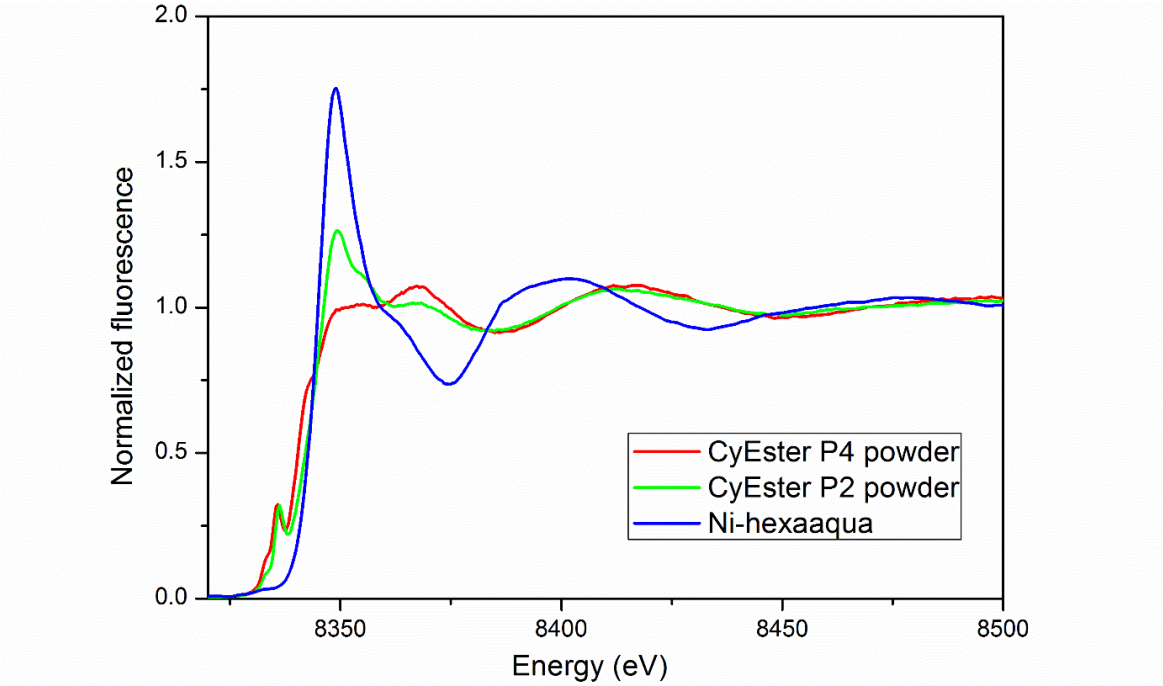

Figure 6. Ni-K edge XAS spectra of the reference samples.

iv. Changes in the coordination sphere after grafting

Two questions relevant to DuBois catalysts are whether the coordination sphere remains intact when they are grafted, and what the structure of the catalytically active species is.

For **CyEster**, it was thought possible from previous work in our group[76] that instead of systematically preserving the P4 coordination state, a P2 species could be formed with the loss of one ligand, replaced by solvent molecules, possibly enabling easier coordination of H_2. This was of particular interest in the case of the so-called "bottom-up" preparation of the MWNT-NH_2/**CyEster** electrodes, in which nanotubes are first modified to bear NH_2 functions, then the amide bond with the ligand is created and finally the metal salt is added for complexation (see Figure 7).

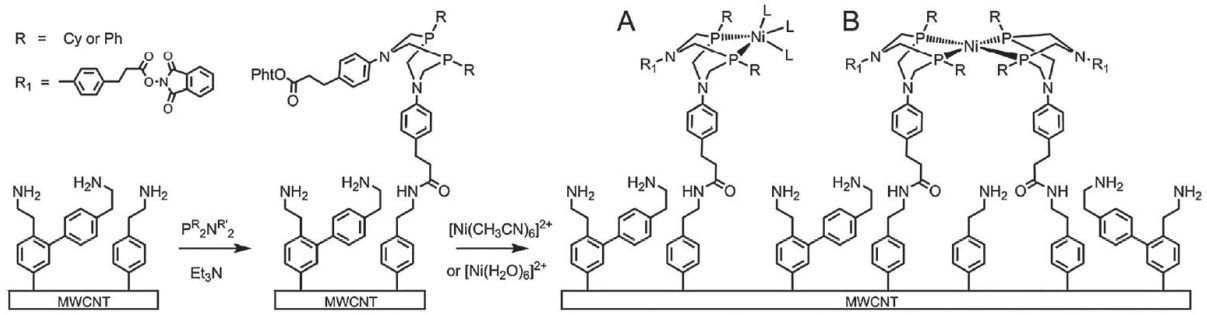

*Figure 7. Bottom-up preparation of the MWNT-NH₂/**CyEster** electrode, taken from ref.[76] A: P2 coordination; B: P4 coordination. L is a solvent molecule.*

To elucidate the coordination type on the electrode surface, the data was fitted with two linear combinations of reference spectra : **CyEster** P2 and Ni-hexaaqua ; and **CyEster** P4 and Ni-hexaaqua (see Figure 8 and 0). Ni-hexaaqua is both a precursor to the complex and a possible product of degradation, which is was it was used in the fit.

Complex % in the respective fit

	CyEster P4	**CyEster P2**
***CyEster** P2*	-	100
***CyEster** P4*	100	-
***CyEster** grafted*	36,3	52,4

*Table 2. Percentage of the either P2 or P4 resulting from the linear combination with the spectra of the Ni-hexaaqua-complex using LC=X*A+Y*B with X+Y=1, A being the spectrum of the P2 or P4 complex and B being the spectrum of the hexaaqua-Nickel-complex. The remaining % missing from the 100 is the amount of Ni-hexaaqua-complex.*

As shown in Figure 8, the spectrum of the grafted **CyEster** is best fitted with a linear combination of a P4 type coordination and Ni-hexaaqua. However, it appears to fall somewhere in between the P4 and P2 LC fits, which could indicate a mixture of coordination types. In both cases, a significant part of the fit is composed of Ni-hexaaqua, in line with previous results for **CyPy**. Further work will include a fitting of this data with a three-part linear combination of P4, P2 and Ni-hexaaqua coordinations, however this has to be done with caution as over-interpretation is easy when combining three functions instead of two.

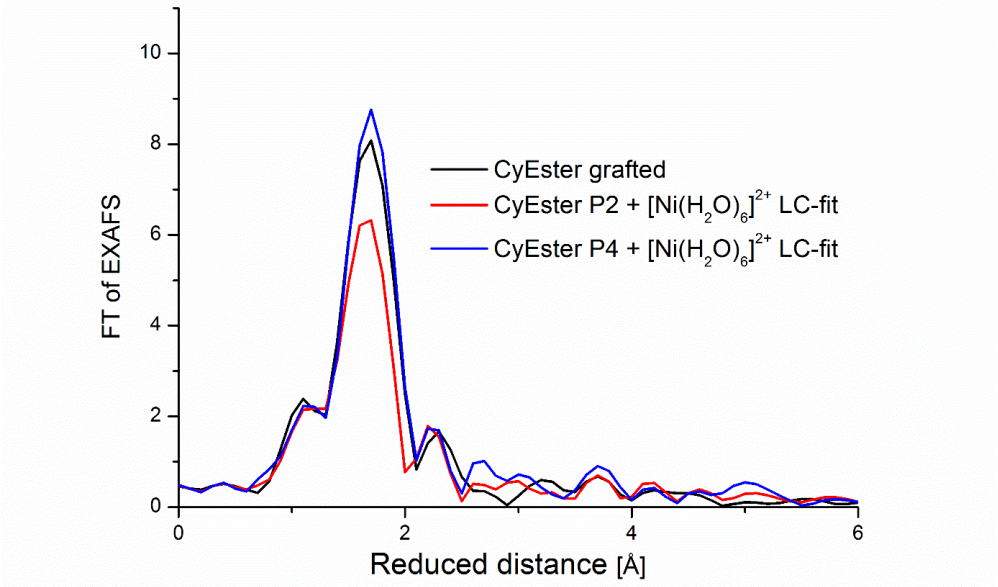

*Figure 8. FT of EXAFS spectra of the measured spectrum of grafted **CyEster** (black) with the two fits resulting from linear combination of **CyEster** P2 [36,3%] (red) and **CyEster** P4 [52,4%] (blue) with the Ni-hexaaqua-complex. LC = linear combination*

v. Evolution of the catalytic sites after turnover

We were interested in knowing whether the catalysts retained their coordination state after turnover. We measured XAS spectra of samples before and after catalysis in the conditions described in Table 1. In the case of the MWNT-NH_2/**CyEster** electrodes, data showed that the complex remained in a P4 or P2 coordination after 1h of HOR turnover, a very encouraging result as to the stability of such molecular catalysts which is often a point of concern for industrial applications. The same was observed for **CyPy** in previous work from our group.[72]

	Complex % in the respective fit	
	CyEster P4	**CyEster P2**
***CyEster** grafted*	36,3	52,4
***CyEster** after turnover*	15,0	23,6

*Table 3. Percentage of the either P2 or P4 resulting from the linear combination with the spectra of the Ni-hexaaqua-complex using LC=X*A+Y*B with X+Y=1, A being the spectrum of the P2 or P4 complex and B being the spectrum of the hexaaqua-Nickel-complex. The remaining % missing from the 100 is the amount of Ni-hexaaqua-complex.*

It should be noted that in the case of **CyEster**, a lesser amount of complex was observed after turnover. In Table 3, we see that the ratio of P2 or P4 complex used to fit the data after turnover rather than before is divided by two. However the catalytic activity was stable over an hour, which leads us to think that it is the result of the washing of inactive, probably not grafted **CyEster** complexes.

vi. Conclusions of the XAS study

This study proved that, like it was shown for **CyPy**, **CyEster** retains a molecular structure when grafted, and after an hour of turnover for HOR at 300 mV overpotential. It is an important trait of this family of catalyst that is very valuable when considering their integration in technological devices. By combining it with quantitative methods such as ICP, XPS or the above-presented CV quantification of active sites, a good picture of the state of catalytic sites within an electrode can be obtained. Similar studies for MWNT-COOH/**CyArg** electrodes are under way.

2. Effect of ionomer on activity

In order to ensure efficient proton transfer from catalytic sites to the proton-exchange membrane of a PEMFC, an ionomer is usually added to the catalytic ink. Although several families of ionomers exist,[88] we here focus on the overwhelmingly most used to date, Nafion.

a. Generalities about Nafion

Nafion is a block copolymer that consists of a hydrophobic PTFE backbone branched with sulfonated PTFE side-chains (top, Figure 9). By itself, as it slowly dries in the presence of water, it is organized at the micrometre scale in hydrophobic and hydrophilic regions as depicted in Figure 9.[89] The hydrophilic sulfonated side chains assemble around water to form so-called water channels, which can be more or less interconnected depending on the degree of hydration of the polymer as well as the length of the side chains. These water channels present great proton transport capability. Indeed, in addition to the classical transport of H^+ in water through the Grotthuss mechanism, the close vicinity of the sulfonate (SO_3^-) functions enables faster proton hopping. The hydrophobic backbone of Nafion is cohesive enough to enable the formulation of Nafion as a self-standing membrane of quite uniform thickness, from about 10 to 100 µm. These properties along with the strong electronic insulation properties of the self-standing Nafion membrane and is relatively good impermeableness to H_2 and O_2 gas made it a good cation-specific membrane for fuel cell applications where insulation is required between the anode and cathode. Furthermore, it is soluble in a mixture of lower aliphatic alcohols, which enables its mixing within catalytic inks prior to deposition. This ensures a continuous proton transporting relay throughout the thickness of both anode and cathode *via* the membrane. It is this duality of ionomer and membrane formulations which makes Nafion such an attractive ionomer for technological applications.

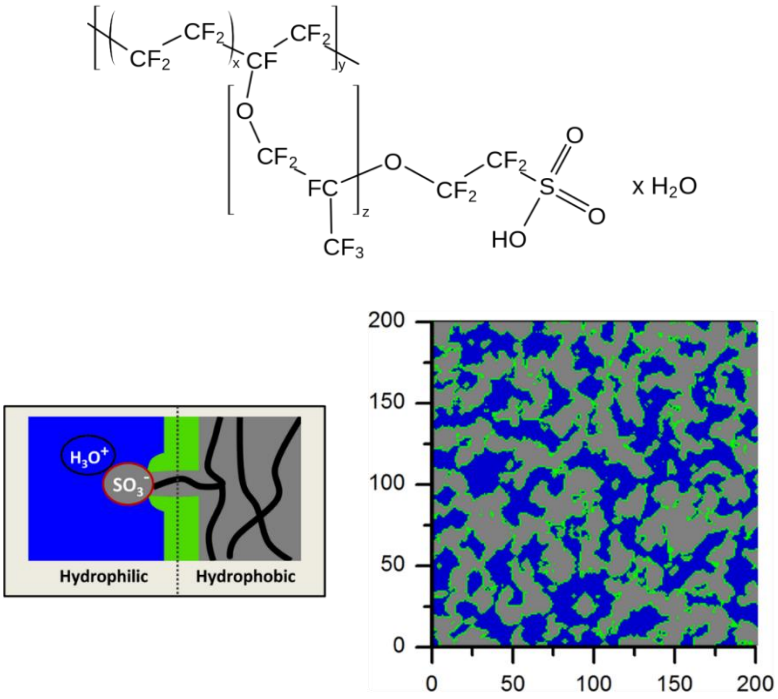

Figure 9. Top, molecular structure of Nafion. Bottom left, schematic representation of the hydrophilic and hydrophobic domains of Nafion. Bottom right, two-dimensional cross-section of the modelled three dimensional cubic structure of Nafion with an edge length of 200 segments. One segment of the mesh corresponds to a cube with 2.1 Å edge length. Grey area: solid phase. Blue area: aqueous phase. Green area: Intermediate phase. Reproduced from refs[90,91]

Originally chosen because of its synergetic behaviour in whole PEMFCs with Pt-based catalysts,[19] Nafion has been the electrolyte of choice for catalytic ink formulation at both the anode and cathode. However, as reported repeatedly in literature mostly for Pt-based cathodes for the ORR,[89-94] the addition of Nafion ionomer to electrodes is a tricky process as its presence often hinders mass transport of gas within the electrode thickness as well as to and from the Pt nanoparticles, in turn hindering activity.[95] In a report by our group on the implementation of a **CyPy** electrode in a compact PEMFC,[72] Nafion ionomer was added to the catalytic ink for PEMFC implementation but not for half-cell experiments. While the PEMFC functioned, the power output (23 µW/cm²) was very low compared to what could be expected from the maximum current densities in half cell measurements (1 mA/cm²). This is attributed, in retrospect, to a detrimental effect of Nafion ionomer in the ink. A seemingly easy solution would be to get rid of Nafion ionomer altogether in half-cell studies, however it is necessary to the proper function of PEMFCs, in which the proton relay depends entirely on ionomer in the absence of electrolyte.

b. Effect of Nafion on bio-inspired catalytic materials

Simple electrochemical experiments were designed in order to assess the effect of Nafion as an ionomer within our catalytic inks. For Pt-based catalysts, the optimum is described to be around 50 wt% in a whole PEMFC and below 20 wt% in half-cell, electrolytic conditions, for carbon materials with specific surface areas similar to that of the carbon nanotubes we use. However, for high specific area carbon support materials such as Ketjenblack, the optimum stands around 70 wt%.[95] The amount of Nafion added, in our case equal to the mass of the carbon support material so that $\frac{m_{Nafion}}{m_{MWNT}} = 100\ wt\%$, was chosen in line with previous work in our group.[76] In Chapter II, we discuss the ratio of Nafion used for bio-inspired systems.

We were interested in characterising the behaviour of all three systems in the presence of Nafion in order to select a system suitable for integration. Potential step chronoamperometry (PS-CA) experiments were designed in which the electrodes were first poised at a reductive potential, -100 mV vs. SHE, to trigger HER then at an oxidative potential, +300 mV, for HOR. Capacitive current is observed as the potential is switched but decays very quickly (1-2 seconds) to display stable HER and HOR currents over the time of the experiments. This was done for all three systems, as described hereafter.

Table 4 presents the Ni/C atomic ratios, carbon nanotube loading and effect of Nafion on HOR catalytic current for each system. The overall loadings in catalyst and nanotube of the three systems are comparable, differing at most by a factor of two. The SLs determined by CV are also shown, proving that even if the MWNT/**CyPy** electrode is much richer in Ni, it still has a SL comparable to that of the other two systems. The Ni/C ratio is measured by energy dispersive X-ray spectroscopy (EDX).

Electrode	*MWNT-NH_2/**CyEster***	*MWNT-COOH/**CyArg***	*MWNT/**CyPy***
***Ni/C atomic ratio** (%)*	0.34	0.31	0.65
***Site loading** (nmol/cm²)*	2.7	2.5	3.1
***Nanotube loading** (mg.cm⁻²)*	0.53	0.38	0.38
***J_{ox} w/o Nafion** (mA.cm⁻²)*	2.1	22.5	2.3
***J_{ox} w/ Nafion** (mA.cm⁻²)*	2.2	21.2	0.0

Table 4. EDX measurements and H_2 oxidation current densities of the three systems. Ni/C ratio is given in the Nafion-containing electrodes. J_{ox} is given at 300mV vs. NHE, after stabilization of the current.

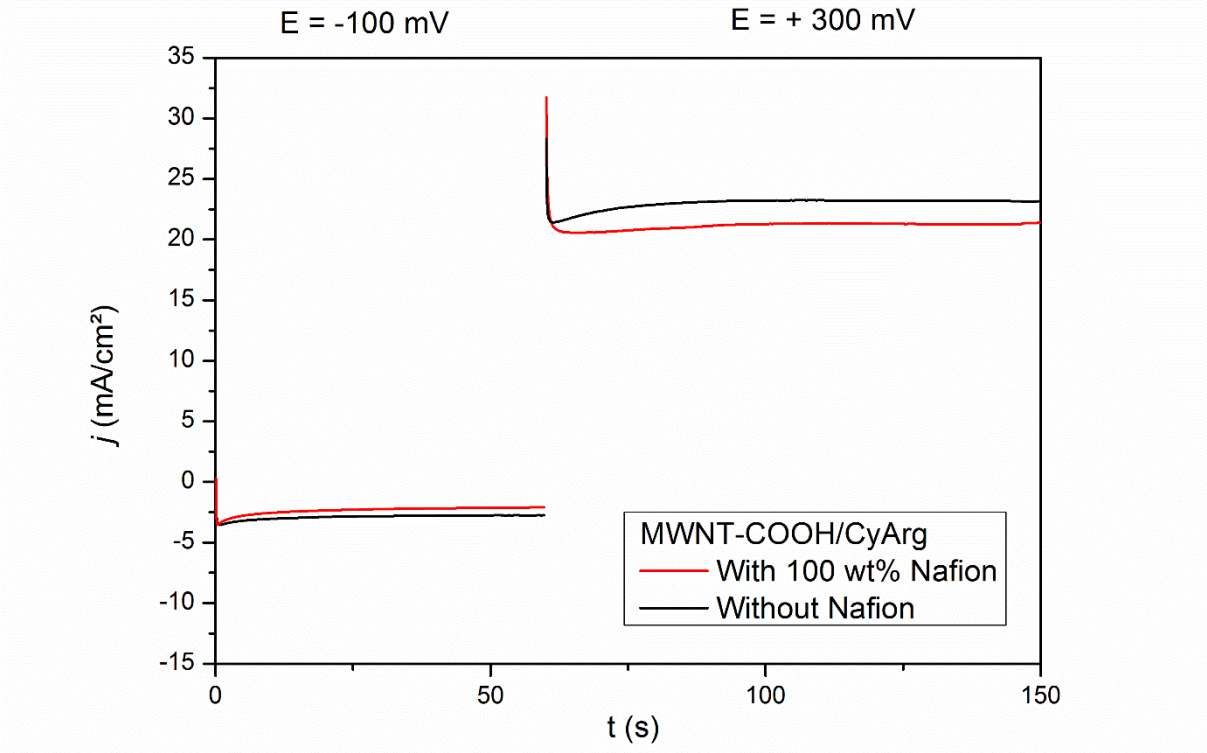

*Figure 10. Potential step chronoamperometry of MWNT-COOH/**CyArg** with (red) and without (black) Nafion. Potentials are quoted vs. SHE. Half-cell setup, S = 0.063 cm², electrolyte is H_2SO_4 0.5 M in H_2O, pH 0.3, 298K and P_{H2} = 1 atm.*

MWNT-COOH/**CyArg** (Figure 10) is more efficient for HOR than for HER, as reported previously.[82] When 100 wt% of Nafion is incorporated in the MWNT-COOH/**CyArg** ink, both H_2 production and uptake catalytic currents remain virtually identical to that of the electrode without Nafion, with only a slight drop in HOR. Transient currents in oxidation are very brief and a large oxidation current is recorded. From this, we can conclude that the addition of Nafion does not prevent H_2 diffusion to and from the catalyst throughout the thickness of the active layer. However, the phenomena at play here are slightly more intricate than meets the eye and a more thorough characterization of the effect of Nafion on catalysis of this system is presented in Chapter III.

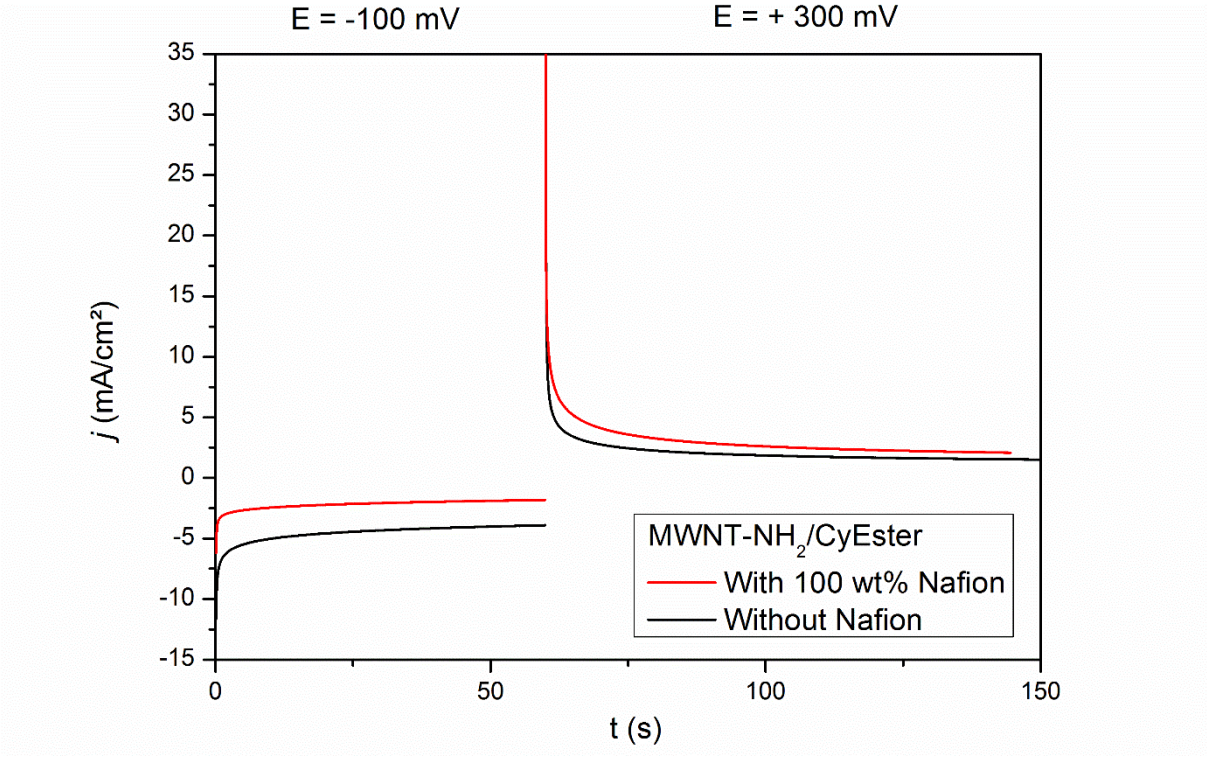

*Figure 11. Potential step chronoamperometry of MWNT-NH_2/**CyEster** with (red) and without (black) Nafion. Potentials are quoted vs. SHE. Half-cell setup, S = 0.063 cm^2, electrolyte is H_2SO_4 0.5 M in H_2O, pH 0.3, 298K and P_{H2} = 1 atm.*

MWNT-NH_2/**CyEster** (Figure 11) shows a different picture. The catalyst is more efficient in reduction than in oxidation, as previously described.[81] Surprisingly, HER currents are somewhat hindered in the presence of Nafion. This could be explained by the fact that adding Nafion to an electrode makes it more hydrophobic. When Nafion is incorporated in the layer, the current for HOR is slightly enhanced, which can be explained by a facilitated proton removal from the active site, allowing H_2 to coordinate more easily.

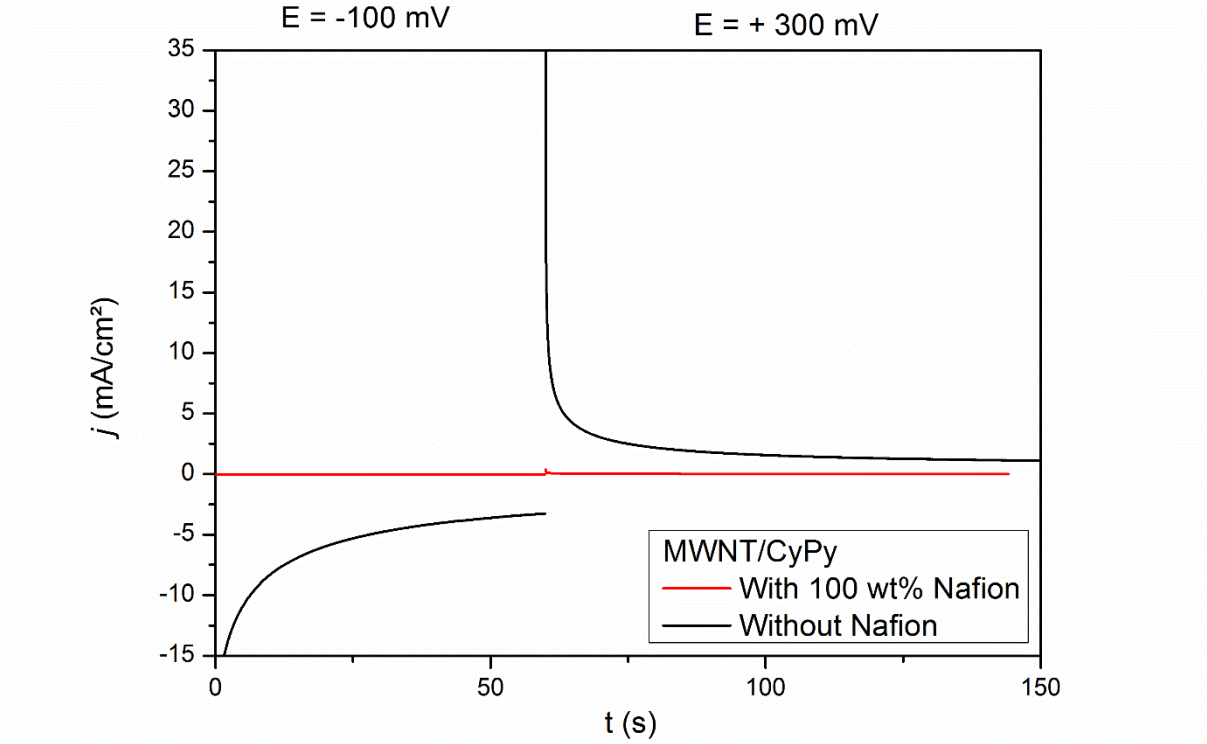

*Figure 12. Potential step chronoamperometry of MWNT/**CyPy** with (red) and without (black) Nafion. Potentials are quoted vs. SHE. Half-cell setup, S = 0.063 cm², electrolyte is H_2SO_4 0.5 M in H_2O, pH 0.3, 298K and P_{H2} = 1 atm.*

Finally, MWNT/**CyPy** (Figure 12) shows a totally different behaviour. This electrode, like MWNT-NH_2/**CyEster**, has a bias for HER. In this case, when Nafion is added, both HER and HOR currents become null. This can be explained either by a poor access of H^+ and H_2 to the catalyst through the Nafion layer, or by a poor electronic connection of catalysts to MWNTs in the presence of Nafion. Consequently, the catalysts are partly or entirely inactivated.

This behaviour of MWNT-NH_2/**CyEster** and MWNT-COOH/**CyArg** in which the electrodes retain strong HOR in the presence of Nafion is an important trait of these systems, very valuable for integration, as it will enable a good proton transport connection between the electrode and the membrane. Such data is important in understanding that necessary steps towards integration can be detrimental to the standalone anode but beneficial to the system as whole: only a Nafion-containing electrode will be capable of exchanging protons in a whole cell, which might come at the price of slightly lower HOR current densities in half-cell benchmarking.

A major difference between these systems is the functionalization of the nanotubes that induces opposite surface charges of the support material: positive for MWNT-NH_2/**CyEster**, negative for MWNT-COOH/**CyArg** and neutral for MWNT/**CyPy**, rendering the MWNT-COOH and MWNT-NH_2 quite hydrophilic while the bare MWNTs are very hydrophobic. We hypothesize

that these differences can be crucial in the structural organization of the ionomer, nanotubes and catalyst mixture during the casting of the catalytic ink.

In order to verify whether the variation in the effect of Nafion was due to the nanotubes or to the catalysts, control experiments were led in which each catalyst was deposited onto the three types of nanotubes. Although this was not expected to yield great catalytic systems – the grafting methods had been designed as specific nanotube/catalyst interactions – this was a good way to assess what caused this effect of Nafion. Table 5 presents the effect of the addition of Nafion on HOR for those controls (the corresponding CA plots can be found in the annex to this chapter).

Support / ***Catalyst***	***MWNT***	***MWNT-NH_2***	***MWNT-COOH***
CyPy	-	-	-
CyEster	-	+	-
CyArg	-	-	+

Table 5. Effect of Nafion addition on HOR for 9 different nanotube/catalyst pairs: kills all activity (-) or retains activity (+).

The first apparent observation from the above table is that if at least one of the members of the grafting interaction is hydrophobic, whether it is the pristine MWNT or **CyPy**, the addition of Nafion ionomer kills all activity (red, Table 5). In the presence of pristine MWNTs, the hydrophobic chains of Nafion are expected to wrap around the hydrophobic surface of MWNTs for which they have a strong affinity.[96] Strong Nafion backbone adsorption was indeed shown on hydrophobic surfaces,[93,97] where it even produced oriented lamellar Nafion phases. Such a self-assembly process likely blocks access of protons and H_2 to the catalysts, as previously proposed for ultra-small Pt loadings on carbon black.[92] In the MWNT/**CyPy** system, the competing interaction between the hydrophobic PTFE Nafion backbone and the pristine MWNTs can also result in the displacement of the π-stacked catalysts from the MWNTs,[92] so that most catalysts lose electronic contact to the electrode. In the case of **CyPy** onto hydrophilic nanotubes, it is expected that the very hydrophobic **CyPy** molecule will have more affinity for the hydrophobic domains of Nafion than for the nanotube and will end up electronically disconnected.

For hydrophilic nanotube/catalyst pairs (blue, Table 5), two behaviours are observed. In the first case, if the interaction is not very strong, that is for **CyEster** on MWNT-COOH and **CyArg**

on MWNT-NH_2, the addition of Nafion also kills the activity. In this case, we can expect the weak interaction to be displaced by the hydrophilic parts of Nafion. Hence, the only case in which the addition of Nafion does not hinder or kill HOR activity is when hydrophilic catalysts interact strongly with hydrophilic nanotubes. In this case, we expect the catalyst and nanotube to remain intimately connected even in the presence of Nafion and to be wrapped as a whole by the hydrophilic part of Nafion, retaining electronic contact between the catalyst and nanotube and conveniently arranging the hydrophilic domains of Nafion around the catalytic sites, placing them at an ideal triple-point for catalysis.

c. Nafion structuration around carbon nanotubes

A further remark is that on MWNT-NH_2 nanotubes, the addition of Nafion hinders HER catalytic activity. At pH 0, the amine functions of the MWNT-NH_2 are expected to be protonated and hence, the nanotube surface would be polycationic. In this case, the anionic part of the Nafion polymer and the cationic MWNT-NH_2 could assemble tightly, as classically observed for all opposite charge polyelectrolyte systems,[98] and such a strong interaction would highly impact the local Nafion structure, driving the organization of Nafion concentrically around the nanotubes (Figure 13, middle panel). In this configuration, the electrolyte and H^+ transport through the PTFE backbone of Nafion could be limited.[90,91] Therefore, such a concentric organization of Nafion around nanotubes could block the H^+ feed and explain the diminution of HER current. Figure 13 pictures a possible Nafion nanostructure around the catalyst-bearing nanotubes as a function of surface charge and hydrophilicity, as supported by our data and similar reports in literature.[99-102] This is but a hypothetical model and will require more direct evidence for validation or rebuttal.

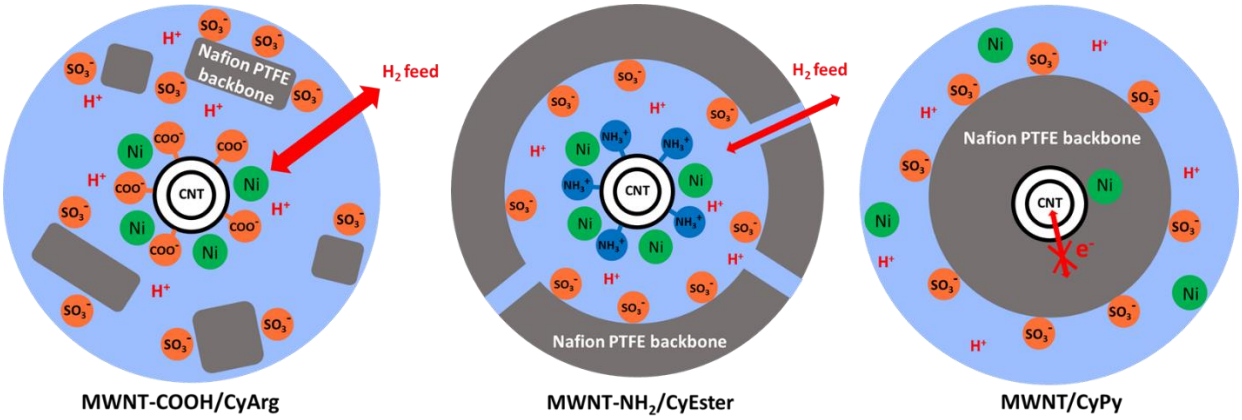

Figure 13. Cross-section schemes representing the hypothesized Nafion arrangement around the MWNTs (white) in the different composites at the mesoscale. The hydrophobic Nafion backbone (PTFE) is shown in grey and hydrophilic domains of the catalytic layers appear in blue.

Scanning electron microscopy (SEM) images in Figure 14 show the aspect of the three systems in the presence of Nafion at the micrometre scale (top pictures) and at the scale of a couple hundreds of nanometres (bottom). For a similar carbon areal loading, MWNT-COOH/**CyArg** displays a thickness (~ 10 µm) five times greater than that of the other systems (~ 2 µm). This porous structure is more suitable for gas and electrolyte diffusion. The nanotubes appear to be stratified in a layered, organised structure which is not found for the other two systems.

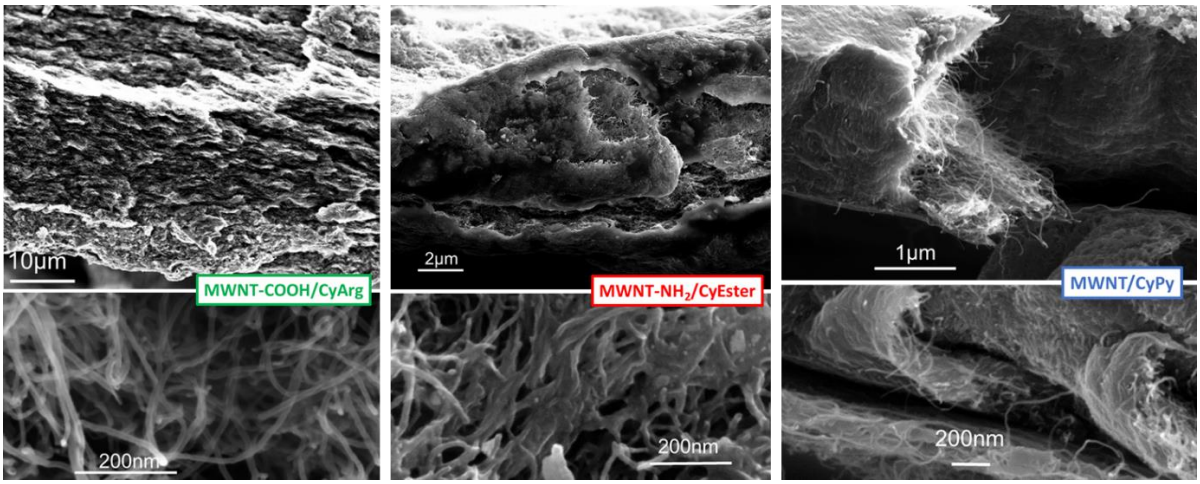

*Figure 14. SEM images of the three systems. From left to right: MWNT-COOH/**CyArg**, MWNT-NH_2/**CyEster** and MWNT/**CyPy**.*

Looking more closely at individual nanotubes in the composites (bottom pictures, Figure 14), differences are observed in the association of the nanotubes and Nafion. The MWNT-COOH/**CyArg** appear loosely arranged in balls of entangled nanotubes and Nafion while in MWNT-NH_2/**CyEster** and MWNT/**CyPy**, nanotubes are wrapped in a Nafion matrix to form a packed layer. Furthermore, while the nanotubes in MWNT/**CyPy** seem to be globally entrapped in a polymeric layer, it seems that the nanotubes in MWNT-COOH/**CyEster** are individually wrapped in a polymeric sheath, which supports the model presented in Figure 13.

d. Comparison with colloidal Pt nanoparticles

In order to elucidate whether some part of the effect of Nafion was due to the molecular nature of the catalyst, control experiments were led in which colloidal Pt nanoparticles were deposited onto the three types of nanotubes. The chemistry of the Pt nanoparticles is supposedly the same for the three types of nanotubes, therefore allowing for comparison of the nanotubes regardless of the nature of the catalyst. The Pt catalyst deposition was done in collaboration with the team of Dr Frédéric Maillard from LEPMI at Université Grenoble Alpes. Briefly, a colloidal suspension of Pt nanoparticles was deposited onto our three types of MWNT through an acidic

polyol synthesis. The final Pt loading on the electrode was 7 µg/cm², which falls into the category of ultra-low loading Pt electrodes (ULL-Pt, < 50µg/cm²). The effect of the addition of Nafion on those electrodes is presented in Figure 15 below. For this type of catalytic materials, we expect a strong bond between the Pt and carbon nanotube.[103] Hence, we do not expect to see any separation between the catalyst and support material when adding Nafion.

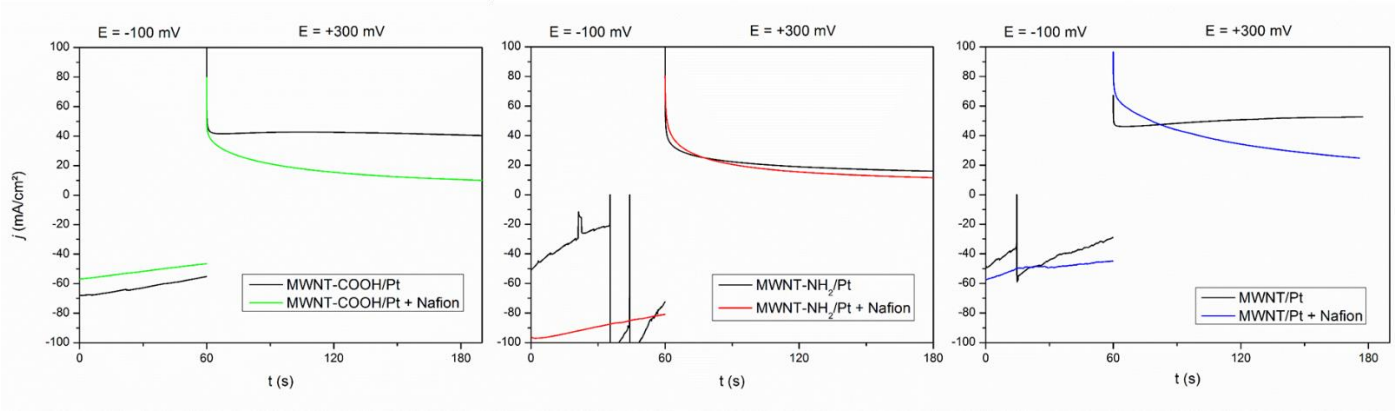

Figure 15. Potential step chronoamperometries of Pt on MWNT-COOH, MWNT-NH_2 and MWNT with (coloured) and without (black) 100 wt% Nafion. Potentials are quoted vs. SHE. Half-cell setup, S = 0.063 cm², electrolyte is H_2SO_4 0.5 M in H_2O, pH 0.3, 298K and P_{H2} = 1 atm.

For the MWNT-COOH/Pt electrode (left panel, Figure 15), HOR current in the absence of Nafion is stable around 40 mA/cm². When Nafion is added, the HER current does not change very much but the HOR current follows a slowly decreasing slope which stabilizes around 10 mA/cm², a four-fold decrease.

For the MWNT-NH_2/Pt electrode (middle panel, Figure 15), neither HER nor HOR currents seem to be affected by the addition of Nafion ionomer (HER current in the absence of Nafion is quite noisy because of the formation of H_2 bubbles, but its value is considered to be around 80 to 90 mA/cm²). Nafion has no effect on the HOR, in line with observations for the MWNT-NH_2/**CyEster** electrode, with currents stabilizing here around 15 to 20 mA/cm².

Finally, in the hydrophobic MWNT/Pt system (right panel, Figure 15), the addition of Nafion doesn't change the HER currents. However, it lowers HOR currents, in a similar way to the MWNT-COOH/Pt electrode, and as previously described for hydrophobic carbon-black, Pt/C systems exposed to Nafion.[95] The fact that the HER and HOR currents are not null in the presence of Nafion supports the hypothesis that, in the MWNT/**CyPy** system, Nafion displaces the π-π interaction and disconnects the catalysts while this does not happen with Pt.

It is likely that either the nature of the molecular catalyst or the nanotube/catalyst interaction plays a part in the effect of Nafion, as interpretation of the data for our bio-inspired catalysts cannot entirely be extrapolated to that of ULL-Pt catalysts. The MWNT-COOH/**CyArg** system in particular presents the very interesting characteristic behaviour of sustaining the addition of Nafion better than a Pt equivalent. Once these phenomena are fully understood, future work could aim at characterizing the behaviour of those Pt-based electrodes with and without Nafion in whole PEMFCs in order to see whether the observed effect of Nafion is still present, and confirm whether Nafion-containing electrodes perform better overall.

3. Choice of a bio-inspired catalytic system for optimization and integration

In this part, we hope to have shown that TOF and catalytic bias are not the only factors to take in account when choosing a catalytic system for future optimization and integration. Its compatibility with existing ionomer and membrane technologies is just as important. It made sense that the MWNT-COOH/**CyArg** system, which showed no sign of inhibition in the presence of Nafion and had the strongest bias for HOR, should be the one that we would integrate into whole fuel cells. Indeed, the importance of establishing a good proton relay to the membrane throughout the electrode thickness is critical for technological integration, when for half-cell experiments its role is less critical due to the excess of electrolyte. It should be noted that the negative effect of Nafion on the **CyPy**/MWNT system, not yet characterized, could be the reason why the performances of the whole noble metal-free fuel cell described in 2015 fell way beyond what was expected from the performances of the standalone benchmarking of the anode and cathode separately. An experimental model to extrapolate such “ideal” power outputs is proposed in Chapter IV.

4. Experimental section

Unless otherwise stated, chemicals including H_2SO_4 (98%), tetrabutylammonium tetrafluoroborate (TBABF4, nBu_4NBF_4) (99%), acetonitrile (CH_3CN, 99.9%) and Nafion solution (5% weight in a mixture of lower aliphatic alcohols) were purchased from Sigma-Aldrich. $CyPH_2$ (10% in hexane) was purchased from Strem Chemicals. UP-NC7000WT multi-walled carbon nanotubes (MWNTs) were obtained from Nanocyl (purity 90% in carbon) and used as received, without further purification. Pt/C (46 wt% Pt/Vulcan XC72, Ref. TEC10V50) was purchased from Tanaka Kikinzoku Kogyo Co., Japan. GDL without MPL was purchased from Paxitech.

a. Electrochemistry

Electrochemical measurements in half-cell setup were performed as follows: in a thermostated glass electrochemical cell filled with 0.5 M H_2SO_4 in H_2O as a protic electrolyte were introduced a reference electrode (Hg_2SO_4/Hg, E = 0.694 V vs. SHE, Bio-Logic, chosen for potential stability in the presence of SO_4^{2-} ions), a counter electrode (99.99% Pt wire, Alfa Aesar) and a working electrode (custom built, see 1.b. "Micro half-cell"). Electrochemical analysis was performed on a Bio-Logic SP-300 potentiostat and data was processed in Origin 8.5. The setup was kept at 25°C and the electrolyte was degassed with Ar for an hour prior to data collection.

b. Synthesis of DuBois ligands and complexes

$P^{Cy}_2N^{PhCH_2CH_2COOH}_2$

This ligand and the corresponding activated ester ligand and complex following a published procedure.[81] To a suspension of paraformaldehyde (408 mg, 13.6 mmol) in degassed, dry ethanol (60 mL) cyclohexylphosphine (0.88 mL, 6.68 mmol) was added drop-wise. The suspension was heated at 78°C overnight under argon, after which 3-(4-aminophenyl)propionic acid (1.1 g, 6.65 mmol) was added, and the solution stirred at 78°C for an additional night. After cooling in the freezer at –18°C for several hours, the voluminous white precipitate was filtered with cannula and washed several times with ethanol. The precipitate was then recrystallized from DMF and water, filtered and dried to give 1.63 g of a white powder (2.67 mmol, 80%) ^{1}H NMR (DMSO-d_6): δ 11.97 (s, 2H, COOH), 6.95 (d, ^2J = 7.4 Hz, 4 H, NC_6H_4), 6.46 (d, ^2J = 7.6 Hz, 4 H, NC_6H_4), 4.13 (d, ^2J = 13.7 Hz, 4 H, PCH_2N), 3.89 (d, ^2J = 13.3 Hz, 4 H, PCH_2N), 3.31 (s, 8 H, CH_2CH_2COO), 1.07 – 2.90 (m, 22 H, C_6H_{11}); ^{31}P NMR (DMSO-d_6): δ –42.22.

$P^{Cy}{}_2N^{PhCH_2CH_2COOPht}{}_2$

To a solution of $P^{Cy}{}_2N^{PhCH_2CH_2COOH}{}_2$ (459 mg, 0.75 mmol) in 15 mL DMF was added *N*-hydroxyphthalimide (489 mg, 3 mmol) and EDC.HCl (577 mg, 3 mmol) and the mixture stirred overnight. The yellow suspension was added drop-wise to rapidly stirred water to precipitate the product, which was collected by filtration and recrystallized from chloroform and diethyl ether, then washed copiously with water, ethanol and ether to give 595 mg of a light yellow product (0.66 mmol, 88%). ^{1}H NMR ($CDCl_3$): δ 7.81 – 7.91 (m, 8 H, pht), 7.08 (d, ^2J = 8 Hz, 4 H, NC_6H_4), 6.66 (d, ^2J = 8 Hz, 4 H, NC_6H_4), 4.31 (t, ^3J = 13.5 Hz, 4 H, PCH_2N), 3.57 (d, ^2J = 15 Hz, 4 H, PCH_2N), 2.93 (m, 8 H, CH_2CH_2COO), 1.35 – 1.99 (m, 22 H, C_6H_{11}); ^{31}P NMR ($CDCl_3$): δ –39.64.

CyEster

In an argon-purged Schlenck flask, 130 mg $P^{Cy}{}_2N^{PhCH_2CH_2COOPht}{}_2$ (0.144 mmol) and 26.7 mg $[Ni(MeCN)_6](BF_4)_2$ (0.057 mmol) were dissolved in ~5 mL dry, degassed acetonitrile and stirred overnight at room temperature under argon. The purple solution was filtered and the solvent removed to give 102 mg of $[Ni(P^{Cy}{}_2N^{PhCH_2CH_2COOPht}{}_2)_2](BF_4)_2$ (**CyEster**) as a purple powder (0.05 mmol, 88%). ^{1}H NMR (CD_3CN): δ 7.88 (s, 16 H, pht), 7.27 (d, ^2J = 8.3 Hz, 8 H, NC_6H_4), 7.04 (d, ^2J = 8.3 Hz, 8 H, NC_6H_4), 4.09 (d, ^2J = 14.1 Hz, 4 H, PCH_2N), 3.83 (d, ^2J = 14.2 Hz, 4 H, PCH_2N), 3.75 (d, ^2J = 14.5 Hz, 4 H, PCH_2N), 3.56 (d, 2J = 13.9 Hz, 4 H, PCH_2N), 3.02 (s, 16 H, CH_2CH_2COO), 1.39 – 2.22 (m, 44 H, C_6H_{11}); ^{31}P NMR (CD_3CN): δ 6.34. MS (ESI$^+$): *m*/*z* 929.7 $[M–2BF_4^-]^{2+}$. Elemental analysis (%) calculated for $C_{100}H_{108}B_2F_8N_8NiO_{16}P_4$: C, 59.05; H, 5.35; N, 5.51; found: C, 56.95; H, 5.33; N, 5.52.

$P^{Cy}{}_2N^{CH_2Pyrene}{}_2$

$P^{Cy}{}_2N^{CH_2Pyrene}{}_2$ was synthesized according to a previously reported.[72] Briefly, 1-Pyrenemethylamine hydrochloride was suspended in degassed water, and an excess of NaOH (dissolved in water) was added. DCM was added and the biphasic mixture stirred rapidly for 30 minutes, then separated. The aqueous layer was extracted with DCM, and the combined organic phases dried with Na_2SO_4 and evaporated. Separately, paraformaldehyde (51.2 mg, 1.7 mmol) and cyclohexylphosphine (0.11 mL, 0.83 mmol) were reacted at 78°C overnight. 1-Pyrenemethylamine (200 mg, 0.86 mmol) in approx. 2 mL DCM was added, and the solution heated overnight. The resulting cream precipitate was filtered and rinsed, giving 200 mg (0.267 mmol, 65%). ^{31}P NMR (CD_3COOD/CD_3Cl): δ −54.1 ppm.

CyPy

$[Ni(P^{Cy}_2N^{CH_2Pyrene}_2)_2](BF_4)_2$ (**CyPy**) was synthesized according to a previously reported procedure.[72] Briefly, $P^{Cy}_2N^{CH_2Pyrene}_2$ (140 mg, 0.187 mmol) and $[Ni(CH_3CN)_6](BF_4)_2$ (60 mg, 0.125 mmol) were mixed in 5 mL degassed MeCN and stirred for three hours, resulting in a red solution with dark purple precipitate. The solution was filtered and the purple precipitate sonicated in additional MeCN, then also filtered. The combined filtrates were concentrated to a fifth of the original volume and the pink product precipitated with ether, resulting in 58 mg of product (0.034 mmol, 27%). ^{31}P NMR (CD_3CN): δ 3.4 ppm.

$P^{Cy}_2N^{Arginine}_2$

$P^{Cy}_2N^{Arginine}_2$ was prepared following a previously published protocol[82]. Briefly, bis(hydroxymethyl)cyclohexylphosphine (200 mg, 1.13 mmol) and arginine (196 mg, 1.13 mmol) were dissolved in 10 mL of ethanol in a Schlenk flask and heated at 80 °C overnight. The resulting white precipitate was filtered, washed with ethanol and acetonitrile and vacuum dried to obtain white solid powder. Yield: 250 mg (0.40 mmole) (70%). ^{31}P NMR (CD_3OH): δ −27.6 ppm, and −35.3 ppm, broad.

CyArg

$[Ni(P^{Cy}_2N^{Arginine}_2)_2](BF_4)_2$ (**CyArg**) was synthesised as previously described[82]. Briefly, $[Ni(CH_3CN)_6](BF_4)_2$ (30.0 mg, 0.063 mmol) was dissolved in 3 mL of methanol, then added dropwise to a solution of $P^{Cy}_2N^{Arginine}_2$ (80 mg, 0.1266 mmol) in 10 mL of methanol and stirred overnight. The red solution was evaporated under reduced pressure and a red/pink powder was obtained. It was filtered, rinsed with Et_2O and vacuum dried. Yield: 54 mg (0.036 mmole) (58%). 1H NMR (CD_3OD): δ 1.1-2.2 (H-cy, Arg-H δ, and Arg-H ε, 30H, m); 3.2-3.6 ppm (-PCH_2N, Arg-H α, and Arg-H γ, 14H, m). 31P-[1H] NMR (CD_3OD): 14.3 ppm, broad.

c. GDL/MWNT/**CyPy** electrode

Grafting of CyPy

This grafting method was also described in our previous work.[72] No prior modification of the MWNTs was required, and they were simply dispersed in EtOH by sonication (6 $mg.mL^{-1}$) either without or with Nafion (100 wt% with respect to the MWNT). This MWNT suspension was mixed in a 3:1 ratio with a 1 mM solution of **CyPy** in DCM and 40 µL of this mixture were drop-casted onto a 0.125 cm² circular area of a GDL and air-dried.

d. GDL/MWNT-NH_2/**CyEster** electrode

Diazonium salt

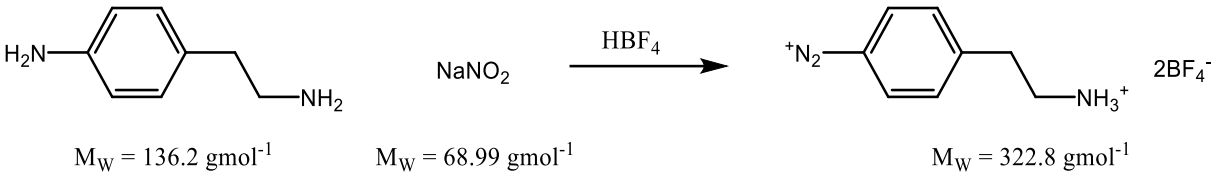

M_W = 136.2 $gmol^{-1}$ M_W = 68.99 $gmol^{-1}$ M_W = 322.8 $gmol^{-1}$

4-aminoethylbenzenediazonium was synthesized according to a published procedure[104]. Briefly, 4-(2-aminoethyl)aniline (Sigma, 408.5 mg, 3 mmol) was dissolved in approx. 20 mL of 25% aqueous HBF_4 solution (made by diluting 10 mL of commercial 50% HBF_4 solution (Sigma) in the same volume of water), and cooled in an ice bath. Sodium nitrite (Sigma, 221 mg, 3.2 mmol) in approx. 1 mL of water was added dropwise, and the solution was stirred for 40 minutes, after which the resulting white precipitate was collected on filter paper, air dried, then washed with diethyl ether and dried under vacuum. The yield was 690 mg (2.13 mmol, 71%) as sharp orange needle-shaped crystals. ^{1}H NMR (CD_3CN; 300 MHz): δ (ppm) 8.47 (d, 2H), 7.82 (d, 2H), 6.35 (t, 3H), 3.26 (m, 4H).

MWNT-NH_2

As described in our early work for similar complexes bearing activated ester function,[76,81] MWNTs (3 mg) are dispersed by sonication in 25 mL abs. EtOH, either without or with Nafion (100 wt% with respect to the MWNT), and filtered onto a 5 cm² circular piece of GDL. 4-aminoethyl)benzene diazonium tetrafluoroborate (25 mg in 50 mL degassed MeCN / 0.1 M $TBABF_4$) was electrochemically reduced onto the MWNT layer through cyclic voltammetry by recording 2 cycles at 20 $mV.s^{-1}$ between 0.5 V and - 0.8 V vs Ag/AgCl, yielding a GDL/MWNT-NH_2 electrode.

Alternative strategies for modification of the MWNTs were employed to ensure that the behaviour of the MWNT-NH_2/**CyEster** system did not arise from the electrodeposition of the diazonium salt. Following the protocol for the synthesis of MWNT-COOH, replacing the 6-amino-2-naphtoic acid by 4-(2-aminoethyl)aniline yielded MWNT-NH_2. Although the overall areal current densities were lower with this functionalization mode, no qualitative difference was observed when compared to the MWNT-NH_2 made by electrodeposition of the diazonium salt.

Grafting of CyEster

The GDL/MWNT-NH_2 electrode was then soaked in a 1 mM solution of **CyEster** in DMF in the presence of 10 eq. of 2,6-lutidine overnight, then rinsed with DMF, MeCN and air-dried.

e. GDL/MWNT-COOH/**CyArg** electrode

MWNT-COOH

Adapting from an existing procedure,[80] MWNTs (50 mg) are sonicated in 150 mL of argon-degassed DMF for 45 minutes. 1.5 g of 6-amino-2-naphtoic acid and 1.1 mL of isoamyl nitrite are added, to trigger the in-situ formation of 2-naphthoic acid 6-diazonium and its subsequent reduction onto the MWNTs. The reaction vessel is purged with argon, closed then heated under stirring at 80°C for 12 hours. After cooling, the MWNTs are filtered on a 0.45 µm Teflon filter, sonicated overnight in 150 mL of DMF then filtered again. They are rinsed thoroughly with hot DMF and EtOH and dried under vacuum to yield around 50 mg of MWNT-COOH.

Catalytic ink

6 mg of MWNT-COOH are dispersed by sonication in 2 mL of abs. EtOH, either without or with Nafion (100 wt% with respect to the MWNT). This suspension is mixed in a 3:1 ratio with a 3 $mg.mL^{-1}$ solution of **CyArg** in pH 6, aqueous, 0.1 M MES:HEPES (1:1) buffer. 40 µL of this suspension are then drop-casted directly onto a 0.125 cm^2 circular area of GDL and air-dried.

f. ULL-Pt modification of nanotubes

The functionalization was done by the team of Dr Frédéric Maillard following a published procedure from their group.[103] Briefly, the deposition of the Pt nanoparticles onto the various carbon supports was performed as follows: (i) a given amount of Pt salt (H_2PtCl_6-xH_2O, 99.9% metal basis, Alfa Aesar) was first dissolved in a 2:1 ethylene glycol (Rotipuran > 99.9 %, Roth):deionized water (18.2 MΩ) solution (typically 88 mg of Pt salt in 100 mL of solution). Then, (ii) the solution was rendered alkaline up to pH = 12.5 and vigorously stirred under argon atmosphere during t = 1 h, (iii) prior to the temperature was increased at T = 393 K and maintained during t = 3 h. Meanwhile, the carbon support was dispersed in a 1:1 ethylene glycol:deionized water solution, aiming a theoretical loading of Pt onto the carbon support of 1 wt.%. (iv) The solution containing the Pt colloidal solution and the dispersed carbon support were mixed and the pH of the solution was decreased down to pH = 2.5 to allow the

nanoparticles deposition onto the carbon support. (v) After t = 22 h, the solution was filtered, washed and dried for t = 45 min at T = 383 K.

The obtained dry powder was then dispersed in EtOH at 3 mg/mL, in the eventual presence of Nafion ionomer (100 wt%) and deposited onto a GDL in order to obtain a final surface loading of 7 µg/cm² of Pt.

Chapter II – Catalytic ink formulation and deposition

Apart from the intrinsic activity markers of a catalyst described in the general introduction, several factors impact its catalytic ability. When we discuss optimization of catalytic materials in this chapter, we are discussing the optimization of the catalytic environment for a given catalyst. In electrocatalytic systems, an ideal environment will be one that places each catalytic site at the boundary of three networks which provide transport for substrate(s), product(s) and electrons. In the case of fuel cell anodes, this means the triple point of a gas transport network, proton channels and a conductive material. While electronic conductivity is rarely a problem when electrodes are elaborated with carbon materials,[105,106] the "sweet spot" in this triple boundary is very tricky to achieve,[97,107] as H_2 gas is very hydrophobic, and protons are transported only in aqueous channels in which H_2 diffuses very sluggishly.[90,91]

Diffusion-limited catalysis becomes a problem at high current densities, or when the thickness of electrodes is increased.[18] Thicker electrodes with good diffusion properties for H_2 and H^+ could be economically desirable, as they enable higher catalytic loading, and therefore higher power outputs, for a given amount of stacks.[108] Furthermore, non PGM catalysts are, as of now, notoriously less catalytically active than Pt, and hence require thicker electrodes to reach higher catalytic loading and similar current densities.

Rational formulation of catalytic inks through the use of additives, tuning of the $\frac{ionomer}{total\ mass}$ ratio, solvent choice, dispersion methods and deposition strategies (such as spray, filtration, drop-casting, doctor-blading…) can impact to drastic extents the nano-structuration of electrodes. Classically, bio-inspired catalysts for H_2 oxidation have been benchmarked in the conditions optimized for Pt catalysts.[72] However, although this is a practical way to proceed, it might not be the ideal one as the requirements of molecular catalysis, which after all generally takes place in a somewhat solvated or homogeneous phase, are notoriously different from those of heterogeneous nanoparticular catalysis, be it in terms of local environment, climatic conditions or electrode structure. Maybe, in order to get the most out of alternative catalysts, we ought to try and place them in better environments. In this chapter, we are interested in selecting and tuning some easily modifiable and relevant parameters and rationalize their effect on molecular catalysis, then pool this gathered understanding to build a somewhat optimized electrode before proceeding to its integration (described in Chapter IV). In addition to optimization, we are also interested in making electrodes in the most reproducible way in order to be able to predict the

power outputs we can expect from a whole fuel cell. First, we look at different carbon additives to the MWNTs, then at the role of ionomer in the electrode and highlight an unexpectedly beneficial interaction between fullerene and Nafion. Finally, we discuss the assembly of a Nafion membrane onto our anodes, the next step towards integration.

1. Catalytic ink formulation

a. Previous work in the group

In our group, work had already been done, in particular by Tran N. Huan using **CyEster**,[76] on nano-structuration to make more porous electrodes. This blend of microfibers and MWNTs was shown to improve both catalytic loading and substrate diffusion within thicker electrodes (10 to 50 µm). For instance, the difference in scale between microfibers and MWNTs is very large (see Figure 1) and the MWNTs can wrap around the fibres, yielding a thick and mesoporous mat of carbon material support.

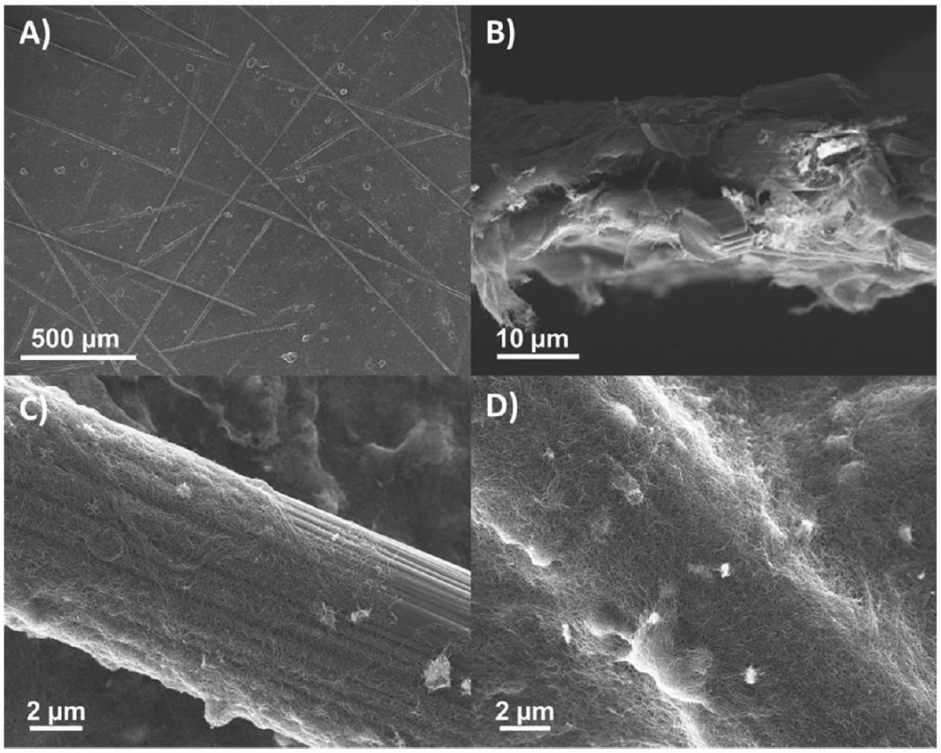

Figure 1. SEM images of GDL electrode coated with 0.267 mg/cm² MWNTs and 0.033 mg/cm² carbon microfibers. (A) Top view; (B) cross-section view; (C) and (D) magnification showing single carbon microfibers coated with MWNTs. Reproduced from ref [76]

This approach was combined with new strategies to deposit the carbon mixture onto a GDL, as this deposition step was determined crucial for both catalytic activity and reproducibility of results. Briefly, instead of vacuum-filtering the carbon mixture onto the GDL, capillary

evaporation yielded thicker, more porous carbon mats as well as increased catalyst loading. Following this line of investigation of the possible nano-structuration of the ink to improve performance, we benchmarked four different carbon additives to some catalytic inks: carbon micro- and nano-fibres, graphene platelets and C_{60} fullerene.

b. Effect of different carbon additives on catalytic activity

As mentioned in the general introduction, assessment of the possibility of technological integration for our catalysts was one of the goals of this work. Therefore, through a collaboration with the team of Pierre-André Jacques at CEA Liten, we investigated ink formulation first on the catalyst that was the easiest to implement on larger scales, **CyPy**, as it could be grafted onto pristine nanotubes by merely mixing them during the ink preparation process, avoiding the need for an immobilization step. Several carbon materials, carbon micro-fibres (0.7 mm x 6 mm, Alfa Aesar), carbon nano-fibres (100 nm × 20-200 µm, Aldrich), graphene platelets (N006-010-P, Angstron) and fullerene (C_{60}, Sigma), were used as additives with different expected effects within the catalytic ink. In each case, 10% of the MWNT were replaced by the additive. Their effect on catalytic behaviour is showed in Figure 2.

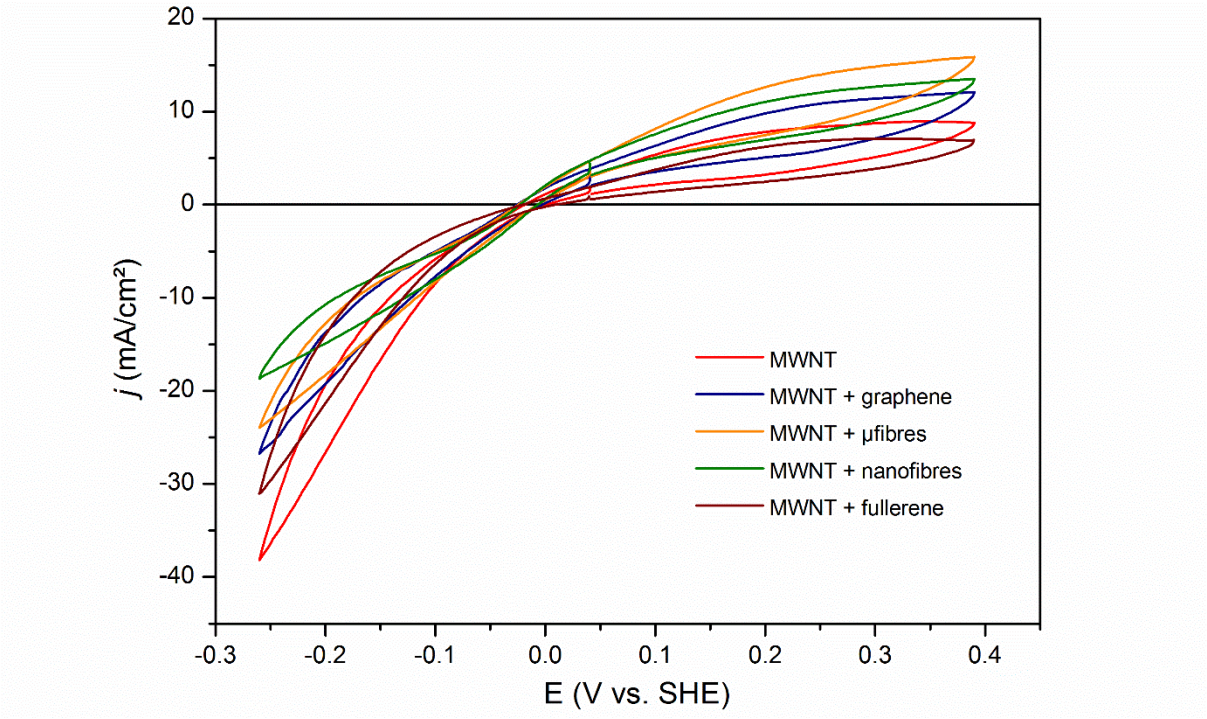

*Figure 2. Effect of four carbon additives on a MWNT/**CyPy** electrode without ionomer. Half-cell setup, S = 0.063 cm², electrolyte is H_2SO_4 0.5 M in H_2O, pH 0.3, 298K and P_{H2} = 1 atm.*

Three main strategies were tested to improve the performances: 1) nano-structuration, 2) modifying the grafting sites and increasing their density and 3) enhancing substrate diffusion.

i. Nano-structuration of the electrode

Carbon microfibers were added to improve porosity, thickness and therefore site loading (SL) as a way of assessing whether this strategy, employed originally for the MWNT-NH_2/**CyEster** system, could be employed for the MWNT/**CyPy** electrodes. Nano-fibres were added with the same goal as microfibers, but with a material that would be able to undergo spray deposition of the catalytic ink, as bulky micro-fibres could clog the nozzles of spray guns. These were merely attempts at changing the structure of the thickness of the electrode by adding carbon materials of strikingly different scales from that of the MWNT, in order to induce a long-range organization of the material support within the electrode. Carbon micro- and nano-fibres are notoriously amorphous and unreactive, which meant that no direct effects on catalytic cycles were expected.

In line with what was observed for the GDL/MWNT-NH_2/**CyEster** systems, Figure 2 shows an increase in current for hydrogen oxidation with the addition of micro-fibres. The same behaviour is observed for nano-fibres, and attributed to the same phenomenon. Decrease in H^+ reduction currents is attributed to the increase in thickness of those very hydrophobic electrodes, which in the absence of Nafion entails poor proton relay throughout the thickness of the electrode.[93,94]

ii. Modification of grafting sites

Graphene, on the other hand, is not as chemically innocent as the afore-mentioned fibres. It is always somewhat oxidized and presents electron-rich graphitic regions. Graphene oxide is a weak oxidizer and can be used in a variety of reactions, however it is not enough of an oxidizer to activate the H_2 molecule. It was added to our inks in order to increase the amount of π-stacking sites for grafting the **CyPy** complex, or to stabilize such a bond by "sandwiching" the pyrene moiety between the MWNT and graphene.

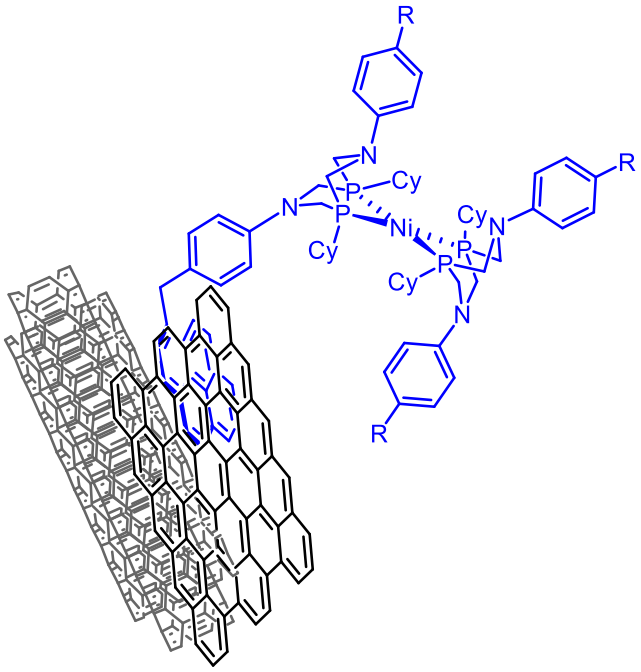

*Figure 3. Possible "sandwich" interaction between graphene platelets, MWNT and **CyPy**. R = CH_2-Pyrene.*

Some improvement of the current densities for H_2 oxidation was observed in the presence of graphene (blue line, Figure 2) but due to the poor understanding of the nature of the graphene that was used and of the possible interaction, we did not pursue investigation further as we wanted to work on well-defined systems in order to be able to rationalize the different aspects of catalysis.

iii. Enhancing diffusion of H_2

Fullerene was originally added with the same goal as graphene, in order to modify or increase the amount of grafting sites. However, as shown in Figure 2, the addition of fullerene shows a decrease in currents for both hydrogen oxidation and production. We assumed that this decrease of activity was due to the fact that fullerene motifs could stack around the nanotubes, decreasing the amount of available grafting sites. However, in line with reports on the affinity of fullerene aggregates for H_2 adsorption and their use for storage of H_2, it was also thought that fullerene could play the very different role of enhancing diffusion of H_2 to the catalyst. We attribute its detrimental effect on catalysis to the fact that H_2 diffusion in these very hydrophobic systems was maybe not limiting as much as H^+ diffusion, which requires water. Hence, we tried adding Nafion to enhance proton relay within the electrode, to inks both with and without fullerene.

iv. Effect of Nafion, synergy with fullerene

In Figure 4, we see the effect of Nafion ionomer, added to the catalytic ink a 1 : 1 mass ratio compared to the MWNTs, with and without fullerene as an additive. In addition to the catalyst, the inks contain either only MWNT (black), or added Nafion (orange), fullerene (purple) or both (red). We can see that the addition of Nafion to a simple MWNT/**CyPy** ink causes a marked decrease in both oxidation and reduction currents. This effect is also observed in the case of MWNT with added micro- or nano-fibres or graphene. This is in line with the results of Chapter I, in which we attributed this drop in activity to a displacement of the bond between the catalyst and MWNTs by the hydrophobic parts of Nafion. The fact that the addition of Nafion is very detrimental to H^+ reduction activity in the absence of fullerene can be explained by the same displacement of the MWNT/catalyst bond, or a poor evacuation of H_2, the product of this reaction, as is seen in catalytic kinetics of several hydrogenase enzymes.[35,109,110] However, the addition of fullerene to the ink entirely reverses the effect of Nafion, which becomes indeed beneficial to both oxidation and reduction currents. This effect was unexpected, yet understandable: as mentioned in the previous paragraph, fullerene is hydrophobic and presents high affinity for H_2 gas.

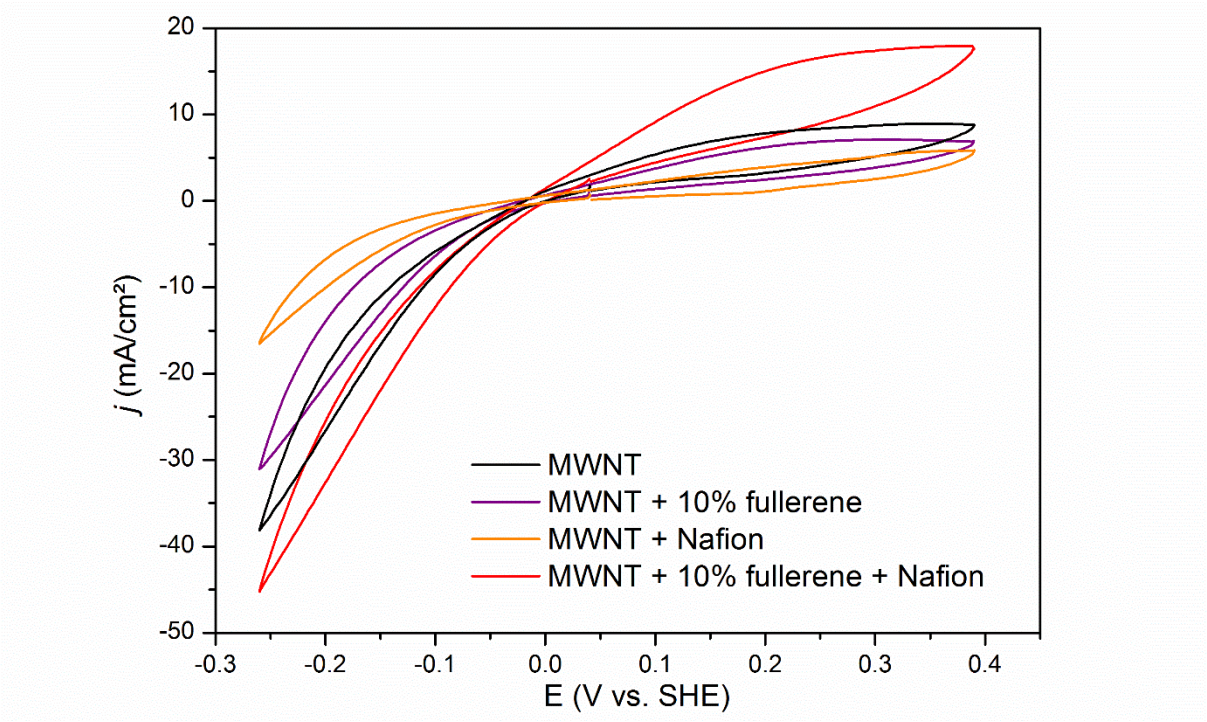

*Figure 4. Effect of Nafion ionomer on MWNT/**CyPy** electrodes with and without fullerene.* $\frac{m_{fullerene}}{m_{MWNT+fullerene}}$ *= 10 % and* $\frac{m_{Nafion}}{m_{MWNT}}$ *= 100 %. Half-cell setup, S = 0.063 cm², electrolyte is* H_2SO_4 *0.5 M in* H_2O*, pH 0.3, 298K and* P_{H2} *= 1 atm.*

Our theory is that fullerene percolates the electrode throughout its thickness as well as the hydrophobic regions of Nafion, permitting H_2 diffusion through what was previously an almost entirely gas-tight domain. Concurrently, the presence of fullerene could create a different organization of the hydrophobic parts of Nafion around MWNTs, limiting displacement of the catalytic sites. Advanced characterization of fullerene and Nafion containing electrodes is the subject of Chapter III, in which we put these theories to the test of various techniques.

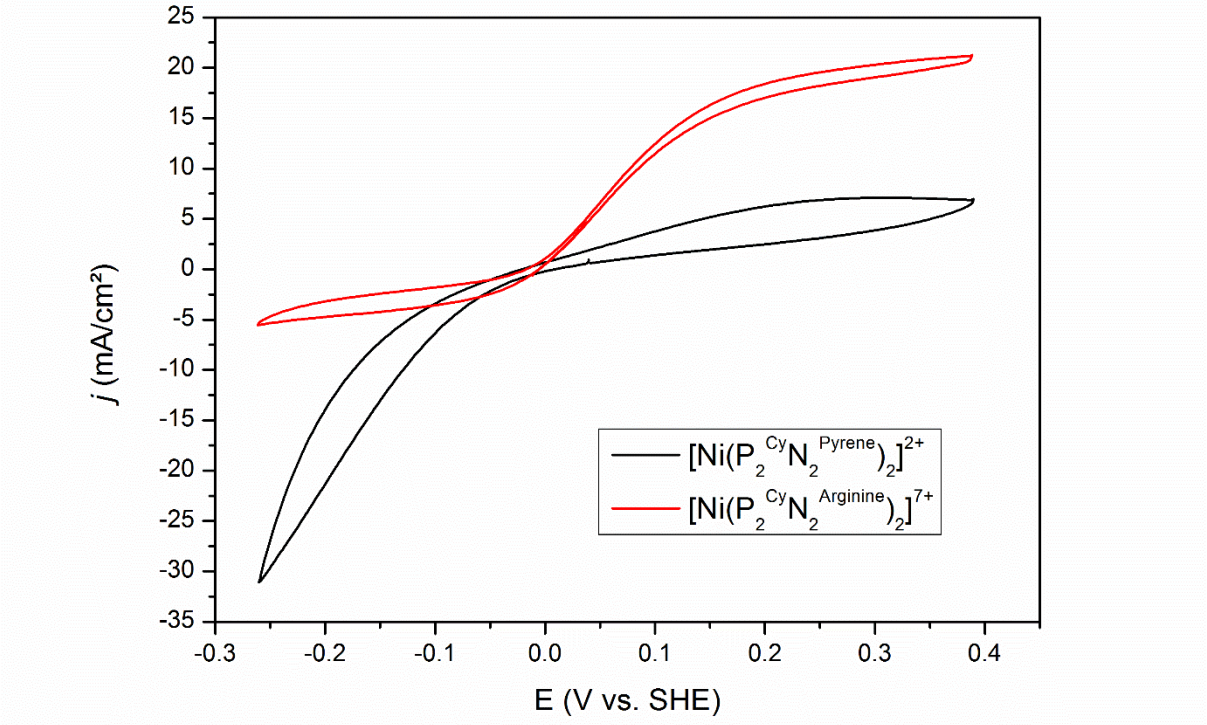

Figure 5. Comparison of the catalytic biases of $[Ni(P_2^{Cy}N_2^{Pyrene})_2]^{2+}$ on MWNT and $[Ni(P_2^{Cy}N_2^{Arginine})_2]^{7+}$ on MWNT-COOH. Half-cell setup, S = 0.063 cm², electrolyte is H_2SO_4 0.5 M in H_2O, pH 0.3, 298K and P_{H2} = 1 atm.

All these experiments on carbon formulation were done early during this project, with **CyPy** as a catalyst. However, **CyArg** shows the most promise for integration because of its strong bias towards H_2 oxidation (See Figure 5) and the unexpectedly good behaviour of the MWNT-COOH/**CyArg** electrodes in the presence of Nafion ionomer (see Chapter I) which we explain by the better stability towards Nafion of the hydrophilic interaction between MWNT-COOH and **CyArg**. Hence, **CyArg** was chosen for the optimisation of ionomer ratio and subsequent integration in fuel cells. Before proceeding with this catalyst, we took a first look at whether the effects of fullerene were the same as for **CyPy**.

c. Ionomer within the ink, and fullerene as a diffusion enhancing additive

Here we first assess some limitations of **CyArg** electrodes, then verify that the effect of fullerene in the presence of Nafion observed for **CyPy** electrodes exists for **CyArg**. Then, we research an optimal ink composition in both fullerene and ionomer.

i. Diffusion-limited catalysis at high overpotentials

The CVs of electrodes containing nothing else than the MWNT-COOH and **CyArg** have the same aspect as the black line of Figure 6, in which the catalytic current for H_2 oxidation reaches a plateau above about 150 mV of overpotential, a trend that betrays diffusion-limited catalysis, in particular limitations from diffusion in liquids.[16] This plateau appears for Nafion-free electrodes. It is attributed to proton diffusion limitation, and the impossibility for the catalyst to rid itself from H^+ fast enough, meaning that intrinsic TOF of **CyArg** is not limiting at high overpotentials. The almost total disappearance of this plateau shape in the presence of Nafion (compare the black and blue lines in Figure 6) leads us to think that diffusion of H^+ is not limiting anymore in the case of Nafion-containing electrodes.

The H^+ reduction currents for electrodes with and without Nafion (black and blue lines) are very similar, which is to say not limited by proton diffusion, which we explain by the fact that the current densities for proton reduction are much lower overall than the ones for H_2 oxidation, hence not limited by mass transport. These identical currents also mean that the amount of electronically connected catalysts for both systems does not change, which is confirmed by SL determination through CVs in aprotic, degassed solvent. This method gives SL at about 4 nmol/cm² for all the electrodes presented in Figure 6. However, initial current (in the 0 – 50 mV overpotential region) for H_2 oxidation is much weaker in the presence of Nafion. This, we attribute to a complete lack of diffusion of H_2 to some catalytic sites, rendering them unavailable for H_2 oxidation catalysis and hence "invisible" in catalytic assessments. Proton diffusion limitation is visible in CVs in the form of a plateau because of its sluggish kinetics (diffusion coefficient of the order of 7×10^{-5} cm²/s in water),[89] whereas H_2 gas diffusion in carbon electrodes, while difficulty characterized, is thought to be overall much faster.[111] If a site is reached by H_2, we do not expect H_2 mass transport to be a limiting factor.

On the other hand, while the addition of fullerene to the electrode does not make the diffusion plateau disappear (compare black and orange lines, Figure 6), it does increase drastically the initial slope of the CV in the oxidative region. In line with previous arguments, we attribute this increase to the creation of H_2 diffusion pathways to catalytic sites which otherwise would not

see any H_2. The plateau remains, displaying the same H^+ diffusion limitation as before, but sits at higher current densities as more sites are turning over. When combining fullerene and Nafion, we obtain the best of both worlds with a strong initial slope and disappearing of the diffusion plateau. This effect was attributed to a percolation of gas-diffusing fullerene aggregates throughout the thickness of the electrode, as well as through the hydrophobic domains of Nafion. This renders them permeable to H_2 gas and allows diffusion of both H_2 to more catalytic sites. These qualitative differences between electrodes are more thoroughly characterized in Chapter III.

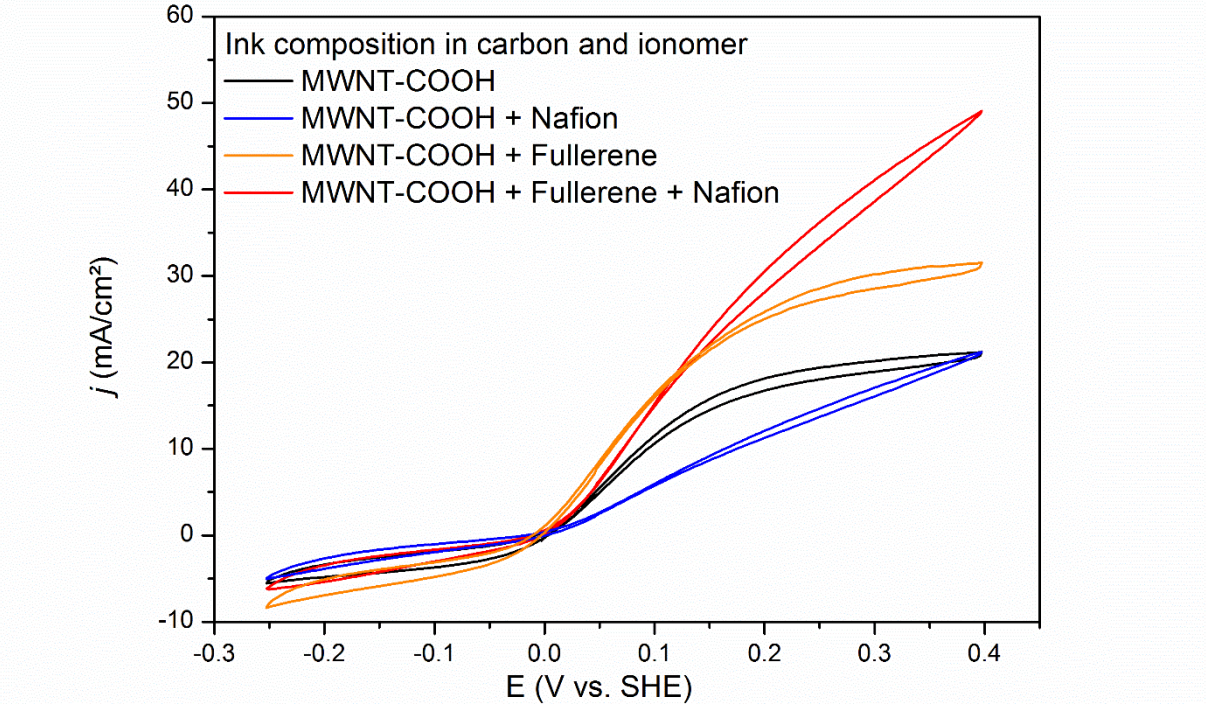

*Figure 6. CVs illustrating the diffusion-limiting effects at high overpotentials in MWNT-COOH/**CyArg** electrodes in the presence or not of Nafion ionomer and fullerene. Half-cell setup, S = 0.063 cm², electrolyte is H_2SO_4 0.5 M in H_2O, pH 0.3, 298K and P_{H2} = 1 atm.*

The similar H^+ reduction currents and SL values for the black and red curves prove that the amount of electronically connected catalysts is the same. The combination of proper H^+ and H_2 diffusion networks has provided catalysts with a high-performing diffusive environment that connects more sites and enables them to reach their maximum possible TOF regardless of applied overpotentials.

ii. Nafion to carbon support material ratio

An optimal ratio of Nafion to carbon support material $\frac{m_{Nafion}}{m_{Carbon}}$ had to be chosen, as too little Nafion would entail poor proton diffusion and too much could hinder gas diffusion. Activity for H_2 oxidation of MWNT-COOH/**CyArg** electrodes was measured at different values of this ratio, between 0 and 200 wt% (Figure 7, black) yielding an optimum at about 25 wt%. This study was also led for MWNT-COOH/**CyArg** electrodes containing 10 wt% of fullerene compared to the total carbon weight, (Figure 7, grey) in line with the effects observed for **CyPy** (Figure 4). In the case of these electrodes, the optimal ratio of Nafion is displaced at around 100 wt% and the maximum current at 350 mV overpotential reaches over 50 mA/cm² at RT.

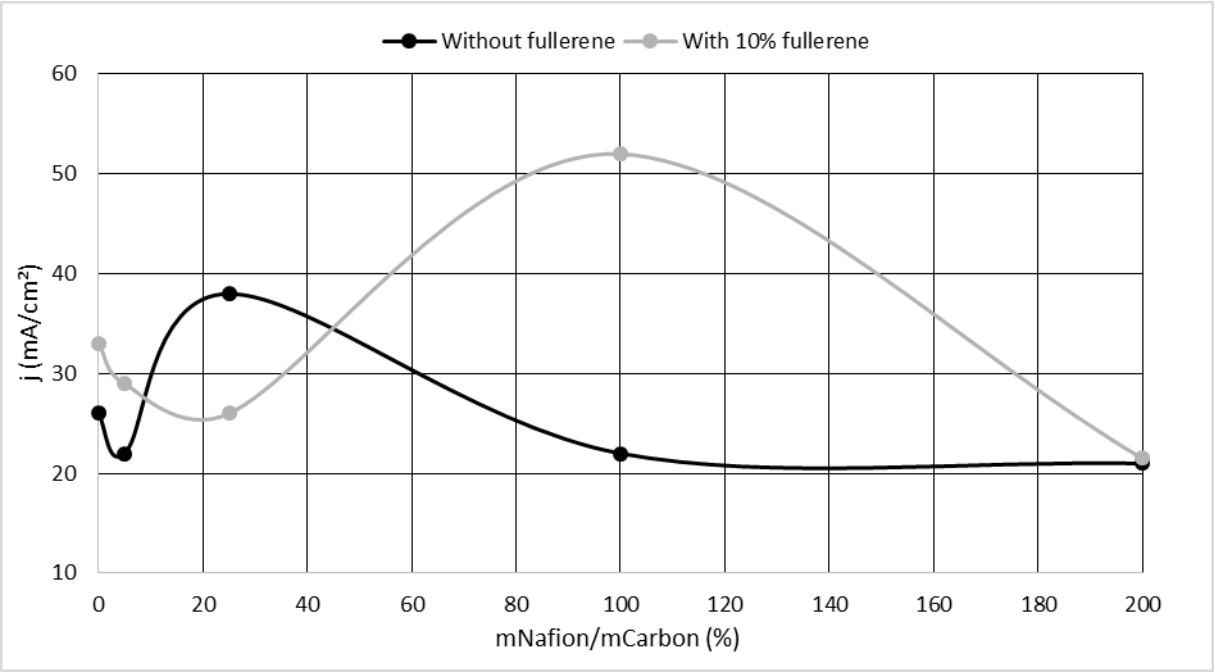

*Figure 7. Current densities of a MWNT-COOH/**CyArg** electrode with (grey) and without (black) fullerene (10 wt%) as a function of Nafion content. Half-cell setup, S = 0.063 cm², electrolyte is H_2SO_4 0.5 M in H_2O, pH 0.3, 298K and P_{H2} = 1 atm.*

The fact that this value is larger than the maximum observed for fullerene-free electrodes leads us to think that more catalytic sites are able to perform catalysis. The broader peak for fullerene-containing electrodes indicates an overall better tolerance to Nafion, and this synergy between fullerene and Nafion was of utmost interest given the necessity for the presence of Nafion ionomer within the electrode in the elaboration of PEMFCs.

iii. Fullerene to MWNT-COOH ratio

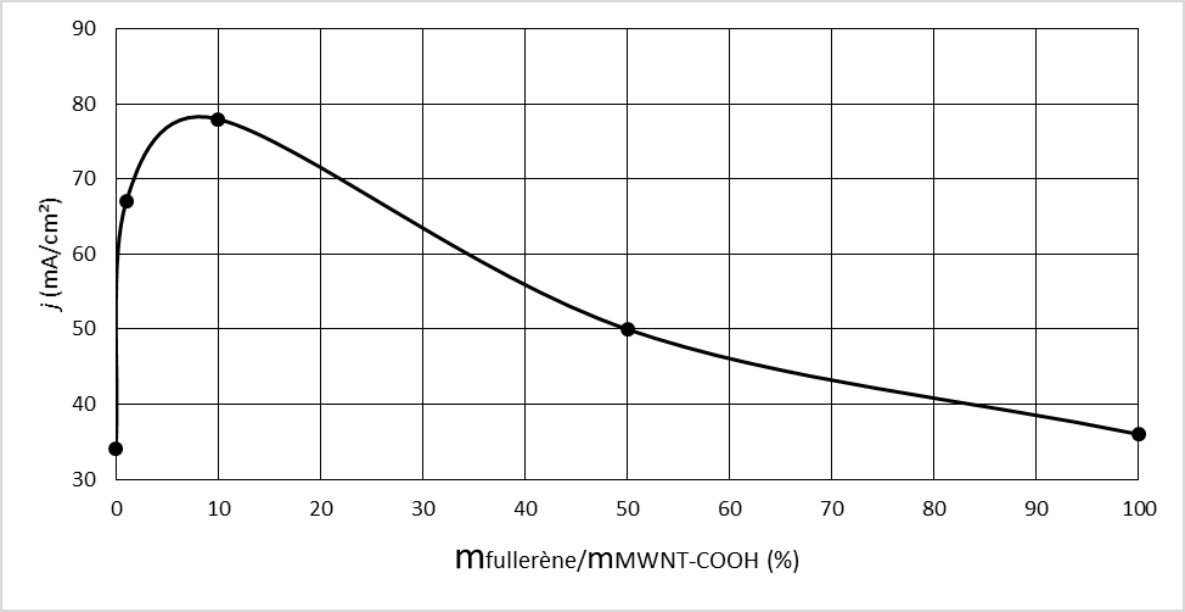

*Figure 8. GDL/MWNT-COOH/**CyArg** electrodes with 100 wt% Nafion. Current densities at 350 mV overpotential as a function of the fullerene to MWNT-COOH ratio. Half-cell setup, S = 0.063 cm², electrolyte is H_2SO_4 0.5 M in H_2O, pH 0.3, 298K and P_{H2} = 1 atm.*

Given the synergetic behaviour of fullerene and Nafion, we explored the ratio of fullerene to MWNT-COOH in order to find an ideal composition. Figure 8 shows the current densities of several GDL/MWNT-COOH/**CyArg** electrodes containing 100 wt% Nafion and different amounts of fullerene. Current densities were the best around 8 wt% fullerene and we used that ratio continuing onwards. This is however only a "local" optimization, as fullerene ratios haven't been tried for other amounts of Nafion and the overall shape of this optimisation 3D plot (in which *x* is amount of Nafion, *y* amount of fullerene and *z* current densities) is unknown.

d. Catalyst to support material ratio

One point of investigation was how much catalyst could be attached to a given amount of MWNT-COOH without losing electrode stability over time. Indeed, the MWNT-COOH are difficultly characterized in terms of amount of -COOH functions and it is hard to theoretically calculate their capacity to accommodate grafted catalysts, especially given how little is known about the amount of -COOH functions required to graft a **CyArg** complex. To study this effect, the ratio of **CyArg** to MWNT-COOH was increased, increasing current densities until a certain point when electrodes stopped displaying stable activity in chronoamperometry. Along with this optimization, the buffer concentration in the catalyst solution (See the experimental section of Chapter I) was lowered from 0.1 to 0.01 M in order to avoid the accumulation of salts on the electrode surface when drying the catalytic ink.

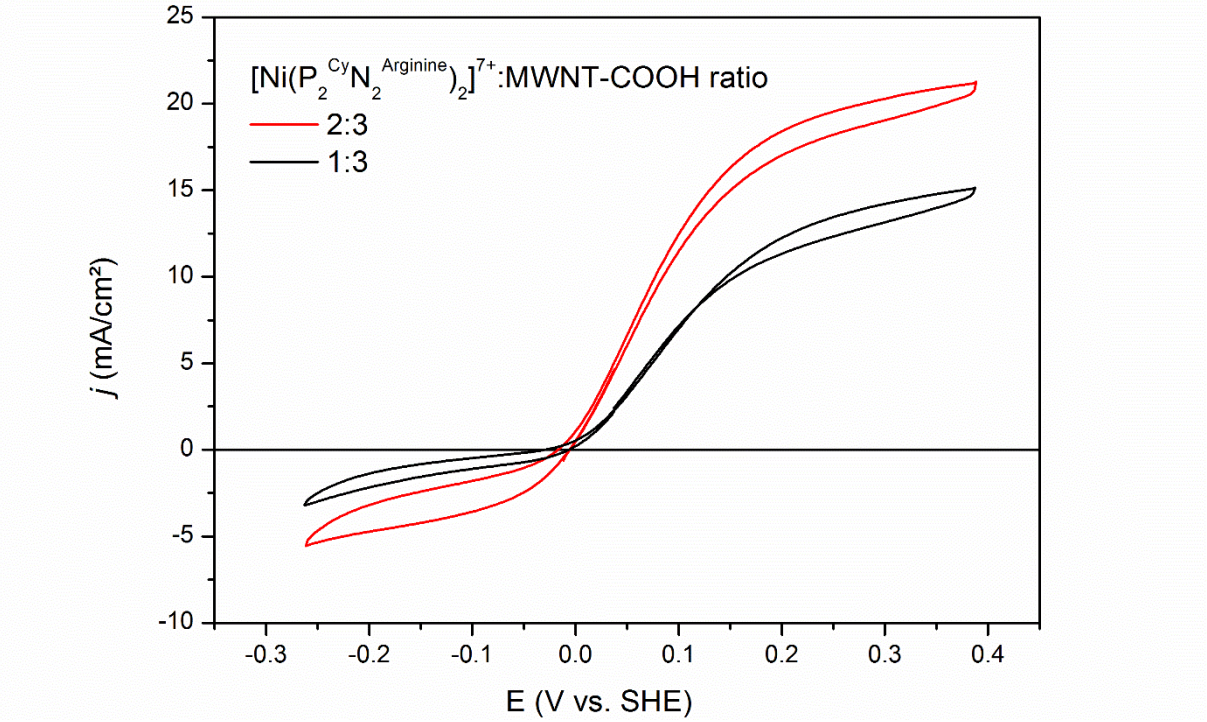

*Figure 9. Effect of **CyArg**:MWNT-COOH ratio on current densities of GDL/MWNT-COOH/**CyArg** electrodes. Half-cell setup, S = 0.063 cm², electrolyte is H_2SO_4 0.5 M in H_2O, pH 0.3, 298K and P_{H2} = 1 atm.*

We took advantage of the high solubility of **CyArg** in pH 6 buffer solution to increase the **CyArg** to MWNT-COOH ratio by dissolving more **CyArg** in the same amount of solution rather than add more solution of **CyArg** to the catalytic ink, which would have led to a difference in formulation and possibly to dilution issues. The original ink had a ratio of 1:3 **CyArg**:MWNT-COOH which we eventually increased to 2:3. Figure 9 shows the activity for those two ratios of **CyArg** to MWNT. Further addition of **CyArg** simply resulted in unstable catalytic activity that stabilized over time at the level of the catalytic currents observed for the 2:3 ratio. This was attributed to a washing off of the excess catalyst presented with too few anchoring functions, and the ratio we achieved was deemed satisfactory for our purposes.

e. Proton-exchange membrane

As the ultimate goal of this optimization part of this work was integration of the best anodes in a fuel cell, addition of a Nafion membrane had to be addressed. Early results with the first PGM-free fuel cell in our group[72] seemed to hint at the fact that the assembly of the MEA was more of a determining factor of performance than previously thought, especially given our group's limited knowledge of the more technological aspects of building a fuel cell. Hence, a study was led to troubleshoot the specificities of the interaction between our electrodes and Nafion membrane. In order to build a good proton relay between anode and cathode, the Nafion

membrane has to be well connected to the ionomer throughout the thickness of each electrode. This is done by ensuring the right pressure, time and temperature of MEA assembly as well as the presence in correct ratios of ionomer within the catalytic ink.[89,94,112,113] Ideally, the membrane should be pressed above the glass-transition temperature of Nafion (about 140°C)[89] but due to the molecular nature of our catalysts, this was out of the question as pressing at this temperature or above resulted in a total loss of catalytic signal. Hence, alternative pressing conditions were examined. Table 6 summarizes all the conditions that were tested for pressing of "half-MEAs" consisting of a GDL-based anode with a Nafion membrane, of which the performances were benchmarked in the same half-cell setup as previously. Various compositions of the catalytic ink (**CyArg** on MWNT-COOH with or without 10% of fullerene and with or without Nafion at different concentrations) were assembled onto a 50 µm thick Nafion-212 membrane in different conditions of pressure and temperature. The benchmarking value for these electrodes was j_{ox}, the oxidation current density measured at 350 mV overpotential, 25°C and P_{H2} = 1 atm in a half-cell setup.

A trend that is observed is that for the fullerene-containing electrodes pressed at 1000 kg/cm², going from 25°C to 80°C for the assembly process systematically doubles $j_{ox,}$ while this is not true for electrodes without fullerene. However, at 500kg/cm², the effect of pressing temperature does not seem to follow any trend.

Overall, the beneficial parameters seem to be as follows. More Nafion within the ink is correlated to better current densities when adding a membrane. Also, the presence of fullerene in the ink increases the amount of Nafion ionomer tolerated by the catalyst. Hence the best current densities with a membrane are obtained for a 10% fullerene and 100% Nafion electrode (entry B4c2 in Table 6), at 68 mA/cm², with the membrane pressed at 80°C and 1000 kg/cm². This knowledge that the membrane itself and the assembly process are not detrimental to the activity of the anode was very useful in troubleshooting whole cells, as shown in Chapter IV.

Experiment number	Carbon support material	$\frac{m_{Nafion}}{m_{Carbon}}$ (%)	Membrane	MEA Assembly conditions		j_{ox} (mA/cm²) ± 15%
				P (kg/cm²)	T (°C)	
A1a1	MWNT-COOH	0	N/A			26
A1b1			Nafion 212	500	25	1
A1b2					80	7
A1c1				1000	25	18
A1c2					80	16
A2a1		5	N/A			22
A2b1			Nafion 212	500	25	12
A2b2					80	6
A2c1				1000	25	11
A2c2					80	15
A3a1		25	N/A			38
A3b1			Nafion 212	500	25	7
A3b2					80	5
A3c1				1000	25	7
A3c2					80	3
A4a1		100	N/A			22
A4b1			Nafion 212	500	25	8
A4b2					80	6
A4c1				1000	25	14
A4c2					80	28
B1a1	MWNT-COOH + fullerene	0	N/A			33
B1b1			Nafion 212	500	25	5
B1b2					80	4
B1c1				1000	25	22
B1c2					80	46
B2a1		5	N/A			29
B2b1			Nafion 212	500	25	9
B2b2					80	18
B2c1				1000	25	23
B2c2					80	42
B3a1		25	N/A			26
B3b1			Nafion 212	500	25	7
B3b2					80	15
B3c1				1000	25	21
B3c2					80	39
B4a1		100	N/A			52
B4b1			Nafion 212	500	25	6
B4b2					80	3
B4c1				1000	25	26
B4c2					80	68

*Table 6. Current densities for H_2 oxidation at 350 mV overpotential for various half-MEAs. Catalytic loading is 80 µL/cm² of **CyArg**/MWNT-COOH ink. Half-cell setup, S = 0.063 cm², electrolyte is H_2SO_4 0.5 M in H_2O, pH 0.3, 298K and P_{H2} = 1 atm. Standard deviation of j_{ox} is around 15 %.*

2. Deposition of the catalytic ink

In the previous studies performed in our group, the MWNT were suspended in a solvent such as ethanol or N-methyl-pyrrolidone (NMP) by sonication and deposited through either vacuum filtration or capillary evaporation onto the GDL, followed by their eventual functionalization then soaking in a solution of catalyst and finally deposition of ionomer.[42,72,79,81] Several disadvantages came with this method. First, a large amount of nanotubes and GDL was required to get homogeneous depositions through vacuum filtering. Second, although the amount of grafted catalyst was easily quantified by electrochemistry (see Chapter I), the majority of the catalyst was wasted in the remnant soaking solution. Third, the deposition of ionomer was very difficult to reproduce as it was operator-dependent and subject to many factors, such as pace and pathway of deposition and environment-dependant drying time. Finally, the soaking in a catalytic solution was far from current industry standards which prefer a spray- or coat-ready catalytic ink.

Together with the GDL/MWNT/**CyPy** system, the GDL/MWNT-COOH/**CyArg** system presented the strong advantage that the carbon suspension could be pre-mixed with the catalyst and ionomer and deposited in one step. This single step protocol is quite interesting as every additional step in a process can be a supplementary drawback from possible applications, and can hinder reproducibility if not perfectly mastered. The deposition of catalytic ink is very important as factors such as the drying kinetics of the ink can determine the developed surface of the electrode and its pore distribution, both critical characteristics of electrocatalytic materials. Furthermore, the chosen technique needs to be reproducible.

With an all-in-one ink, furthermore quite concentrated, the method we chose for deposition of electrodes was drop-casting. With the available equipment in our lab, several variations of drop-casting and vacuum filtration were tested. Drop-casting is the one which showed the best reproducibility, a key aspect for all our benchmarking studies. However, spraying of this ink with help of a simple air gun was possible and we did spray-coat anodes directly onto membranes which were integrated in functional fuel cells, as described in Chapter IV. This is a notable advantage for the scaling up of these electrodes to large surface areas, as it is the technique of choice for membrane coating in industrial setups.

a. Support material

The classical support material for fuel cell electrodes is a GDL, often covered in a micro-porous layer (MPL). The GDL is commonly made of carbon micro-fibres, sometimes covered in a thin layer of PTFE, woven together to form a mesh, fabric or more or less rigid paper. When choosing our support material for drop-casting, several factors had to be accounted for. First, the hydrophobicity of the surface determines the shape of the drop of ink, which is dispersed in water and ethanol, both polar solvents. Second, the rate of evaporation depends on the ability of the GDL to soak the solvent from the ink drop. Third, the presence or absence of an MPL and hence the roughness of the GDL surface determines to a large extent the porosity and thickness of the electrode. Finally, physical integrity and resistance to mechanical failure are largely due to the adhesive strength of the MWNT to the GDL support. While we were not interested in specifically characterizing all those features for lack of microscopic, materials science and chemical physics knowledge, we knew that they would be accounted for when looking at the current densities and reproducibility of electrodes deposited on different supports.

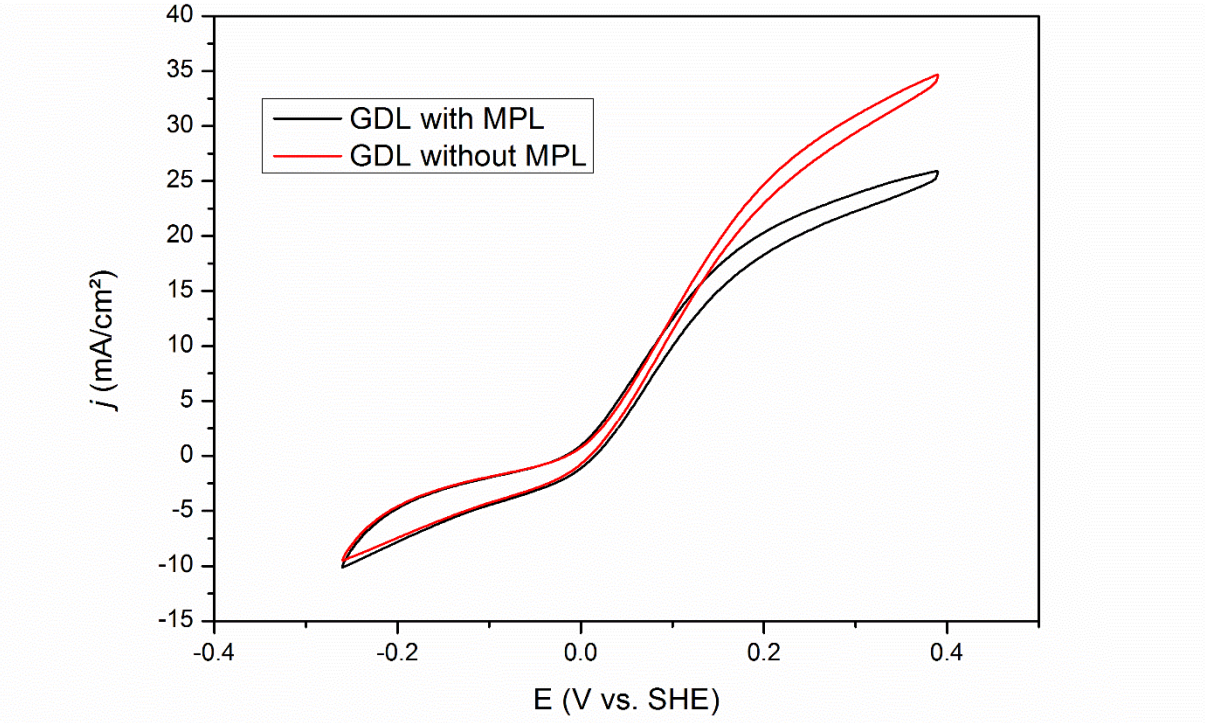

*Figure 10. Comparison of the current densities of a MWNT-COOH/**CyArg** electrode without fullerene of Nafion deposited onto a GDL with or without a microporous layer. Half-cell setup, S = 0.063 cm², electrolyte is H_2SO_4 0.5 M in H_2O, pH 0.3, 298K and P_{H2} = 1 atm.*

Four kinds of GDL were tested (CARBEL-CL P-02360 from Gore Fuel Cell Technologies, Sigracet GDL from SGL, and GDL with and without MPL from Paxitech), which were deemed representative of the variety of available products on the market for fuel cell electrode support

materials. All GDLs apart from the CARBEL-CL were of a rigidity similar to that of thick cardboard. We could not get reproducible current densities from the CARBEL-CL or the Sigracet GDL, due to handling problems when cutting the electrodes to size for the benchmarking apparatus. The ink did not stick at all to the Sigracet, and the CARBEL-CL, which is more of a carbon fabric than paper, fell apart when it was cut. The data displayed here in Figure 10 shows the difference of catalytic current between the GDL with and without MPL from Paxitech. While the proton reduction currents are exactly the same, the hydrogen oxidation currents are much better in the case of the GDL without MPL. We hence chose the GDL without MPL for future applications.

Cross cut SEM images of the GDL/MWNT-COOH/**CyArg** assembly are shown in Figure 11. The GDL/MWNT-COOH/**CyArg** assembly is facing down, with the catalyst on the bottom part of the images and the GDL on top. Here, the catalytic layer has detached from the GDL support and its geometric characteristics are easy to see. The CNT mat is flat, quite homogeneous in thickness, and seems very organized on the cross-section. On the bottom image, thickness of the catalytic layer has been measured in the neighbourhood of 20 µm on average for a 160µL/cm² loading of a 2:3 MWNT-COOH:**CyArg** ink without Nafion or fullerene. The layer seems almost stratified, as if it had been built by stacking layer upon layer of MWNTs. On the part of the catalytic layer detached from the GDL, some bundles of MWNTs are "poking out" as they were reaching in the spaces between the micro-fibres of the GDL, however they represent only a small portion of the overall MWNTs, meaning that most of the carbon material in the catalytic ink has not soaked into the GDL and in fact remains in the catalytic layer (CL).

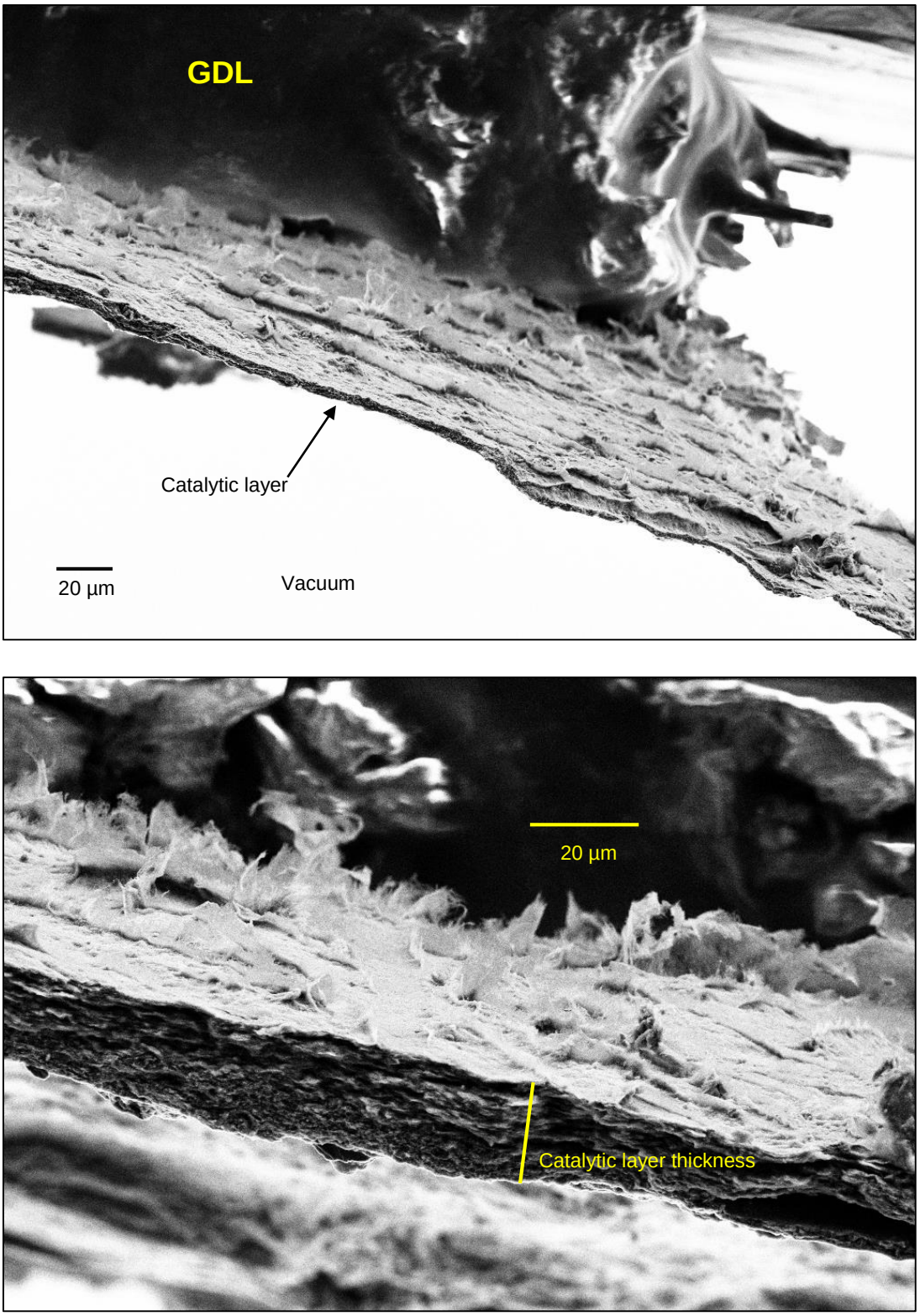

*Figure 11. Cross-cut SEM images of a GDL/MWNT-COOH/**CyArg** electrode with Nafion, deposited on a GDL without MPL. Bottom image is a zoom dead in the middle of the top one.*

This very organized structure is possibly one of the reasons for the very good reproducibility of current densities of these electrodes. Indeed, if the nanotubes have a long-range induced organization, the environment of the catalyst is probably less variable.

b. Amount of catalytic ink

All the above optimization ideas were qualitative: we changed the environment of the catalyst with a given amount of catalytic ink. When working with non-noble metals, it does not make sense to try and reduce the catalytic loading to a minimum. In fact, it is rather the opposite that is true. To reach a given power output, it is currently economically more interesting to have larger amounts of non-PGM catalyst and less stacks, as non-PGM catalysts cost less than the membrane and bipolar plates.[21] It should be noted that nowadays, the upper technological recommendation for thickness of non PGM anodes stands around 100 µm. This is due to the recommendation for thickness of a single MEA stack expected to not be thicker than 500 µm, and the upper limit of thickness for the cathode stands around 300µm.[18,114] However, most of Pt based anodes are much thinner than this because of how little catalyst is required for the anode compared to the cathode.

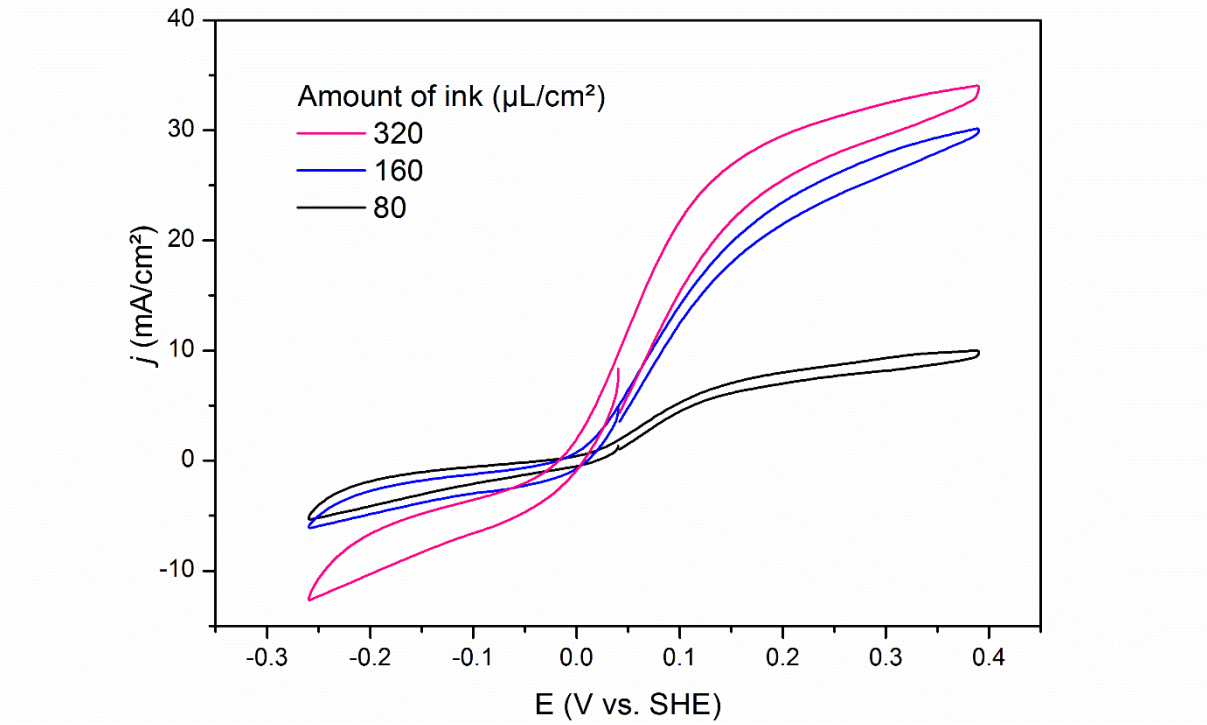

*Figure 12. Catalytic behaviour of GDL/MWNT-COOH/**CyArg** electrodes at various surface loadings of catalytic ink. Electrodes are made by depositing the 2:3 MWNT-COOH:**CyArg** ink and contain neither Nafion nor fullerene. Half-cell setup, S = 0.063 cm², electrolyte is H_2SO_4 0.5 M in H_2O, pH 0.3, 298K and P_{H2} = 1 atm.*

In the case of GDL/MWNT-COOH/**CyArg** electrodes without either Nafion or fullerene (Figure 12), the addition of more catalytic ink upwards of 160 µL/cm² is beneficial to proton reduction activity and somewhat beneficial for H_2 oxidation in the low overpotential region. The thicker electrodes show large capacitive currents which could be indicative of

inhomogeneity of current densities within the electrode or flooding of the electrode. Although the amount of grafted, electronically connected active sites has increased, shown by the increase in H^+ reduction current, all those sites are not in their current state capable of H_2 oxidation to their best ability. This, in addition to the fact that the capacitive current strongly increases when increasing catalytic loading, leads us to think that the electrode is quite thick and flooded with electrolyte, as capacitive current can increase along with the developed surface of the electrode in contact with electrolyte and hence the capacity of the electrical double-layer. It is obvious here that the catalyst is not in an ideal environment to perform to the best of its ability. Furthermore, at higher overpotentials the difference in HOR currents is almost negligible because of the diffusion plateau.

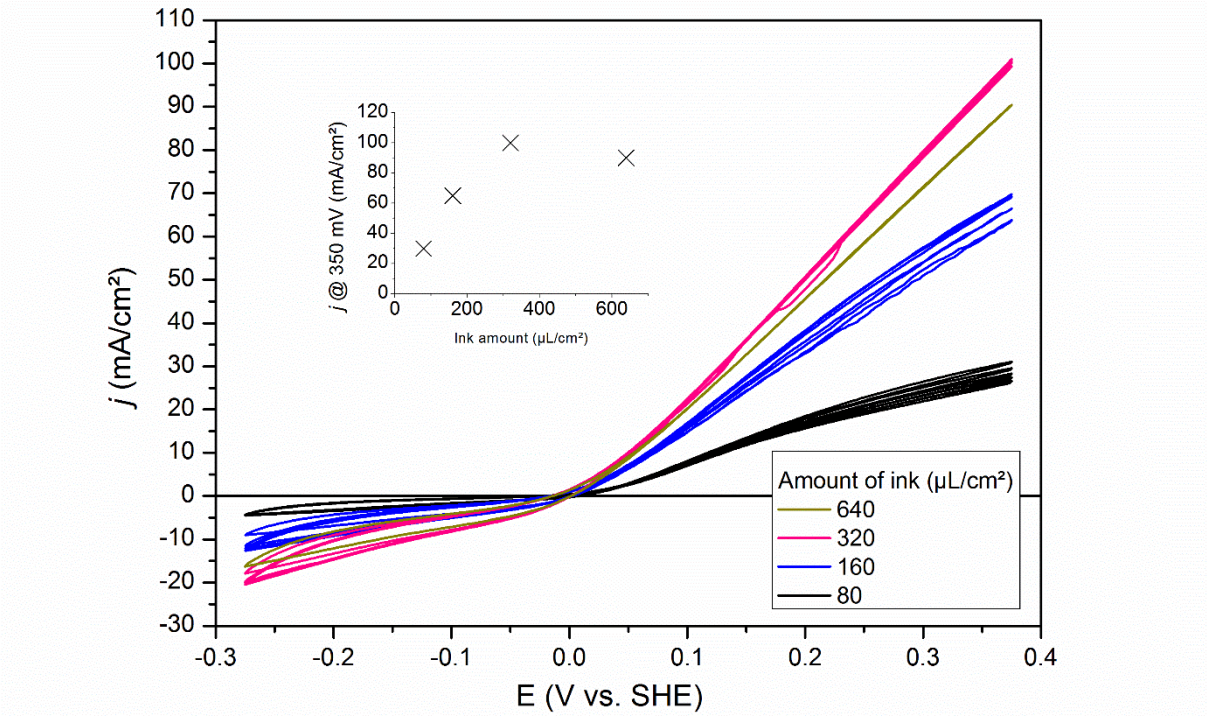

*Figure 13. Catalytic behaviour of GDL/MWNT-COOH/**CyArg** electrodes at various surface loadings of catalytic ink. Electrodes contain 10% fullerene and 100% Nafion in mass compared to that of carbon nanotubes. Inset: values of j at 350 mV overpotential for each CV. Current densities increase with the number of cycles as Nafion takes some time to hydrate. Half-cell setup, S = 0.063 cm², electrolyte is H_2SO_4 0.5 M in H_2O, pH 0.3, 298K and P_{H2} = 1 atm.*

On the other hand, in the case of the GDL/MWNT-COOH/**CyArg** electrodes that contained 10% fullerene and 100% Nafion, the addition of more ink resulted in a linear increase in current densities, with a doubling of j_{ox} following the doubling of catalytic loading, until 320 µL/cm² (Figure 13). At 320 µL/cm², strong current densities upwards of 100 mA/cm² were reached at 350 mV overpotential. At 100 mV overpotential, current densities of up to 25 mA/cm² are reached and 35 mA/cm² at 150 mV. Compared to the state of the art described in the

introduction, this performance stands at about 25 % of that of state of the art ultra-low loading Pt.[74] While it is not yet as efficient, it is however comparable and starts being interesting for low-power fuel cell applications. The best current densities are more than twice that of our most recently published results for **CyEster**,[76] and are observed at 25°C as opposed to 50°C.

Above 320 µL/cm² of catalytic ink, the current densities did not increase anymore. For large loadings, they sometimes were slightly lower. This was detrimental to the overall efficiency of the electrode expressed in A/mg_{metal}, and wasteful of material. Remarkably, even for the most loaded electrodes, the diffusion plateau does not reappear and capacitive current remains low, which is encouraging as to the ability of our best electrodes to retain adequate H_2 and H^+ diffusion even as thickness increases. Determination of the SL yields a value of 10 nmol/cm² for the best performing electrode, at 320 µL/cm². At 640 µL/cm², the SL is measured at the same value, leading us to think that the added catalytic ink is not addressed electrochemically.

3. Taking advantage of different grafting modes

The versatile grafting strategies inherent to DuBois catalysts could permit the grafting of complexes with different catalytic biases, such as **CyArg** and **CyPy**, which would be of particular interest for unitized regenerative fuel cell (URFC) applications.

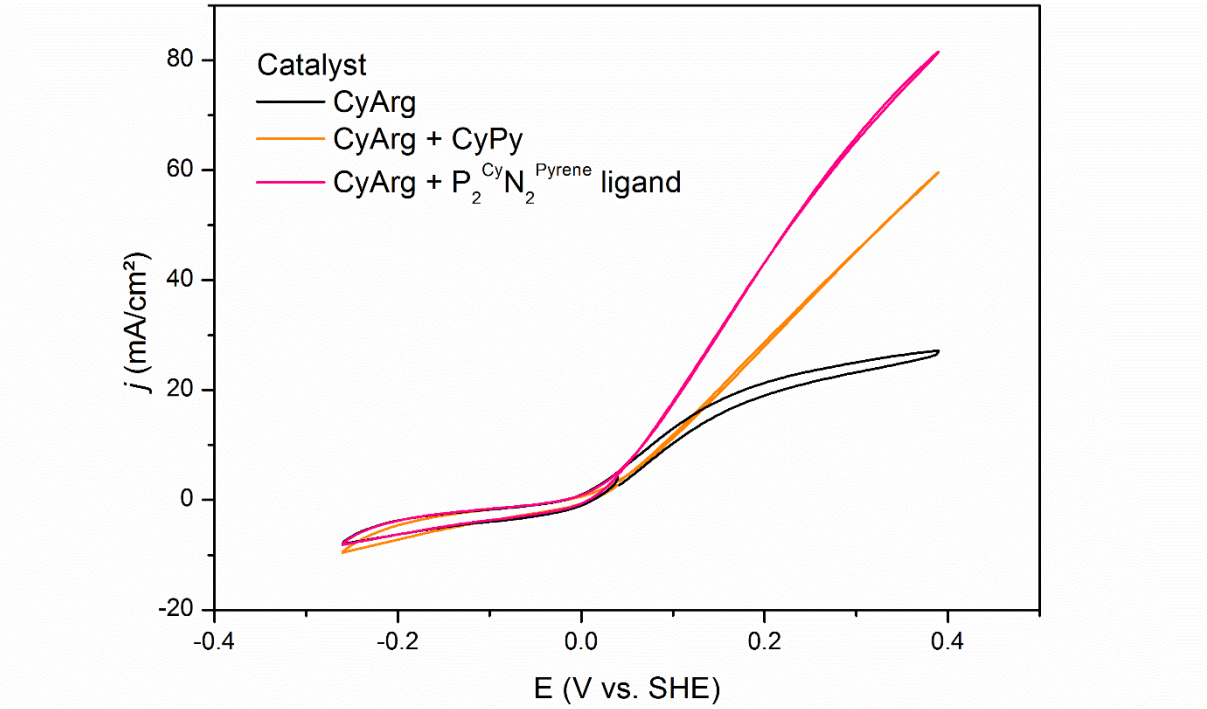

*Figure 14. CVs of GDL/MWNT-COOH/**CyArg** electrodes, with added **CyPy** and $P_2^{Cy}N_2^{Pyrene}$ ligand. Half-cell setup, S = 0.063 cm², electrolyte is H_2SO_4 0.5 M in H_2O, pH 0.3, 298K and P_{H2} = 1 atm.*

In Figure 14, we look at the effect of adding **CyPy** catalyst or the corresponding ligand ($P_2^{Cy}N_2^{Pyrene}$) to a GDL/MWNT-COOH/**CyArg** electrode that does not contain Nafion or fullerene. Strong increases in H_2 oxidation currents and disappearing of the diffusion plateau are observed after addition of both the complex or ligand. The effect is even stronger with the ligand alone than with the **CyPy** complex. However, current densities for proton reduction are not really affected. It is known that **CyPy** has a strong bias towards H^+ reduction, as shown in Figure 4,[79] hence we assume that it is not the **CyPy** complex that is responsible for this increase in catalysis but that it arises from either another catalytic species or a change in environment.

The results were quite encouraging, with current densities reaching 85 mA/cm² at 350 mV overpotential with a MWNT-COOH/**CyArg** ink loading of only 160 µL/cm². However a deep understanding of the structure of the catalytic sites within such electrodes has not yet been reached. Intricate equilibriums of complexation of the nickel can happen in the presence of different ligands in such an intricate environment. As mentioned in Chapter I, XAS is a method of choice to elucidate catalyst structure. Relevant samples have been submitted for characterization in order to elucidate this question, in collaboration with Solène Gentil at Université Grenoble Alpes, who has done some research about heterogeneous DuBois complexes bearing both a **CyPy** and a **CyArg** ligand. However, the data has not yet been processed and rationalized in sufficient detail to explain the structure of those catalytic mixtures. This opens up the way for polyvalent catalytic materials, capable of adaptive reactivity under flexible conditions, provided that every catalyst is stable towards all reactions.

4. Conclusion

Lessons taken from all the above points were used to formulate an optimized catalytic ink and find a facile and repeatable deposition method. From the carbon additives experiments, only fullerene was kept as we tried to keep the ink as simple as possible and its synergy with Nafion was very beneficial to implementation. The best GDL support was chosen, and the drop-casting method was selected. A protocol was developed for assembling a membrane onto our electrodes, at an optimized ratio of Nafion within the catalytic ink. We chose not to add the **CyPy** catalyst to our inks for integration, as we wanted to be able to characterize them thoroughly and keep them as simple as possible in order to understand fully the PEMFC that would be built with those anodes. However, preliminary results indicate that a **CyPy**/**CyArg** mixture may be very effective for HOR.

Hence, the best candidate for integration was the MWNT-COOH/**CyArg** ink with 10% of fullerene and 100% of Nafion in mass compared to the MWNT, deposited at 320 µL/cm², yielding a final coverage of 0.48 mg/cm² of **CyArg** (about 20 $\mu g_{Ni}/cm^2$) and 0.72 mg/cm² of carbon support material (MWNT-COOH + fullerene) with an electrode thickness sitting in the 10 - 30 µm region. These electrodes displayed stable currents for H_2 oxidation over several hours and offered the best current densities at all overpotentials. Qualitatively, they showed no diffusion limitation at high overpotentials and very little capacitive current. They are thoroughly characterized in Chapter III and their integration is described in Chapter IV.

5. Experimental section

All electrochemical measurements were carried out as described in the experimental section of Chapter I. Specifics of each series of experiments are described below.

a. Benchmarking of carbon additives

GDL/MWNT/**CyPy** electrodes were prepared in an analogous manner as described in the experimental section of Chapter I, with the difference that a part (10% in mass) of the MWNT was substituted for the appropriate carbon additive: Carbon micro-fibres (0.7 mm x 6 mm, Alfa Aesar), carbon nano-fibres (100 nm × 20-200 μm, Aldrich), graphene platelets (N006-010-P, Angstron) or fullerene (C_{60}, Sigma). The carbon additive was added at the same time as the MWNT, before the sonication steps. The electrodes were then deposited onto a GDL without MPL from Paxitech and benchmarked with the half-cell setup described in the introduction and Chapter I.

b. Nafion ratio

GDL/MWNT-COOH/**CyArg** electrodes were prepared in an analogous manner as described in the experimental section of Chapter I. After sonication of the carbon materials, an amount of Nafion ionomer (5% Nafion in a solution of lower aliphatic alcohols, Aldrich) indexed on the mass of carbon materials ($\frac{m_{Nafion}}{m_{Carbon}}$ = 5, 25 or 100%) was measured, vacuum-dried in order to remove solvents and dilution effects compared to the inks without Nafion, and added after the sonication of the carbon materials as described in Chapter I. The Nafion-containing carbon suspension was then sonicated for a further 3 hours before deposition.

c. Fullerene ratio

In standard MWNT-COOH/**CyArg** inks, fullerene was added at the same time as the MWNT-COOH in a ratio measured compared to the mass of MWNT-COOH. (1, 10, 50 and 100%) Current densities were measured and data points were spline connected to extrapolate a rough theoretical ideal fullerene to MWNT-COOH ratio.

d. Catalyst to support material ratio

Solutions of **CyArg** were made as described in Chapter I, however the amount of MES:HEPES buffer was decreased from 0.1 to 0.1 M. This allowed to maintain a stable pH while limiting

the amount of salt deposited onto the electrode. Concentrations of **CyArg** were as follows. 3 mg/mL for the 1:3 ratio and 6 mg/mL for the 2:3 ratio.

e. Nafion membrane conditioning

The Nafion membrane (Nafion-212, 50 µm thick, Sigma) was cut in square 5 x 5 cm pieces, and conditioned following standard procedures.[115] The membrane is sonicated first in H_2O_2 (10% in H_2O), then in H_2SO_4 (pH 0 in H_2O) then in H_2O for 30 min each with thorough rinsing in water between each step, then stored in distilled water and superficially dried before use.

f. MEA assembly

A homemade apparatus consisting of two thick (3 cm) bronze plates machined to micron-flatness on one face was made to yield a makeshift MEA assembly press from an IR pellet press.

GDL/MWNT-COOH/**CyArg** electrodes with different Nafion ratios were prepared and drop-casted onto a single piece of GDL, then pressed onto a pre-conditioned Nafion membrane for 60 seconds at either 500 or 1000 kg/cm² and either 25°C, 80°C or 140°C. Heating was achieved by pre-heating the bronze plates in an oven before pressing and temperature controlled via a probe inserted in the bronze plate.

g. Support material

The catalytic ink containing MWNT-COOH and **CyArg**, in a 2:3 ratio, as described above, was deposited onto GDLs both with and without MPL from Paxitech. Shape of the drop was affected but the surface of deposition was similar, of the order of 0.125 cm² for 20 µL of ink.

h. Amount of catalytic ink

Ink was added in 20 or 40 µL increments onto a 0.125 cm² area to reach the final surface concentration, allowing the ink to superficially dry for a couple of minutes in-between additions.

Chapter III – Advanced electrochemical characterization

In this part, we are interested in characterizing the behaviour of electrodes obtained through the optimization described in the previous chapter. First, we discuss the stability of our best performing electrode materials and look at some kinetic aspects of catalysis. Then, advanced electrochemical characterization of four types of electrodes is proposed. In the case of our molecular-engineered nanomaterials, we here use both micro-polarization and Tafel analysis as well as electrochemical impedance spectroscopy (EIS) to determine a catalytic turnover frequency (TOF) as well as provide a mechanistic description of catalysis. This represents the behaviour of the material as a whole and allows comparison of electro-assisted homogeneous catalysis, supported molecular catalysis and classical surface electrocatalysis.

1. Assessment of stability

The first point of interest regarding stability was stability over time of the best-performing electrodes. A chronoamperometry was recorded under catalytic conditions, at 350 mV overpotential for HOR, of the optimized electrode formulation described in Chapter II and is shown in Figure 1. Stable currents are observed at 90 mA/cm² over an hour.

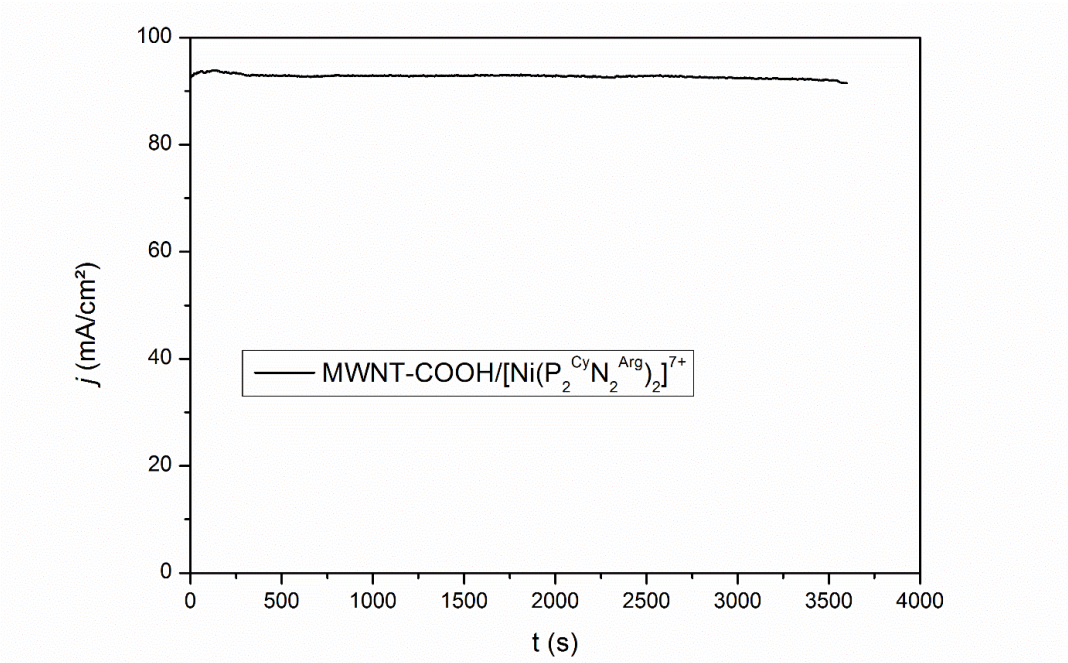

*Figure 1. Chronoamperometry of a MWNT-COOH/**CyArg** electrode containing Nafion (100 wt%) and fullerene (10 wt%) at 350 mV vs. SHE, in the presence of H_2. Half-cell setup, 320 µL/cm² loading, S = 0.063 cm², electrolyte is H_2SO_4 0.5 M in H_2O, pH 0.3, 298K and P_{H2} = 1 atm.*

For the data presented in Figure 1, a loading of 320 µL/cm² is used, showing that the best performing electrodes displayed stable catalytic currents. However, such high-loading electrodes take more time and catalyst to prepare. Hence as the qualitative catalytic behaviour was known to be the same, lower catalytic loadings are used for subsequent studies in this chapter, which explains the lower current densities.

Stability over turnover is not the only benchmark of interest. Carbon monoxide is a common contaminant of H_2 gas obtained from natural gas, petrol or biomass reforming. Ideally, H_2 gas in the future will be obtained from water through renewable processes, but for now it is important to show that catalytic systems can withstand – or at least easily recover from – exposure to moderate amounts of CO. Figure 2 showcases the stability of a MWNT-COOH/**CyArg** over an hour at 100 mV overpotential for HOR in the presence of 50 ppm of CO in the H_2 gas feed compared to that of 50 µg/cm² Tanaka Pt/C in the same conditions. Initially, the gas feed is H_2, it is then changed to H_2 + 50 ppm CO and after an hour reverted back to H_2 only. Sharp, brief drops in currents are due to the formation of bubbles on the electrode surface.

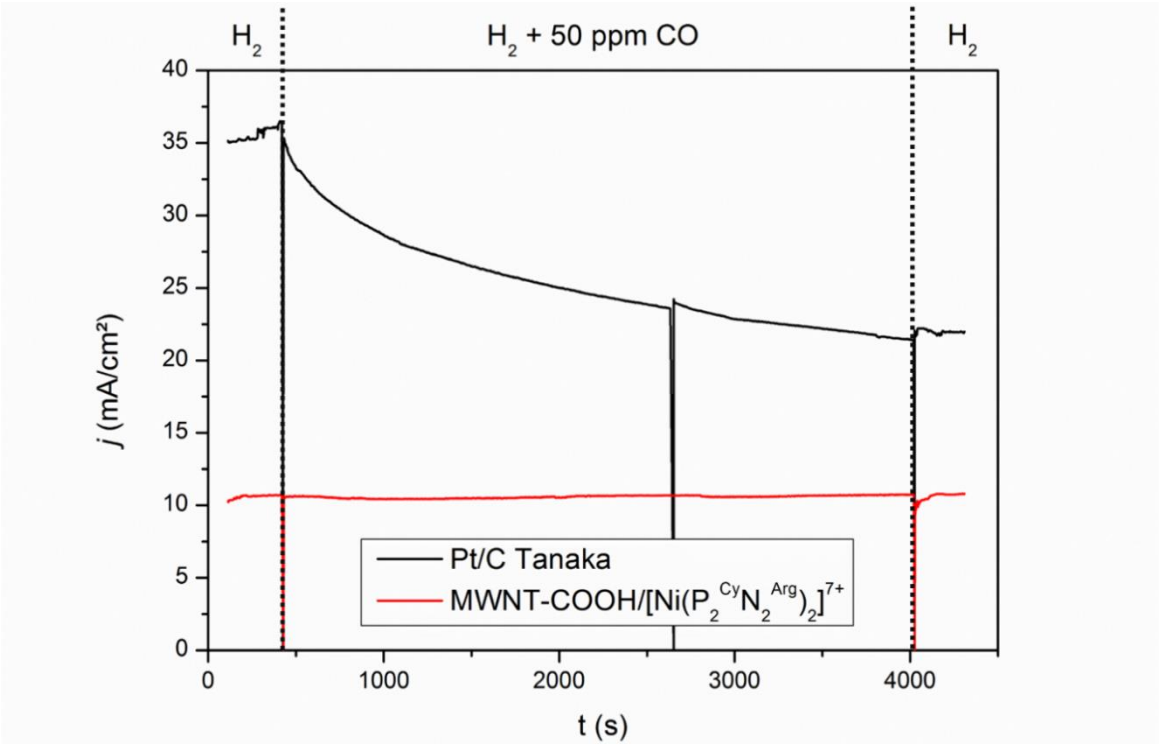

*Figure 2. Chronoamperometry of a 50µg/cm² Pt/C and a MWNT-COOH/**CyArg** electrode containing Nafion (100 wt%) and fullerene (10 wt%) at 100 mV vs. SHE, in the presence of H_2 with or without 50 ppm CO. Half-cell setup, 160 µL/cm² loading, S = 0.063 cm², electrolyte is H_2SO_4 0.5 M in H_2O, pH 0.3, 298K and P_{gas} = 1 atm.*

The Pt/C electrode shows a steady decrease in activity starting as soon as CO is added, and current becomes stable again when gas flow is reverted to pure H_2, but no recovery of initial current is observed. Despite lower overall current densities at those loadings, no such effect is observed for the MWNT-COOH-**CyArg** electrode, which retains stable current densities over the whole time of the experiment. This is attributed to the substrate selectivity of the molecular catalyst which is much greater than that of the Pt/C nanoparticles, as reported previously.[79]

2. Effect of temperature, activation energy

The effect of increasing temperature on HOR catalytic activity was studied for a MWNT-COOH/**CyArg** electrode. Temperature was increased from 25 to 55°C in 10°C increments, and a classical Arrhenius plot was traced by plotting $\ln(j) = f(\frac{1}{T})$, see Figure 3.

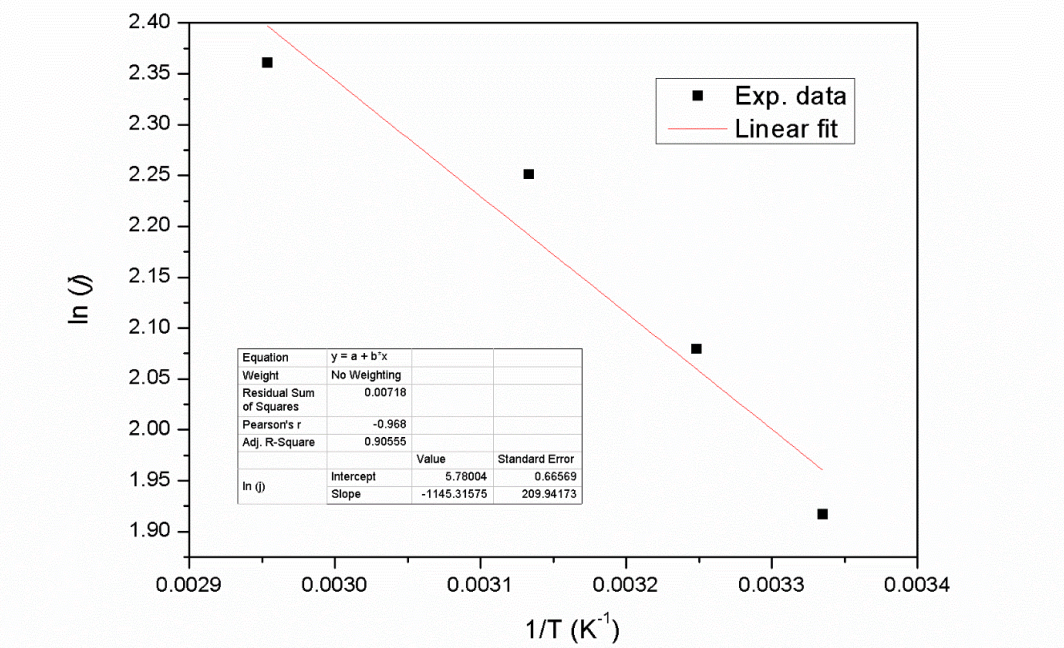

*Figure 3. Arrhenius plot for a MWNT-COOH/**CyArg** electrode without fullerene or Nafion. Current densities measured at 300 mV overpotential for H_2 oxidation. Half-cell setup, 160 µL/cm² loading, S = 0.063 cm², electrolyte is H_2SO_4 0.5 M in H_2O, pH 0.3, and P_{H2} = 1 atm, at 25, 35, 45 and 55°C*

The effect of temperature was studied at 300 mV overpotential, on the catalytic plateau (see black line, Figure 6), in order to verify that this plateau was indeed a diffusion plateau rather than the TOF_{max} plateau of the electrode. From the natural logarithm of the Arrhenius law noted:

$$\ln(j) = \ln(A) - \frac{E_a}{R}\frac{1}{T}$$

with A the pre-exponential factor, R the universal gas constant in kJ/mol/K and T in K, an activation energy E_a = 10 ± 2 kJ/mol was found. Such a low value is indicative that it is either

product or substrate mass-transport, rather than the intrinsic turnover frequency of the catalyst, that limits current densities.[72] This is in line with previous results from our group, which found an activation energy around 15 kJ/mol for a MWNT-NH_2/**CyEster** electrode[76] and a MWNT/**CyPy** electrode.[72] These values can be compared to that of hydrogenase enzymes in solution, reported to be within a broad 15 - 70 kJ/mol range,[35,116] and that of carbon-supported Pt catalysts, found to be in the 9 – 18 kJ/mol range.[75,77] A report by the group of Armstrong makes mention of a 19 kJ/mol activation energy for grafted *Escherichia coli* Hyd1,[117] but reserves on the validity of those results have been expressed by another group.[118] It appears that, even grafted, the TOF of **CyArg** is sufficiently high that mass-transport to the active site is the limiting factor.

3. Micro-polarization and Tafel analysis

In this part and the next, we compare the electrochemical behaviour of the four types of MWNT-COOH/**CyArg** electrodes described at the end of Chapter II. Those four electrodes differ in the composition of the catalytic ink: they either contain Nafion (100 wt% compared to MWNT-COOH), fullerene (12 wt%), both, or neither. CVs of these four electrodes are depicted in Figure 4.

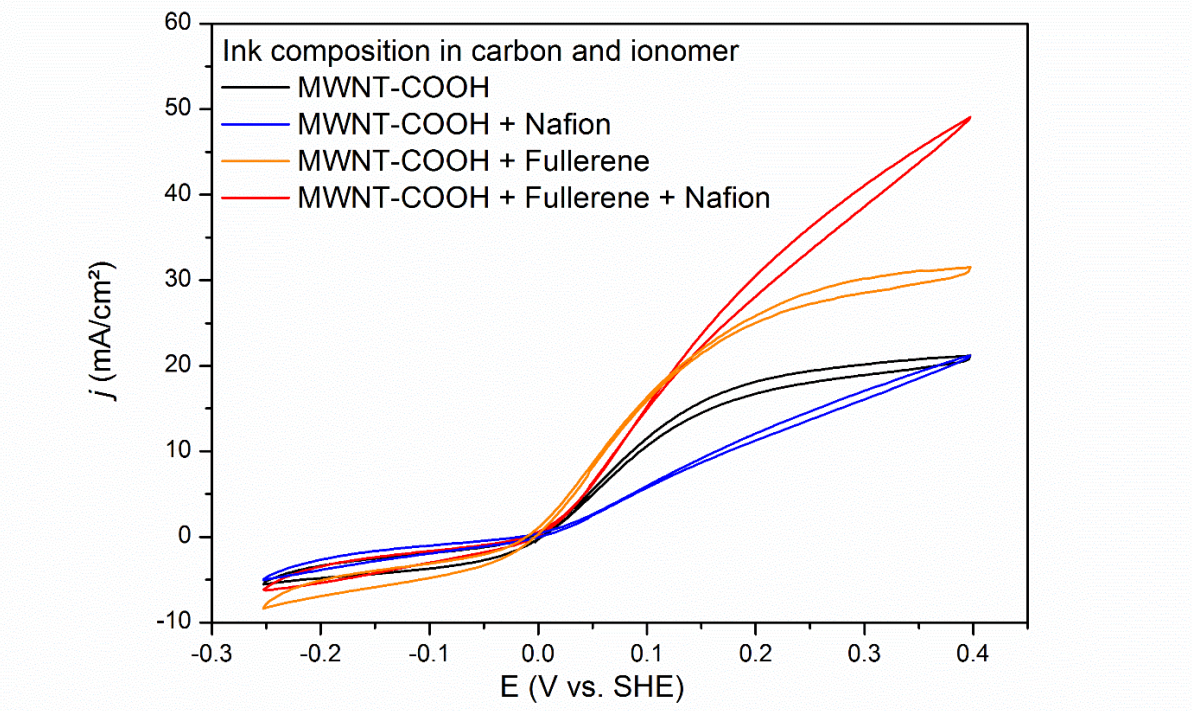

*Figure 4. CVs illustrating the difference in catalytic behaviour at high overpotentials of MWNT-COOH/**CyArg** electrodes in the presence or not of Nafion ionomer and fullerene in the catalytic ink. Half-cell setup, 160 µL/cm² loading, S = 0.063 cm², electrolyte is H_2SO_4 0.5 M in H_2O, pH 0.3, 298K and P_{H2} = 1 atm.*

First, we evaluate the kinetic characteristics of the four systems using micropolarization and Tafel analysis. As described in the introduction, Tafel plots are obtained by plotting $\log_{10}(j)$ as a function of overpotential. Here, overpotential is termed E_{IRcorr} and is compensated for ohmic drop (obtained as the product of internal resistance and current density at a given potential, as described in Chapter IV) , and j is given in mA/cm^2_{geo}, the geometric current density. Figure 5 presents the Tafel plots of all four electrodes for overpotential values between 0 and around 200 mV for HOR. Here, potentials were corrected for ohmic drop using the following equation:

$$E_{IRcorr} = E_{applied} - iR$$

with i in mA the current at a given $E_{applied}$ and R the resistance of the cell.

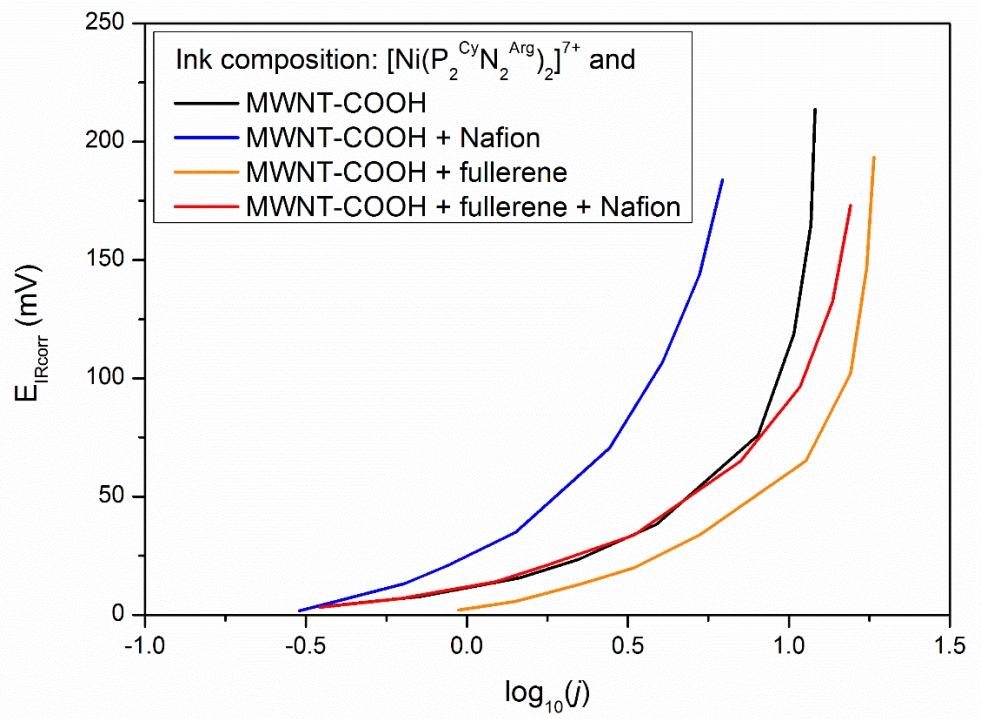

Figure 5. Tafel plots for the HOR region of the four electrodes presented in Figure 6. Potential is corrected for ohmic drop and plotted against the $\log_{10}$ of current densities. Half-cell setup, 160 µL/cm² loading, S = 0.063 cm², electrolyte is H_2SO_4 0.5 M in H_2O, pH 0.3, 298K and P_{H2} = 1 atm.

The cathodic and anodic current contributions at an electrode at any given potential are given by the Butler-Volmer law, written hereafter:

$$j = j_0 \left[e^{\frac{\alpha n F \eta}{RT}} - e^{-\frac{(1-\alpha) n F \eta}{RT}} \right]$$

with j the current in mA/cm² at a given overpotential η in V, F the faraday constant, n the number of electrons involved in the reaction (2 in the case of HOR), R the gas constant, T the temperature in K and j_0 the exchange current density in mA/cm² and α the charge transfer

coefficient between anodic and cathodic current, by default 0.5 for a fully reversible reaction. The first and second exponential terms represent the anodic and cathodic contributions respectively.

At low overpotential, this relationship simplifies by Taylor expansion to the following linear expression which describes the micro-polarization of the electrode:

$$j = j_0 \frac{nF}{RT}$$

This relationship gives access to the exchange current density of an electrode, j_0.

The description of electrochemical systems with Tafel plots arises from the simplification of the Butler-Volmer law at high overpotentials (that is, when cathodic current is negligible when studying the anodic reaction and vice-versa, usually η further form equilibrium than ± 30 mV). Then, the Tafel equation can be written as follows:

$$\eta = a + b \log(j)$$

In which a is a pre-exponential term, which gives access to the exchange current density j_0 ($\log(j_0) = -b/a$) and *b*, the Tafel slope denotes how much overpotential is required to increase current by an order of magnitude. In the case of "two-dimensional" platinum electrodes, the Tafel slope can be used as insight to understand the catalytic mechanism at play, as it takes characteristic values depending on the pathway for HOR and the rate-determining step in this pathway.

Two common model pathways for HOR on Pt electrodes, the Heyrovsky-Tafel and Heyrovsky-Volmer mechanisms, are described hereafter.[119] These pathways are both two-step reactions, named after their elementary steps, which are given hereafter along with the value of b, the Tafel slope, if the step in question is rate-determining.[120] S is an active site of the electrocatalytic material and H·S a catalytic site-bound atomic hydrogen.

The Tafel step, s_T, b = 29 mV/decade

$$H_2 + 2\ S \rightleftharpoons 2\ H \cdot S$$

the Heyrovsky step, s_H, b = 38 mV/decade

$$H_2 + S + H_2O \rightleftharpoons H_3O^+ + H \cdot S + e^-$$

and the Volmer step, s_V, b = 116 mV/decade

$$H \cdot S + H_2O \rightleftharpoons H_3O^+ + S + e^-$$

Those elementary steps are combined, with stoichiometric equilibration, to describe different reaction pathways. The Heyrovsky-Tafel pathway consists of + 2 s_H and – 1 s_T, while the Heyrovsky-Volmer pathway consists of + 1 s_V and + 1 s_H, in which (+) indicates the elementary step as written and (–) the reverse reaction.

Hence, the Heyrovsky-Tafel pathway can be written as follows:

$$+ 2\, s_H: \quad 2H_2 + 2S + 2H_2O \rightleftharpoons 2H_3O^+ + 2H \cdot S + 2e^-$$

$$- 1\, s_T: \quad 2\, H \cdot S \rightleftharpoons H_2 + 2\, S$$

and the Heyrovsky-Volmer pathway:

$$+ 1\, s_H: \quad H_2 + S + H_2O \rightleftharpoons H_3O^+ + H \cdot S + e^-$$

$$+ 1\, s_V: \quad H \cdot S + H_2O \rightleftharpoons H_3O^+ + S + e^-$$

Both of those pathways eventually lead to the same overall reaction:

$$H_2 + 2\, H_2O \rightleftharpoons 2\, H_3O^+ + 2\, e^-$$

However, these systems tremendously differ from our catalytic materials. Closer to the work in this project, in the case of grafted molecular catalysts, the group of Costentin and Savéant has reported that a Tafel slope of 60 mV/decade can be expected in the case of a single electron transfer with one rate determining step.[121,122]

In the case of porous materials, the same group reports that the electrochemical response of grafted catalysts can deviate from the expected Tafel behaviour, and present a Tafel slope of 120 mV/decade. This is due to sluggish electron transfer which arises from the dispersion of sites in the pores, where they can be reached by charges only through long and diverse electronic pathways through the carbon support material and electrolyte within the pores.[123] Clearly the Tafel plots shown in Figure 5 hardly contain a linear region. Figure 6 presents the best Tafel plots of the four electrodes presented above in the low overpotential region corresponding to unhindered catalysis, and Table 1 sums up the values of exchange currents and Tafel slopes for those electrodes.

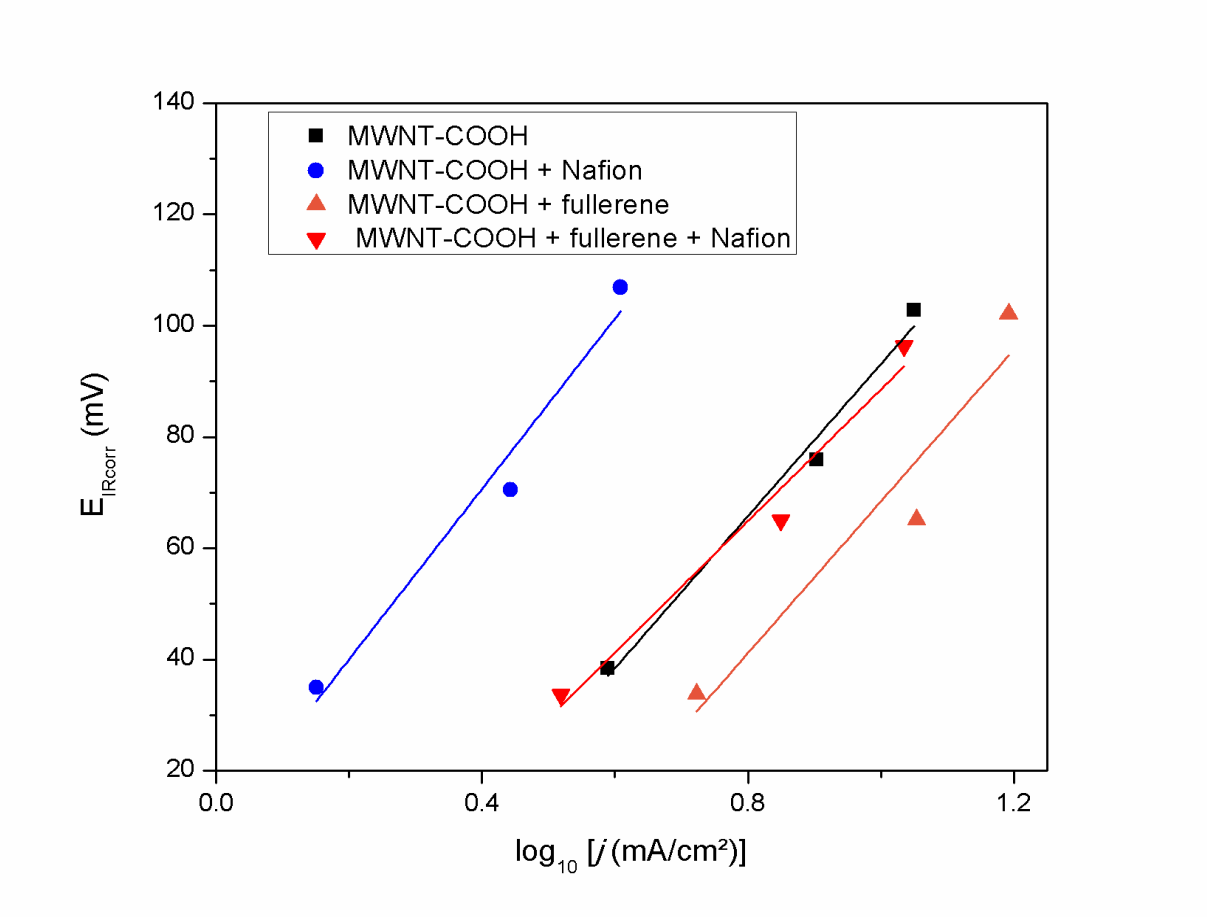

Figure 6. Linearization of the Tafel plots for HOR of the four systems in the 25 to 100 mV overpotential region. Half-cell setup, 160 µL/cm² loading, S = 0.063 cm², electrolyte is H_2SO_4 0.5 M in H_2O, pH 0.3, 298K and P_{H2} = 1 atm.

Carbon and ionomer composition	***j_0 (mA/cm²$_{geo}$)***	***b (mV/decade)***
MWNT-COOH	2.2	135 ± 16
MWNT-COOH + Nafion	0.89	153 ± 26
MWNT-COOH + fullerene	3.4	136 ± 29
MWNT-COOH + fullerene + Nafion	1.8	118 ± 19

Table 1. Values of the exchange current, j_0 (mA/cm²$_{geo}$) and the Tafel slope, b (mV/decade) obtained by linearization of the Tafel plots. Half-cell setup, 160 µL/cm² loading, S = 0.063 cm², electrolyte is H_2SO_4 0.5 M in H_2O, pH 0.3, 298K and P_{H2} = 1 atm.

These Tafel slope values of around 120 to 150 mV/decade are similar to those reported by Savéant and co-workers and are in line with the very porous electrode made from carbon nanotubes. No mechanistic information can hence be obtained from these Tafel slope values.

The other metric of interest obtained from these Tafel plots is the current exchange density, j_0 in mA/cm²$_{geo}$. However, it cannot be obtained from Tafel linearization, as the electrodes do not seem to follow a standard Tafel behaviour. Instead, j0 values can be obtained from the

polarization resistance of the electrode at low overpotentials (see above). Here, values between 0.89 and 3.4 mA/cm²$_{geo}$ are obtained, while for Pt catalysts a value of around 100 mA/cm²$_{geo}$ is reported for 1.7 µg$_{Pt}$/cm² electrodes.[75] For our MWNT-COOH/**CyArg** with fullerene and without Nafion, which has the best j_0 at about 3.4 mA/cm², if the effective catalytic loading could be increased thirtyfold while retaining the same properties, our systems would perform as well as state of the art ULL Pt electrodes. As discussed in Chapter II, increasing SL still presents a lot of challenges. However, only 5 % of the loaded catalytic sites are electrochemically active (see Chapter I). If all the loaded catalytic sites were accessible and active, a factor of 20 would already be reached. Further work on optimization should consider such problematics.

From the value of j_0 and that of site loading measured for each electrode by CV in non-aqueous electrolyte, a simple calculation allows us to determine the TOF of a single site, using the formula:

$$TOF = \frac{j_0}{2F \times SL}$$

with TOF in s^{-1}, j_0 in A/cm², F = 96500 A.s/mol, and SL in mol/cm². This yields values of TOF of the same order of magnitude, roughly between 1 and 3 s^{-1}, as shown in Table 2 for electrodes with a catalytic ink loading of 160 µL/cm² this. Of note, if there was no effect of Nafion or fullerene on the catalytic mechanism of **CyArg** for HOR, these values should be identical for all four electrodes.

Carbon and ionomer composition	***SL (nmol/cm²)***	***j_0 (mA/cm²)***	***TOF (s^{-1})***
MWNT-COOH	4.6	1.2	1.4
MWNT-COOH + Nafion	3.2	0.62	0.93
MWNT-COOH + fullerene	3.9	2.0	2.7
MWNT-COOH + fullerene + Nafion	3.6	1.2	1.7

*Table 2. SL, j_0 and TOF values for four **CyArg** electrode compositions. Half-cell setup, 160 µL/cm² loading, S = 0.063 cm², electrolyte is H_2SO_4 0.5 M in H_2O, pH 0.3, 298K and P_{H2} = 1 atm.*

However, this method of determining TOF might not be ideal as j_0 reflects the amount of catalytic sites at the triple boundary of H_2, H^+ and electron networks which enables catalysis, while SL, as determined here, takes into account all catalytic sites which are electronically connected regardless of whether they able to do catalysis. Therefore, we think that these are low estimates of the TOF of the truly active catalysts and that variation between those values

does not represent an actual change in the catalytic mechanism, but might actually rather represent the difference in amount of catalytic sites able to do turnover compared to that of sites which are merely electronically connected. TOF values are calculated more accurately with the help of EIS, as described in the next part of this chapter, and are then compared to that of Pt/C catalysts and hydrogenase enzymes.

4. Electrochemical impedance spectroscopy models for catalytic activity

In this part, we propose electronic models for catalysis through impedance spectroscopy. While the physical phenomena causing experimental observations do not change whether they are looked at from the point of view of EIS or other electrochemistry techniques such as the Tafel analysis presented above, EIS provides a set of useful abstractions and models which can help get a finer understanding of those phenomena. Combined with other characterization techniques, EIS is a powerful tool for deep chemical physics and mechanistic understanding of electrochemical systems.[17,26,124] In this part, all potentials are corrected for ohmic drop as described above for the Tafel analysis, and quoted against the OCV of the circuit. The OCV represents the equilibrium potential of the reaction, hence potentials are here equivalent to overpotentials.

a. A brief introduction to EIS

In classical electrochemistry, such as CV or CA measurements, a direct (DC) potential, or current, is applied to an electrochemical system, yielding a direct response following Ohm's law:

$$E = RI$$

Hence, when measuring a CV, for instance, measuring the current is indirectly measuring the resistance of the system to the passage of current. For catalytic materials, this resistance depends among other things on the ability of the system to do catalytic turnover.

On the other hand, EIS takes advantage of the wealth of information contained in the response of an electrochemical system submitted to the constraint of an alternating (AC) potential or current. This is illustrated in Figure 7. In this work, we apply a potential rather than a current, and this is termed potentiostatic electrochemical impedance spectroscopy (PEIS).

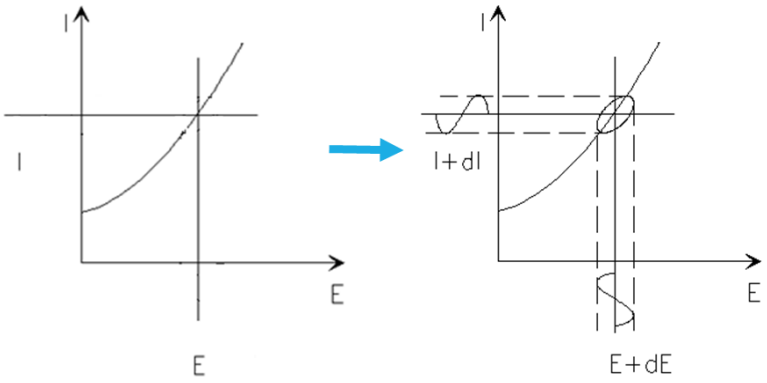

Figure 7. Going from DC potential electrochemistry to AC potential electrochemistry.

In this case, the system opposes impedance, rather than resistance, to the passage of current. Variations of potential are chosen sufficiently small for the electrode to respond linearly to these variations. Under this assumption, the electrode can be considered as a linear system. Parameters on which the characteristics of the electrode depend are assumed to remain constant during the measurement process. Under this assumption, the electrode can be considered as a time-invariant system during the measurement time. Jointly, these two assumptions allow to consider the electrode as a linear and time-invariant system regarding the additive input-output variations and during the measurement time. Here, the PEIS amplitude modulation was chosen to be of ± 2 mV as the systems displayed a linear I/E response over such an amplitude.

Impedance, noted Z, can be defined as follows. It is a complex number in which the real component is resistance and the imaginary component is the reactance to the passage of current. Reactance results in a phase angle, or dephasing, of the AC signal of current compared to that of the potential. In its Cartesian form, impedance is noted:

$$Z = R + jX$$

with R the resistance, j the imaginary number and X the reactance. In polar form, it is written:

$$Z = |Z|e^{\arg(Z)}$$

In which the absolute value of Z is the resistance and its argument, arg(Z), is the phase angle between the voltage and current. In practical terms, phase angle represents capacitive phenomena such as double-layer equilibration or local accumulation of charges.

Impedance of some electrochemical phenomena depends on frequency and follows characteristic trends, hence it is possible to scan impedance response over a range of frequencies. This is electronic impedance spectroscopy. Impedance data can be plotted in several ways. For instance, plotting the imaginary part of impedance as a function of the real

part, a so-called Nyquist plot, gives a useful visual representation of impedance response as a function of frequency. This is the representation chosen in this work.

In a second time, EIS spectra can be simulated from equivalent electronic circuits with simple components which each represent an electronic phenomenon happening at the working electrode. These components have a number of intrinsic variables in order to fit the experimental data. For instance, the impedance of a **R** element, a simple resistor, will be the purely real number:

$$\mathrm{Z}_R(\mathrm{f}) = R$$

which does not depend on frequency and denotes an attenuation of the amplitude of the current without phase angle. On the other hand, the impedance of a **C** element, a capacitor, will be the purely imaginary number:

$$\mathrm{Z}_C(\mathrm{f}) = \frac{1}{Cj2\pi f}$$

in which C in F is a capacitance, j the imaginary number and f the natural frequency in Hz.

This impedance depends on frequency and denotes a dephasing of the current without any attenuation in amplitude. EIS models can combine several simple components, some with a physical reality such as **R** and **C** and some which are rather mathematical abstractions that well represent a particular electrochemical phenomenon.

All the difficulty of EIS interpretation lies in the choice of those models, which base hypotheses have to be in accordance with the supposed physical reality of the system and which constituents have to be carefully chosen in order to be relevant. Someone[citation needed] once said "Give me two exponential functions and I will fit an elephant": it is the kind of risk inherent to improper EIS interpretation.

For our catalytic systems, we fit our data in two times. First, we find a common base to all our inks which we call "unhindered" catalysis, in the 0 to 50 mV overpotential region, in which the current is directly proportional to overpotential. The electronic behaviour in this region is fitted with an equivalent circuit containing an element assigned to unhindered catalysis. In a second time, the behaviour of our systems at higher overpotentials is fitted with fixed values for the catalytic parameters, to explain the catalytic plateaus observed in certain cases and the difference in behaviour of different electrodes at higher overpotentials.

b. EIS model for pure catalysis: 0 to 50 mV overpotential

Concurrently with the Tafel data studied above, EIS spectra of the electrodes in the 0 – 50 mV overpotential region were recorded. They were fitted with an **R1 + G1 + C2/R2** equivalent circuit, in which **R1** is the resistance of the setup, **C2/R2** represents the electrochemical double layer as an imperfect capacitor and **G1**, a Gerischer element, represents unhindered catalysis. This circuit is represented below in a standard electronic schematic:

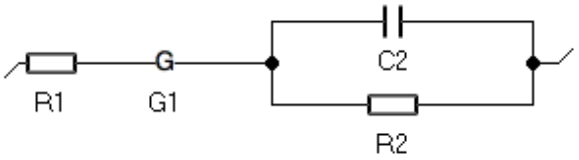

The Gerischer circuit element was originally derived to describe a redox phenomenon with a preceding chemical reaction happening in solution,[125,126] as per the equation below for an oxidation reaction:

$$A \xrightarrow{k} Red \xrightarrow{-ne^-} Ox$$

In the case of HOR on a catalytic site "Cat", this equation could be written as:

$$Cat + H_2 \xrightarrow{k} Cat\text{-}H_2 \xrightarrow{-2e^-} Cat + 2\,H^+$$

In which the observed preceding step would be the rate-determining step of the catalytic cycle for HOR at a catalytic site, which in the case of **CyArg** is the addition of H_2. The impedance of the Gerischer element takes the form:

$$Z_G(f) = \frac{R_G}{\sqrt{1 + j2\pi f \tau_G}}$$

In which R_G (Ω) is the resistance of the Gerischer circuit, j the imaginary number, f (Hz) is the natural frequency and τ_G (s) the time constant of the Gerischer circuit. τ_G is the reciprocal to the time constant k (in s^{-1}) which in our case would represent the TOF of a single catalytic site.

The impedance of the **C2/R2** element is of the form:

$$Z_{C/R}(f) = \frac{R_{CT}}{1 + j2\pi f R_{CT} C_{DL}}$$

in which R_{CT} and C_{DL} describe the ion transport within the double layer of the electrode.[127]

The impedance of the whole **R1 + G1 + C2/R2** circuit, Z, is simply the addition of the impedances of **R1**, **G1** and **C2/R2**, and is written:

$$Z(f) = R_{cell} + \frac{R_G}{\sqrt{1 + j2\pi f \tau_G}} + \frac{R_{CT}}{1 + j2\pi f R_{CT} C_{DL}}$$

in which R_{cell} is the cell resistance, or resistance of the setup.

First, the analysis process is detailed for a MWNT-COOH/**CyArg** electrode without fullerene nor Nafion. Figure 8 presents the evolution of the impedance spectra, plotted in a Nyquist representation, as a function of overpotential.

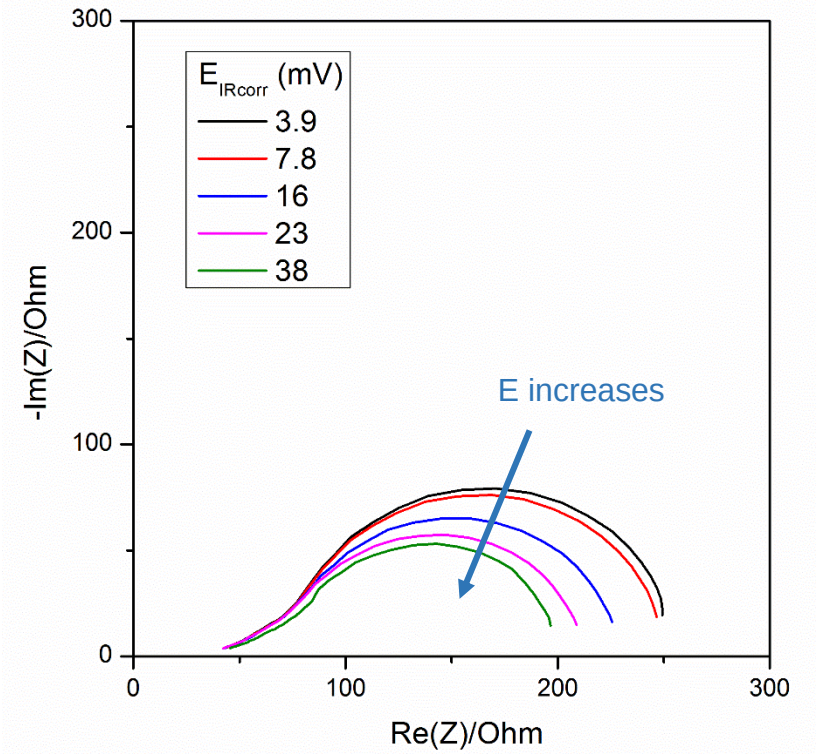

*Figure 8. Nyquist plots of PEIS spectra of a MWNT-COOH/**CyArg** electrode without Nafion or fullerene at several overpotentials for HOR. Half-cell setup, S = 0.063 cm², electrolyte is H_2SO_4 0.5 M in H_2O, pH 0.3, 298K and P_{H2} = 1 atm.*

It appears from a first look at these results that the overall impedance of the system decreases as potential is increased. There is both less resistive (abscissa) and capacitive (ordinate) contributions with increasing potential. This is line with a linear *j* = f (E) response in the low overpotential region, with more current, or less impedance, at higher overpotentials.

One example of a spectrum fitted with a **R1 + G1 +C2/R2** circuit at 3.9 mV overpotential for HOR for is given in Figure 9. Table 3 gives the fit values for the data presented in Figure 9.

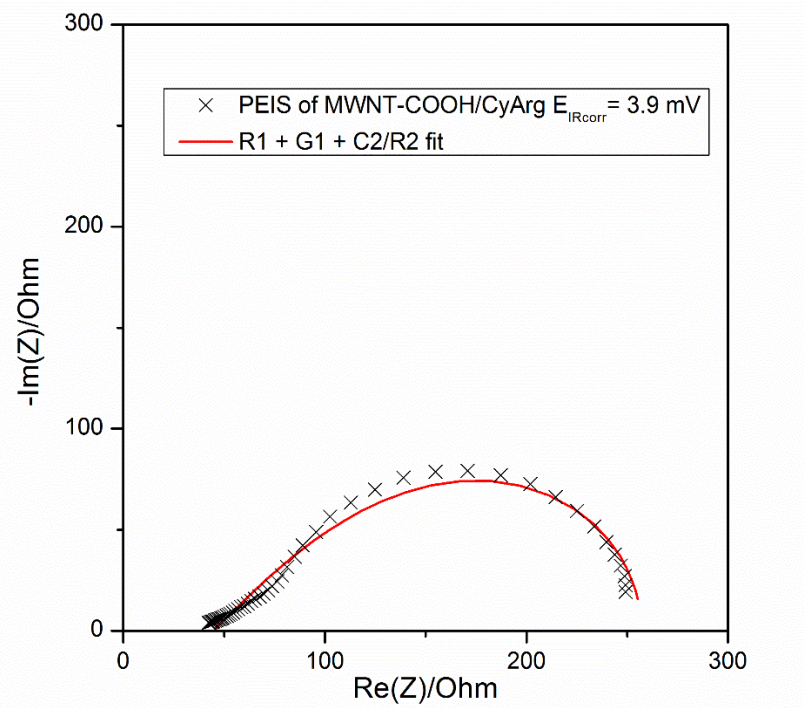

*Figure 9. Nyquist plot of a PEIS spectrum of a MWNT-COOH/**CyArg** electrode without Nafion or fullerene at E_{IRcorr} = + 3.9 mV overpotential for HOR, fitted with a **R1 + G1 + C2/R2** circuit. Half-cell setup, 160 µL/cm² loading, S = 0.063 cm², electrolyte is H_2SO_4 0.5 M in H_2O, pH 0.3, 298K and P_{H2} = 1 atm.*

E_{IRcorr} (mV)	R_{cell} (Ω)	R_G (Ω)	τ_G (s)	R_{CT} (Ω)	C_{DL} (mF)
3.9	45	211	0.23	30	3.2
7.8	48	204	0.25	32	3.0
16	50	179	0.23	30	2.3
23	50	160	0.225	31	1.8
38	55	145	0.27	30	1.8

*Table 3. Fit values in the 0 – 50 mV overpotential region for a **R1 + G1 +C2/R2** fit of PEIS spectra of a MWNT-COOH/**CyArg** electrode without Nafion or fullerene. Half-cell setup, S = 0.063 cm², electrolyte is H_2SO_4 0.5 M in H_2O, pH 0.3, 298K and P_{H2} = 1 atm.*

One of the steps of validating a model in EIS is to look at the evolution of the values of the different variables as a function of potential (other validation factors can be found in the experimental section). Here, we expect the following trends for our variables: R_{cell} should remain stable, as it is the overall resistance of the electrochemical setup. R_G should diminish then stabilize with increasing potential. Indeed, the overall current density of the electrode increases with overpotential following a Tafel law, indicating that more and more catalytic sites are involved in catalysis following the Nernst equation, until all sites are turning over at which point R_G stabilizes. Figure 10 presents the evolution of R_G for all four electrodes. What is expected is indeed observed, with a more pronounced decrease for the MWNT-COOH/**CyArg**

electrode without Nafion or fullerene and a value of R_G which does not stabilize as well as for the other three electrodes, a phenomenon yet to be explained. The overall resistance of the four electrodes to catalysis is in line with the data of Figure 6, with less resistance for larger current densities. This further supports the use of this **G1** element to model catalysis.

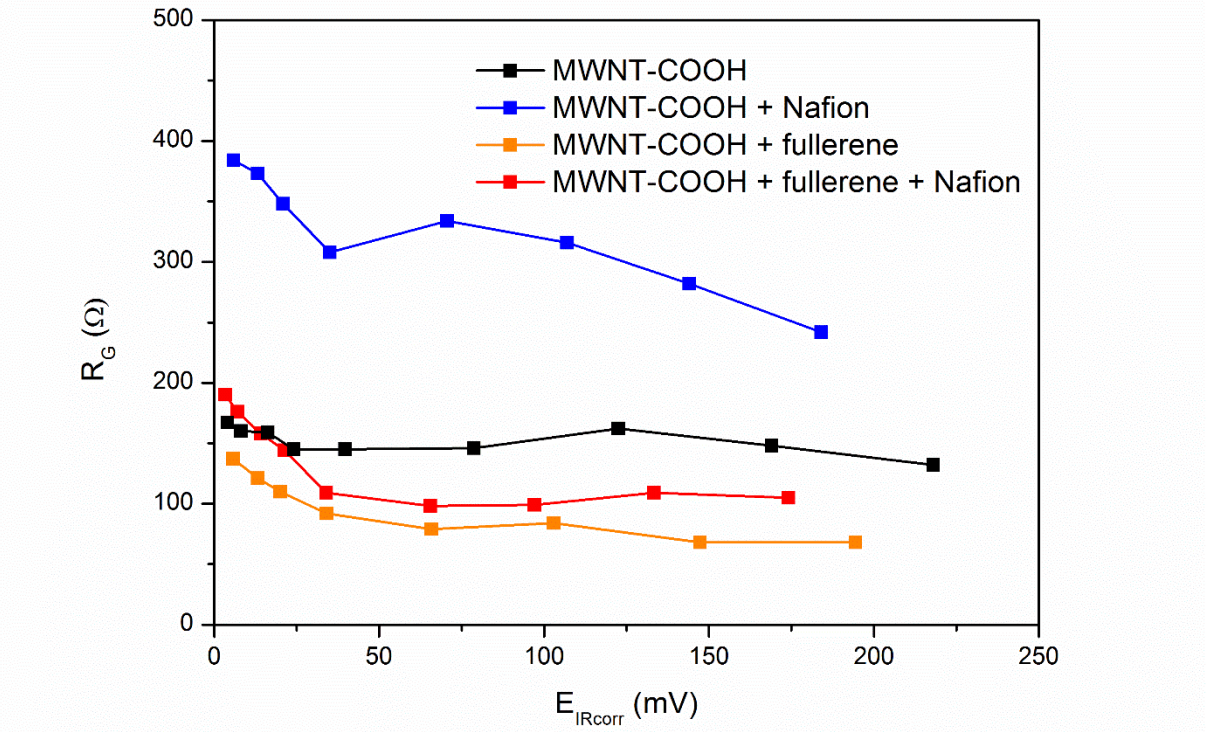

Figure 10. R_G values as a function of potential for all four electrodes. Half-cell setup, 160 µL/cm² loading, S = 0.063 cm², electrolyte is H_2SO_4 0.5 M in H_2O, pH 0.3, 298K and P_{H2} = 1 atm.

The value of τ_G should not change, as it represents the TOF of a single catalytic site and does not depend on overpotential for a given catalytic mechanism. This is indeed observed. The value of C_{DL} should diminish and that of R_{CT} should increase, for as potential increases the double layer acts less as a perfect capacitor and more like a mass transport resistance, with the resistive contribution taking over the capacitive contribution. This is indeed what is observed, confirming the validity of the **R1 + G1 + C2/R2** circuit to model the impedance behaviour of our electrode at low overpotentials. At such low overpotentials, the contribution of the double layer is quite low. Trends for R_{CT} and C_{DL} values are plotted and discussed later in this chapter.

The most interesting element of this circuit is **G1** which represents our catalytic phenomenon. The values of τ_G and R_G, which are potential-independent, are averaged and fixed for further fitting of the data. This ensures coherence between the model and the variables in the fit: those values do not vary with potential and are hence locked. The value of τ_G for the MWNT-COOH/**CyArg** electrode without Nafion or fullerene is averaged at 0.24 s, which gives

a k, or TOF = 4.1 s^{-1}. Of note, this is the intrinsic turnover value of a single catalytic site and hence does not depend on overpotential.[16,121] However, the catalytic activity of an electrode as a whole depends on overpotential because the catalytic sites are not all at the same "electronic distance" from the current collector.[126] This leads to a dispersion in ohmic drop for catalysts placed at different distances from the current collector, triggering slightly different resistances to electron transfer and hence a dispersion in E_{IRcorr} values. This means that, as overpotential increases, more catalytic sites become catalytically active, hence changing the overall current response of the electrode, while within a given electrode all of those sites are doing the same catalytic cycle with the same TOF. The same protocol was applied to the other three types of electrodes, which are MWNT-COOH/**CyArg** with either Nafion (100 wt%), fullerene (12 wt%) or both. Full EIS fit data can be found in the annex to this chapter.

Carbon and ionomer composition	***Average τ_G (s)***	***TOF (s^{-1})***
MWNT-COOH	0.24	4.1
MWNT-COOH + Nafion	0.36	2.8
MWNT-COOH + fullerene	0.26	3.9
MWNT-COOH + fullerene + Nafion	0.36	2.8

Table 4. Average τ_G values and corresponding TOF for the four ink compositions, obtained from the fit of PEIS spectra with a R1 + G1 circuit in the 0 – 50 mV overpotential region. Half-cell setup, 160 µL/cm² loading, S = 0.063 cm², electrolyte is H_2SO_4 0.5 M in H_2O, pH 0.3, 298K and P_{H2} = 1 atm.

The value of TOF is the same for the MWNT-COOH/**CyArg** and MWNT-COOH/**CyArg** with fullerene electrodes (see Table 4), indicating that fullerene addition has no effect on the catalytic cycle. However, the addition of Nafion in both cases leads to a decrease of the TOF by 25 %, from about 4 to around 3 s^{-1}. While the order of magnitude of the TOF remains the same, we think this could be a non-negligible difference which could be correlated to an effect of Nafion on the catalytic cycle of the catalyst. It is possible that the formation of strong H-bonds between the outer coordination sphere of the catalyst and the hydrophilic part of Nafion could trigger a lower flexibility of the pendent base, lowering the intrinsic TOF of the catalyst.

Interestingly, these values are close to those found in the initial report of a grafted **CyEster** DuBois catalyst by our group, which found a TOF around 2 s^{-1}.[81] These TOF values for grafted **CyArg** in different environments can also be compared to that of two grafted hydrogenase enzymes, determined recently through EIS by the group of Armstrong.[17] In this work, TOF values for HOR at 0°C of 78 s^{-1} and 12 s^{-1} are found for *Cp*I from *Clostridium pasteurianum* and *Cr*HydA1 from *Chlamydomonas reinhardtii*, respectively. These values may seem quite low for hydrogenase enzymes, which turn over much faster in solution, of the order of several

hundred or thousand s^{-1}.[109,128,129] However, the same is true for **CyArg**: in solution at 25°C, 1 atm H_2 and pH 0.4, TOF for HOR in water was found to be around 210 s^{-1}.[52,82] It is interesting to draw a parallel between the activity loss of those biological and bio-inspired systems when going from homogeneous to grafted catalysis, especially given that it may arise from similar phenomena. Dynamic, flexible reorganization of the hydrogenase enzyme is one of the necessary factors for good catalytic activity, and so is the flexibility of the second coordination sphere of DuBois catalysts.[13,45,46,52,130] This kind of flexibility is lost to some extent when those catalysts are grafted onto a surface, possibly somewhat slowing down the catalytic activity.

c. Model for the catalytic plateau

At higher over potentials (above around E_{IRcorr} = + 100 mV, see Figure 4), the behaviour of the electrodes follows two different paths. The two electrodes containing Nafion show a linear I/E response in the continuation to that of the 0 – 50 mV region, while the electrodes without Nafion display catalytic plateaus. It is our hypothesis that those plateaus arise from a limiting diffusion of protons, as discussed in temperature studies earlier in this chapter. This hinders HOR catalysis as the product of the reaction is not removed fast enough from the active site.

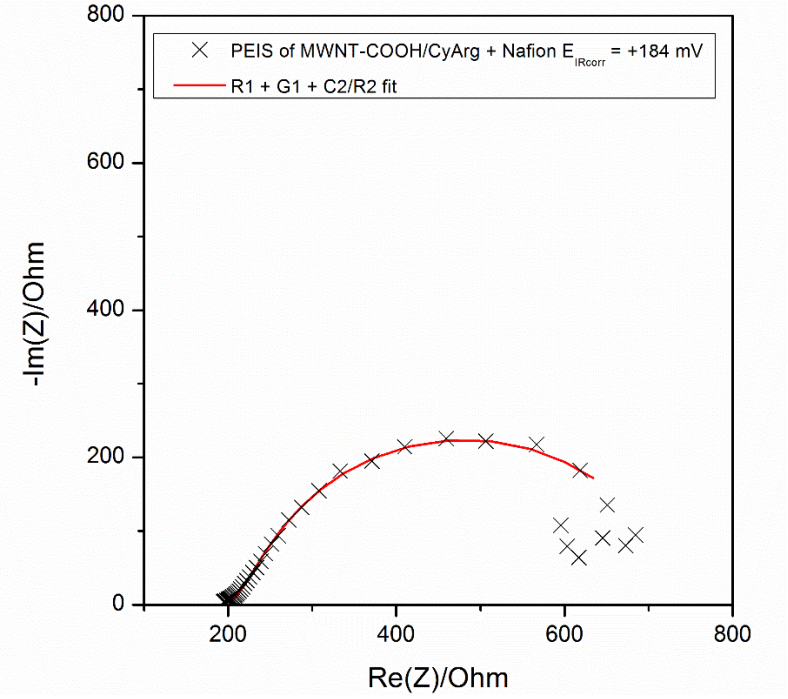

*Figure 11. Nyquist plot of a PEIS spectrum of a MWNT-COOH/**CyArg** electrode with Nafion at E_{IRcorr} = + 184 mV overpotential for HOR, fitted with a R1 + G1 + C2/R2 circuit. Half-cell setup, 160 µL/cm² loading, S = 0.063 cm², electrolyte is H_2SO_4 0.5 M in H_2O, pH 0.3, 298K and P_{H2} = 1 atm.*

EIS spectra for the electrodes containing Nafion can be fitted at all potentials with the **R1 + G1 + C2/R2** equivalent circuit used in the 0 – 50 mV region, without requirement for an

additional circuit element to represent diffusion. This is illustrated in Figure 11 for a MWNT-COOH/**CyArg** electrode with Nafion and no fullerene at a high potential for HOR, E_{IRcorr} = + 184 mV (full fit data for all electrodes can be found in the annex to this chapter). As potential increase, the contribution of the electrochemical double layer to overall impedance increases as it behaves more like a mass transfer resistance and less like a capacitor. There is a small inductance loop at the low-frequency end of the spectrum which is not considered significant and hence was removed from the fit. This is in line with the linear current response over the 0 - 200 mV overpotential range for HOR, and indicates that no other phenomenon than the intrinsic TOF is limiting catalytic activity at a single site.

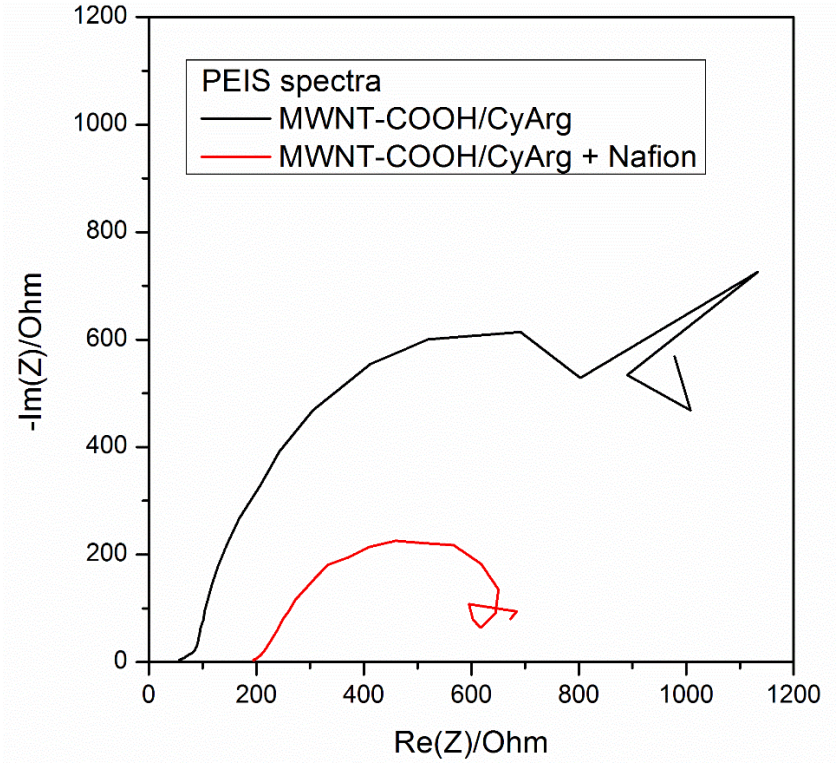

*Figure 12. Nyquist plot of PEIS spectra of MWNT-COOH/**CyArg** electrodes with and without Nafion at E_{IRcorr} = + 184 mV overpotential for HOR. Half-cell setup, 160 µL/cm² loading, S = 0.063 cm², electrolyte is H_2SO_4 0.5 M in H_2O, pH 0.3, 298K and P_{H2} = 1 atm.*

Spectra for the electrodes without Nafion can be fitted with the **R1 + G1 + C2/R2** circuit as well at high overpotentials. However, Figure 12 illustrates the difference between the PEIS spectra of a MWNT-COOH/**CyArg** with and without Nafion at E_{IRcorr} = + 184 mV. A much larger impedance phenomenon is present in the case of the electrode without Nafion, which is coherent with an additional impedance contribution of mass-transport in the catalytic plateau. This is reflected in the fit values of the **C2/R2** circuit element. Of note, the value of R_{cell} is larger in the Nafion-containing electrode (see annex). The values of C_{DL} and R_{CT} are plotted as a function of potential in Figure 13 and Figure 14, respectively.

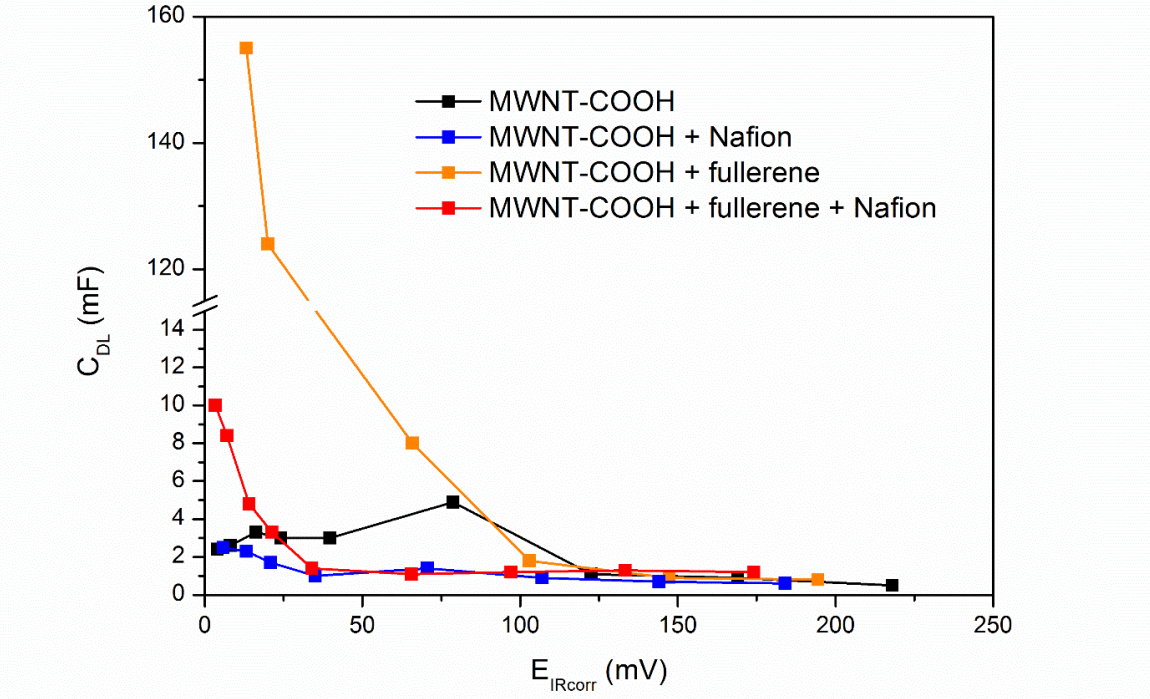

Figure 13. C_{DL} values as a function of potential for all four electrodes. Half-cell setup, 160 µL/cm² loading, S = 0.063 cm², electrolyte is H_2SO_4 0.5 M in H_2O, pH 0.3, 298K and P_{H2} = 1 atm.

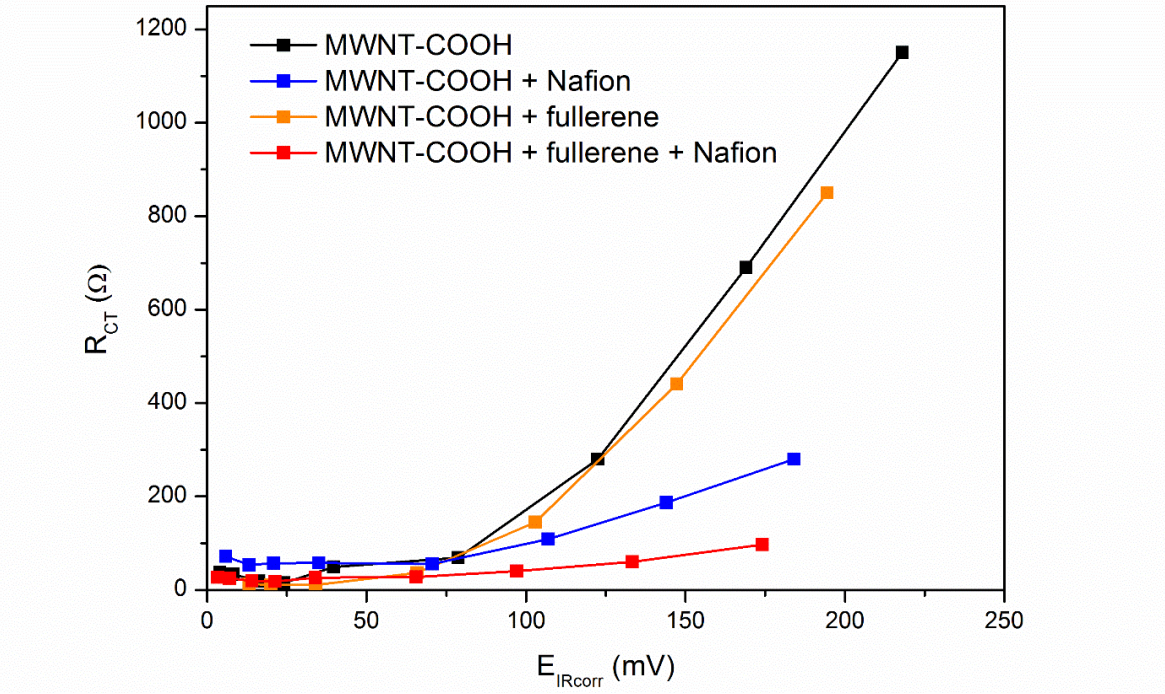

Figure 14. R_{CT} values as a function of potential for all four electrodes. Half-cell setup, 160 µL/cm² loading, S = 0.063 cm², electrolyte is H_2SO_4 0.5 M in H_2O, pH 0.3, 298K and P_{H2} = 1 atm.

It appears from Figure 13 that the addition of fullerene increases the double layer capacitance of the electrodes tremendously at low overpotentials. This is attributed to an increase in hydrophobicity of the electrode. However, values of capacitance stabilize for all four electrodes at a similar value of around C_{DL} = 1 mF at high overpotentials, as the impedance contribution

of the **C2/R2** element becomes mostly resistive. In Figure 14, it appears that initially low values of R_{CT} increase with potential. This is to be expected for ion transport becomes more important as current densities increase and more protons are to be evacuated. Maximum values of R_{CT} are much larger in the case of Nafion-free electrodes. This leads us to think that charge transfer through proton transport is the limiting factor in the absence of ionomer, and plays a much less important role when Nafion is present.

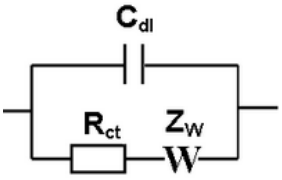

Figure 15. Randles equivalent circuit.

The impedance data for our systems could not be fitted with a Randles circuit, depicted in Figure 15, instead of the **C2/R2** element. In such a circuit, W denotes the Warburg semi-infinite diffusion element which represents diffusion from the bulk electrolyte to the electrode. It is a low-frequency phenomenon and its inability to fit our data constitutes proof that the diffusion limitation observed in the case of catalytic plateaus arises from mass transport through the thickness of the electrode rather than from the bulk electrolyte to the electrode.

5. Conclusion

Kinetic analysis and EIS permit a much better understanding of these molecular-engineered materials. Micro-polarization combined with EIS allowed to determine the intrinsic TOF of the grafted catalysts. These values compare well with the values measured for adsorbed hydrogenases as well as similar catalysts in solution, which bridges the gap between electro-assisted catalysis and molecular electrocatalysis. EIS gives a lot of insight on limiting phenomena for catalysis at different rates and allows us to better understand the limits of our materials, yielding possible paths for improvement. The synergy between Nafion and fullerene has to be further investigated in order to fully understand what is happening in our electrodes. Partial H_2 pressure experiments could be led in conjunction with isotope experiments in order to elucidate gas diffusion mechanisms in such elaborate environments. This synergy was also shown for noble-metal free ORR catalysts as well as Pt-C based catalysts for both HOR and ORR with very promising early results. These finding were the basis of a patent application (INPI n°1854007) which encompasses the use of fullerene in the formulation of catalytic inks for fuel cells and electrolysers.

6. Experimental section

d. CO tolerance

A Pt/C electrode was made by suspending 40% Pt/C (Tanaka) in EtOH (2.77 mg/mL) and drop casting onto a GDL to reach a surface loading of 50 µg/cm². The MWNT-COOH/**CyArg** contained neither Nafion nor fullerene and the ink was deposited as described in Chapter II at a loading of 160 µL/cm². In a classical CA experiment at 100 mV overpotential for HOR, gas flow was switched from pure H_2 gas from an electrolyser to H_2 + 50 ppm CO gas (Air Liquide) at 25°C, 20 mL/min and 1 atm.

e. Temperature study

A classical three-electrode setup is used in a water-jacketed, thermostated electrochemical cell heated at several discreet values between 25 and 65°C. The working electrode is a MWNT-COOH/**CyArg** electrode at a loading of 160 µL/cm². Current densities are noted and plotted against the temperature in a classical Arrhenius plot to determine the activation energy.

f. Electrochemical impedance spectroscopy

General electrochemistry procedures for a three-cell setup as well as described in Chapter I are used, with some considerations specific to EIS. Potentials are quoted and measured against the OCV rather than against the reference electrode. In order to reduce contamination with oxygen to a minimum, the electrochemical cell used had a volume of 3 mL, and the electrolyte was degassed with Ar for 2 hours. The reference electrode used was a miniature Hg/Hg_2SO_4 (Bio-Logic). The parameters shown in Figure 16 were used for data acquisition, with the only variable being the applied potential:

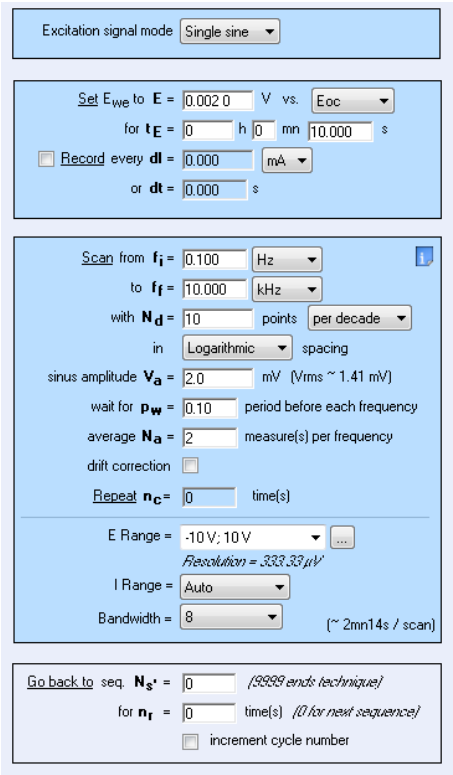

Figure 16. Screenshot of the parameters used for EIS data acquisition in EC-Lab v11.17

Several precautions and verification steps were employed to ensure that measured data and model were realistically representing the observed phenomena:

- Potentials were corrected for ohmic drop using the following equation:

$$E_{IRcorr} = E_{applied} - iR$$

  Using i in mA the current at a given $E_{applied}$ and R_{cell} the resistance of the setup
- The current densities for each EIS spectrum were plotted against the data obtained in CVs to ensure that the system was in a pseudo-stationary state
- No circuit element was added unless it both represented a supposedly existing phenomenon and lowered the X^2 by a factor of 10, following an Occam's razor of sorts
- The EIS spectra were fitted with simulations of the circuit using the Z_{fit} function of EC-Lab in order to verify that each component of the circuit was significant in the fit
- The evolution of the various parameters of the models were plotted a function of overpotential in order to ensure that the models were valid

Chapter IV – Integration in PEMFCs

With a now much better knowledge about the physical chemistry of our most performing systems came the time for their integration in functional devices. The goal of this part of the project is to make an entirely noble-metal free operational fuel cell and showcase the viability of implementation of cheap, abundant metal-based catalysts in final devices. For this, we employed at the cathode the CoNC catalysts introduced in Chapter III which are described in further detail here.[72,131,132] Here, we show how important some technological aspects are when benchmarking new catalysts. We hope to convince the reader that those aspects should not be overlooked: a better catalyst could pale in comparison to a worse one merely because the benchmarking apparatus and assembly process were not chosen properly.

1. Benchmarking apparatus

The first step was to get access to a fuel cell benchmarking setup for full devices. For that purpose, and with the help of Dr Adina Morozan, a standard benchmarking system was built in house, with a fuel cell enclave connected to heating cartridges, and gas inlets which allow control over heating and humidification of gases. As discussed later in this chapter, gas humidification is an important technological factor that was probably slightly overlooked while designing this benchmarking setup. A fuel cell enclave allowing electrode surfaces up to 5 cm^2 with serpentine gas channels was purchased from Paxitech. Figure 1 presents the initial drawing of the fuel cell benchmarking apparatus built in-house, with the following characteristics:

- H_2 and O_2 gas inlets, allowing flow up to 80 ml/min
- Possibility to switch from O_2 to air from a membrane pump
- Humidification of the gases with heated bubblers
- Pressure control for both gases up to 3 atm
- Heating of the cell up to 150°C with heat controllers

H_2 is provided by an electrolyser, which can provide up to 300 mL/min of 99.99% H_2 at 4.6 bar. O_2 is provided from a pressurized bottle and air with a simple aquarium membrane pump, with the drawback being that air pressure cannot be increased above 1 atm. However, this is comparable to a type of fuel cell termed "passive air flow fuel cells" which are simply left open to natural air convection, which is sometimes assisted by fans.

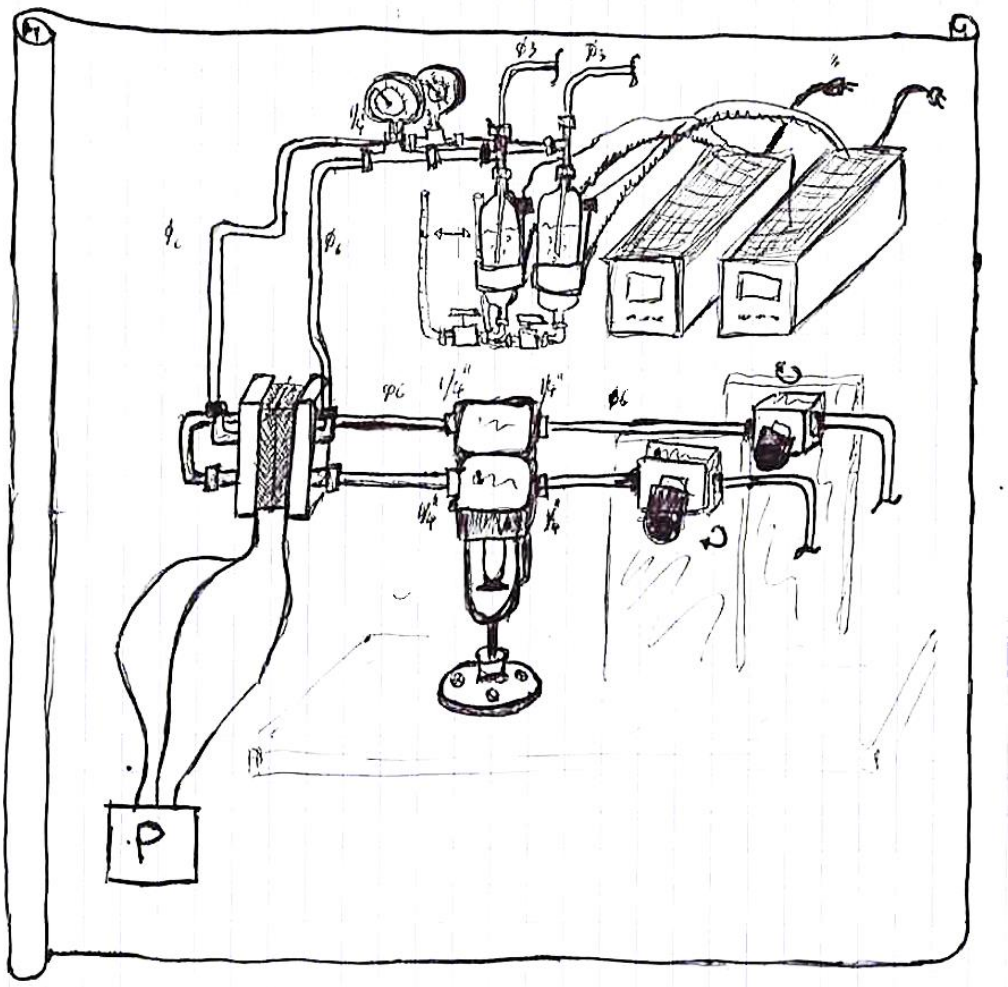

Figure 1. Initial drawing of the fuel cell benchmarking apparatus. P is a potentiostat.

Later conversations with fuel cell specialists taught us that the maximum gas flow rate in our systems was not sufficient to ensure homogeneous repartition of substrates over all of the 5 cm^2 electrodes and, in the continuation of this work, future improvement in design should bring gas flows up to at least 200 mL/min. However, while inhomogeneous substrate distribution can lead to localized fuel starvation, especially problematic on the cathode side,[133] we are quite confident in asserting that it did not hinder the performances of our fuel cells especially at our quite low current densities compared to those of Pt fuel cells. It is our understanding that inhomogeneous fuel distribution causes problems either in the longer term or at high current densities, none of which apply (for now) to our systems. This is supported by the fact that our fuel cells show identical power outputs whether the cathode is fed with pure O_2 or air.

2. Activity markers of a fuel cell

The fuel cell is benchmarked as a two electrode electrochemical cell, in which the cathode serves both as reference and counter electrode. Hence, in the case of a chronoamperometry (CA) measurement for instance, instead of applying a potential to the working electrode quoted versus a reference electrode, it is rather a difference of potential, noted E, applied between the two electrodes.

The current passing through the anode and cathode has to be the same, hence this sets E and hence the overpotentials for the HOR and ORR at the anode and cathode, respectively. Hence, the limiting electrode will always limit the power output of the cell no matter how well the other electrode performs.

a. Open circuit voltage

The open circuit voltage (OCV) represents the difference in potential between the two electrodes of the fuel cell in the presence of H_2 at the anode and O_2 at the cathode, at null current densities. For an ideal fuel cell with imaginary "perfect" catalysts that have no overpotential requirements for HOR or ORR, the ideal OCV is the difference between the standard potentials of HOR and ORR, which at pH 0 for a PEMFC gives:

$$OCV_{ideal} = E^0_{ORR} - E^0_{HOR} = 1.23\ V\ at\ 25°C$$

As a general rule, the OCV is given for a PEMFC by the following equation:

$$OCV = 1.23 - (\eta_{HOR} + \eta_{ORR})\ V$$

For platinum/platinum (Pt/Pt) fuel cells in which the catalyst has no overpotential for HOR and requires but a few hundreds of millivolts for ORR, the best observed OCVs fall in the 950 mV region. In which η is the overpotential requirement in V of the catalysts for the HOR and ORR, respectively. The onset potential of a catalyst is a controversial activity marker that is difficult to measure and define. However, as Pt is a fully reversible catalyst for HOR/HER without requirement for overpotential in either direction, the difference between the OCV of a Pt/Pt fuel cell and its ideal value is mostly due to a overpotential requirement for ORR. The lower the overpotential requirements are and hence the closer the OCV gets to its ideal value, the better the fuel cell can be expected to perform in terms of electromotive force. In the case of our systems, as we are not changing the catalyst, OCV from one fuel cell to the next should remain the same, regardless of any differences in Nafion membrane, assembly or SL. An OCV of about

830 mV can be expected, given that the ORR at the CoNC cathode requires 400 mV overpotential and the HOR at the anode, no overpotential at all. In reality, the OCV is repeatedly observed at 790 ± 10 mV. While the 10 mV variation is deemed within acceptable experimental error, the 40 mV difference is attributed to a voltage loss from junction overpotentials at the interfaces between the catalytic layers and membrane.

b. Power output

Power output is the most relevant metric when describing systems for "real-world" applications, as this is what defines the possible applications of a fuel cell stack. At a given E, the power output of the fuel cell, P, is given by the following equation:

$$P = E \times i,$$

with:

$$E = E_{cathode} - E_{anode} - iR$$

In which P is in W, E in V, i the current in A and R the internal resistance of the cell in Ω. The iR product is the so-called "ohmic drop" of the cell, a contribution from the internal resistance of the fuel cell that decreases its voltage as a function of the passed current.

As E is decreased, *i* increases because the reactions on anode and cathode each benefit of a higher overpotential, or driving force. A local maximum of P is found, P_{max}, the maximum power output of the PEMFC, which corresponds to a pair of E and i values.

3. Technological considerations

a. Water management

Water management in a fuel cell is a very sensitive parameter that can make or break a system just as well as the choice of a catalyst. Let us take a first look at classical Pt/Pt fuel cells. The water content of the fuel cell has to be very finely tuned, as a lack of water will prevent efficient proton transfer through the membrane and too much water will lead to flooding of the electrodes, preventing gas diffusion. This is a very simple first look at this problem but the actual behaviour of water in the fuel cell is multifaceted and complex. First of all, water is present in both gaseous and liquid forms. The presence of nucleation sites can trigger the formation of water droplets, often in bothersome places such as the serpentine gas channels or within the pores of the GDL and catalytic layer, causing problematic inhomogeneous gas

repartition.[133] Second, water vapour is constantly being synthesized at the cathode, where water is undesirable as it prevents gas diffusion. As a general rule, a better repartition of water between the anode and cathode is desirable. Studies propose the use of a small temperature gradient to promote water migration from the cathode to the anode: heating the cathode by a few more degrees than the anode has been shown to efficiently serve this purpose.[134]

In the case of our noble metal-free fuel cells, several factors change. Arguably, the most important one is that the current densities of noble metal-free fuel cells are, as of yet, nowhere near those of a Pt/Pt fuel cell. Catalytic activity at such low current densities creates negligible amounts of water at the cathode and almost no perceptible increase in overall temperature of the system. The water formed *in situ* at the cathode in Pt/Pt fuel cells is critical to the proper hydration of the membrane (see Conditioning below). In our fuel cells, this water has to be provided by other means, a problem that comes hand in hand with that of operating temperature, described hereafter.

b. Operating temperature

Classical operating temperature for a Pt/Pt fuel cell is in the 60-90°C range.[135,136] Lower temperatures entail slower catalysis and higher temperatures are detrimental to membrane and ionomer hydration and, as water transitions to the gas phase, proton transport is at best hindered and at worst non-existent.

A concern when considering molecular catalysts is their thermal resistance : molecules are overall much more prone to thermal degradation than inorganic metallic nanoparticles. The main concern when considering the operating temperature was hence the stability of the molecular anode catalyst. At the cathode, the thermal stability of the CoNC cathode catalyst under turnover has been well established.[131,132] Phosphorus NMR studies of **CyEster** and **CyPy** have proven that they retained their molecular structure in 0.5 M sulfuric acid solution at 80°C over 24 hours, under an atmosphere of Ar. However, this was not assessed under catalytic conditions. **CyArg** has been proven to remain stable, in solution and under HOR turnover conditions, up to 72°C.[13,52] However, experiments in this work indicated that the noble metal-free fuel cells prepared in this project showed much less power output at 55°C than at 25°C. In fact, they displayed a decrease in activity over increasing the temperature, the opposite of what was expected from the Arrhenius activation energy calculations in Chapter III. This, taken in consideration along with the established stability of **CyArg** and CoNC under turnover at this temperature leads us to hypothesize that heat does not degrade the catalyst, but rather impacts,

to a yet not fully understood extent, the nano-structure of the electrode or causes critical dehydration of the membrane or catalytic layer and subsequent loss of proton transport. As the temperature increases in Pt/Pt fuel cells, the hydration of the membrane relies more and more heavily on *in situ* water synthesis and less on the humidification of gases. This may be where some problems lie for our noble metal-free fuel cells, in which almost no water is formed *in situ*. In future work, assays should be led with a polybenzimidazole membrane doped with phosphoric acid, which could retain better H^+ transport properties in dry conditions.

c. Conditioning

Classical Pt/Pt fuel cells are submitted to a so-called conditioning treatment, in which the potential or current is ramped stepwise in order to increase the power output with each step. The fuel cell is maintained at each step for a certain amount of time that can range from a couple of minutes to several hours. The effect of this conditioning is beneficial to the power output of the fuel cell. The reasons for this improvement are multiple and not yet fully understood but it is thought to be due to proper, incremental hydration of the fuel cell and slow reorganization of the Nafion ionomer within the catalytic layers, rendering more catalytic sites accessible to substrate and electrolyte.[136] This is termed a "break-in" period, or activation period.

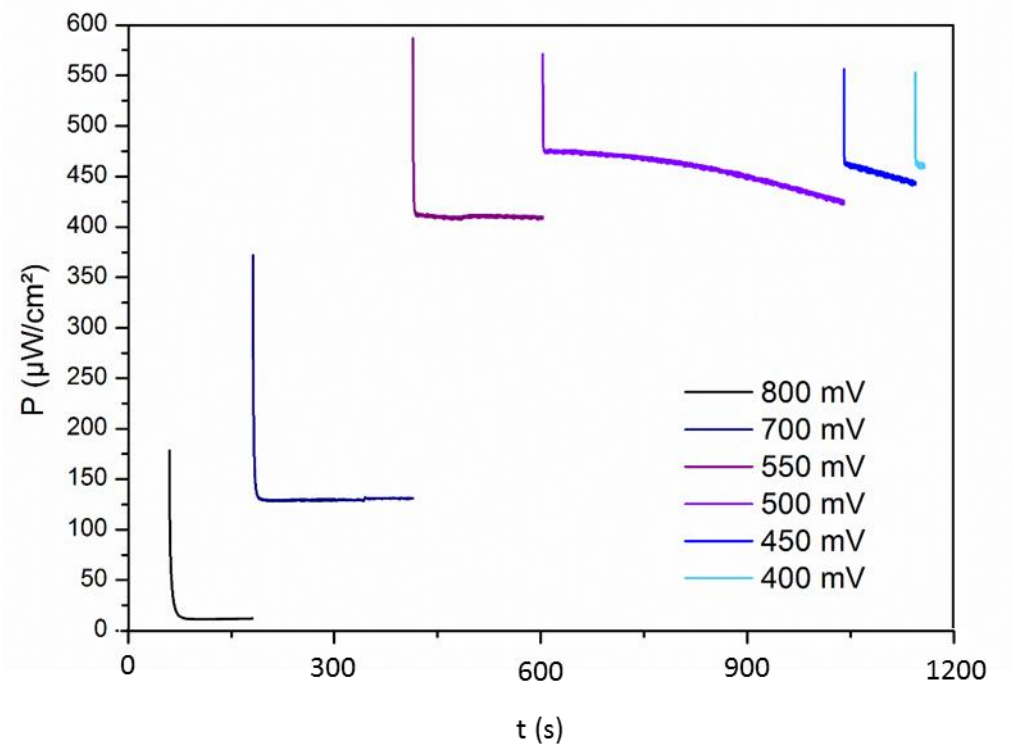

*Figure 2. Stepwise CA conditioning of a compact **CyArg**/Nafion/CoNC fuel cell. $P_{H2} = P_{O2} = 1$ atm, RT, S = 1.5 cm²*

In the case of our noble metal-free PEMFCs, this conditioning has proven detrimental to overall power output. Indeed, as shown in Figure 2, when E is decreased from 800 to 400 mV, power output increases with each step but as the potentials are maintained over several minutes the power output diminishes. Possible explanations for such decrease in currents are proposed below.

4. Membrane-electrode assembly

In this part we'll go over the different components of the MEA and the process of their assembly. The MEA consists of the anode and cathode, separated by a proton-exchange membrane. They are pressed together in order to establish intimate contact between the electrodes and the membrane while retaining electronic insulation between the two electrodes in order to avoid short circuits. This is one of several challenges in the elaboration of the MEA, the longevity and efficiency of which depend on many mechanical, chemical and topological parameters. First we describe the electrodes and membrane and their important characteristics, then go over the process of assembling them in the making of the MEA.

a. Anode

Following the results of the three previous chapters, our best-performing anode formulation was chosen for integration in the fuel cell. This ink contained MWNT-COOH, with 10 % fullerene, 100 % Nafion and 66 % **CyArg**, all in mass ratios compared to the MWNT-COOH. It was deposited at 320 µL/cm² onto a Paxitech GDL without MPL, and air-dried.

b. Membrane

A commercial Nafion membrane of 25 µm thickness from Sigma-Aldrich was chosen. Reports show that thinner membranes lead to better performance of fuel cells, [89,90,112,137] and 25 µm was the thinnest commercially available membrane at the time. For this work, several membranes with thicknesses between 25 and 200 µm were tested and the thinner membranes reproducibly yielded the best current densities. However, as thinner membranes are used, additional precautions must be taken while making the MEA: thinner membranes are fragile and prone to tearing and other types of mechanical failure. Too rough an electrode surface can cause tremendous localized stress on the membrane, which in turn can result in short circuits and hence non-functional MEAs. A single rigid carbon nanotube sticking out of the surface by a couple of microns can be enough to puncture a thin membrane.

Following a report in literature for Pt/Pt fuel cells,[137] an attempt was made at getting rid of the preformed Nafion membrane altogether by direct deposition of large amounts Nafion ionomer onto both electrodes. In this configuration, Nafion ionomer was drop-casted with a pipette onto both electrodes which were then sandwiched around a square gasket of known surface area. The gasket serves both as a gas barrier to prevent gas crossover, and to prevent short circuits on the side of the GDLs. If properly deposited, the layer of Nafion ionomer atop the electrodes will be insulating enough to prevent short-circuits once dried. However despite several attempts, no MEA with a correct OCV could be obtained and they all displayed very little resistance between the anode and cathode (R = 3 Ω), indicative of a short-circuit.

c. Cathode

The goal of this project was ultimately to build a PEMFC without any Pt, which means that an alternative catalyst had to be used for the cathode as well. As mentioned in the general introduction, most of the research on Pt-free catalysts is aimed at catalysts for ORR and hence the alternatives are numerous.[18,99,114] Previous work in our group in collaboration with Bruno Jousselme at CEA Saclay employ so-called transition metals nitrogen-doped carbon (TMNC) catalytic materials,[72] in which TM is, in this work, cobalt. Hence, the material is termed CoNC. Those materials are made through pyrolysis of nitrogen-containing precursors and TM salts onto carbon materials such as carbon black or carbon nanotubes, yielding porphyrin-type complexations of the TM. Porphyrins are a very stable motif found in nature, for instance in the cytochrome c oxidase enzyme, which contains an iron porphyrin, or heme, at the active site and catalyses the 4 e^- conversion of O_2 to H_2O in living organisms.

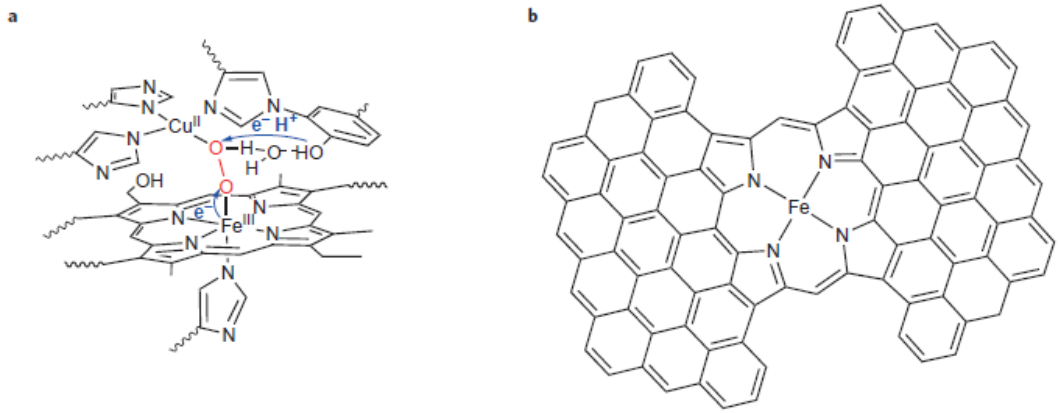

Figure 3. Taken from ref[114] with permission. of metallo-porphyrin-based ORR catalysts. a, The active site of cytochrome c oxidase with a bound peroxo ligand (red) after 2-electronreduction of O_2 by the initial Fe^{II} and Cu^{I} centres. Further electron and proton transfers to complete the 4-electron reduction process are shown in blue. b, The active site of TMNC ORR catalysts.[138]

Those materials are stable under acidic, technologically relevant conditions and show much promise as replacements for Pt in PEMFCs. Figure 3 shows the structure of the active site of a cytochrome c oxidase compared to the active site of a FeNC catalytic material.

While those catalysts have numerous advantages, they also require a relatively high overpotential to start catalysing the ORR, around 400 mV at pH 0, an evident drawback to possible applications. However, the molecular nature of the catalyst means that slight tuning of the coordination sphere of the metal could lead to improvements in overpotential requirements.[18] This is one of the notable advantages of coordination chemistry.

The CoNC material was dispersed in EtOH in the presence of Nafion, and deposited at a loading of 4 mg/cm², following previously established procedures.[11,72,131]

d. Assembly of the MEA

In state of the art industrial processes, two MEA-making processes exist in which the catalytic inks are deposited either onto the membrane, or onto the GDLs. They are termed spray-coating and hot pressing, respectively. The former method is much more easily scalable than the latter, and more reproducible at a large scale as well. However, spray-coating requires both specific equipment and technical knowledge in order to be done properly. A compact fuel cell was built with the non-noble metal-based catalytic materials described above, using the spray-coating technique. While a correct OCV value (around 780 mV) was obtained, as well as a canonical polarization curve, the power output was very weak, of the order of 28 µW/cm². This is very comparable to previous results obtained in our group in 2015 for a spray-coated fuel cell based on **CyPy** at the anode.[72] Due to lack of time, we did not explore further the optimization of spray-coated fuel cells. However, this is an encouraging proof of concept which shows the feasibility of such a technique for non-traditional catalytic inks, an encouraging step for industrial adoption of such materials.

Instead of spray-coating, we prepared our anodes and cathodes by drop casting of the catalytic inks onto the GDLs, followed by pressing of the GDLs on each side of a hydrated Nafion membrane, as described in Chapter I and using the pressing apparatus described in Chapter II. This enabled us to use the characterization in half-cell studies to understand the behaviour of whole cells by minimizing the number of variable parameters between the half-cell and whole-cell experiments. Several important aspects have to be considered in addition to the assembly time, temperature and pressure.

First, to ensure that the GDLs in the MEA will not be flattened, each electrode is laid within an incompressible mask of a thickness equal to 85 % of that of the electrode. This ensures that no matter what amount of pressure was used, the electrodes would not be compressed by more than 15 %. Over-compression of the GDL can lead to numerous problems, such as perforation of the Nafion membrane or loss of porosity.

Second, in order to prevent the water management issues described above, the Nafion membrane is kept in water right up until it is ready for assembly, at which point it is only superficially dried with a lint-free cloth. As soon as assembly is completed, the MEA is taken out of the 80°C pressing bronze plates and cooled in air.

5. Performances

In this part, we describe a model for calculating a theoretical power output from the anode and cathode performances, present our best performing PEMFCs, and propose hypotheses for the limitation of power outputs.

a. Expected power output

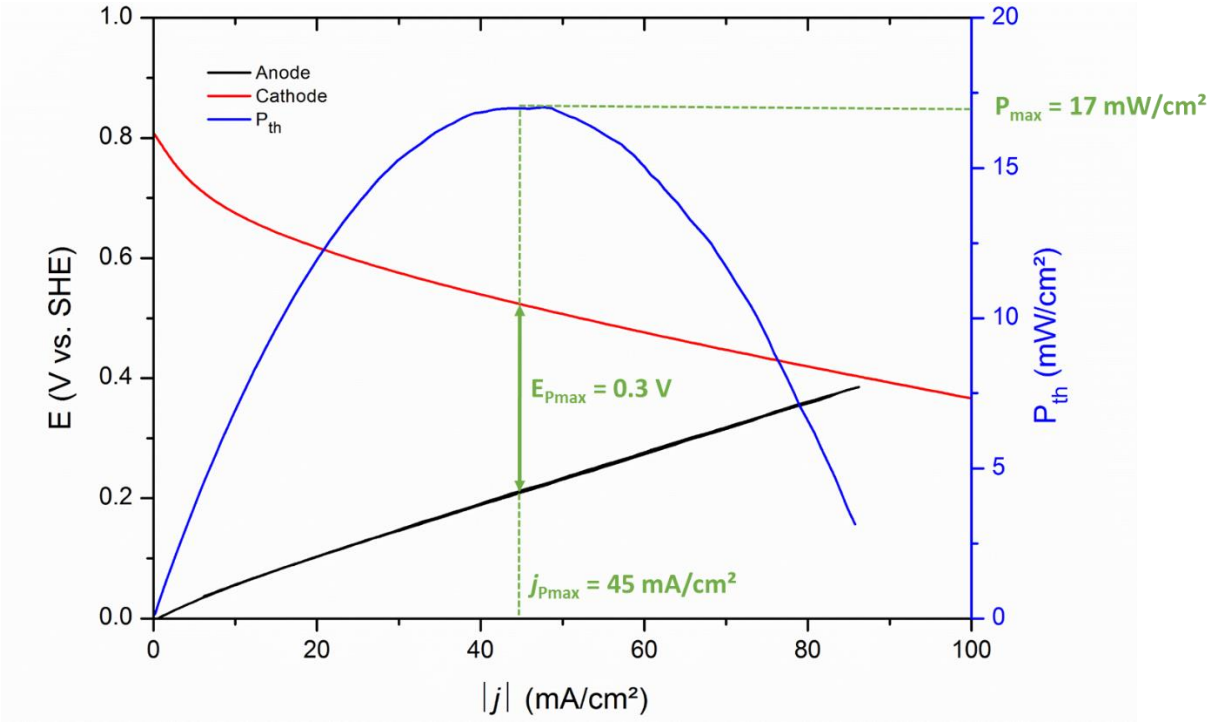

*Figure 4. Polarization curves of a **CyArg** anode (black) and CoNC cathode (red), and extrapolated power output of an ideal fuel cell. Conditions for anode (MWNT-COOH/**CyArg**): S = 0.063 cm², electrolyte is H_2SO_4 0.5 M in H_2O, pH 0.3, 298K and P_{H2} = 1 atm. Conditions for cathode: S = 0.063 cm², electrolyte is H_2SO_4 0.5 M in H_2O, pH 0.3, 298K and P_{O2} = 1 atm.*

A model was made in order to calculate an "ideal" power output, independent of the technical considerations of MEA assembly and water management within the fuel cell. Polarization curves of both the anode (MWNT-COOH/**CyArg**) and cathode (CoNC) were recorded in classical half-cell conditions, and a theoretical power output was extrapolated from these experiments. In Figure 4, the black and red polarization curves are to be read with the black axes and the blue, theoretical power output, with the black abscissa and the blue ordinate. The black and red curves are CV polarization curves as presented throughout this work, quoted against the SHE. The thermodynamic potential of the ORR is at 1.23 V vs SHE at this pH, and it is apparent that the CoNC catalyst requires around 400 mV of overpotential to start turning over, whereas **CyArg** requires no overpotential for HOR, as described earlier. The blue curve, on the other hand, (top and right axes) represents a theoretical power output as a function of E, determined by correlating P and *j* through the following formula:

$$P(j) = j \times |E_{anode}(j) - E_{cathode}(j)|$$

Using this formula, the anode is still found to be limiting at all values of E. It reads P_{max} = 17 mW/cm² at E_{Pmax} = 0.3 V and j_{Pmax} = 45 mA/cm². A larger P_{max} could be obtained if the cathode required less overpotential.

b. Performances of compact PEMFCs

A compact PEMFC is a technologically relevant fuel cell in which the MEA is compact (thickness < 500µm) and hence stackable. Compact MEAs were prepared as described above, using the pressing conditions determined in Chapter II: 1 T/cm² of applied pressure, at 80°C, for 60 seconds, using the anode and cathode prepared as described in the previous section.

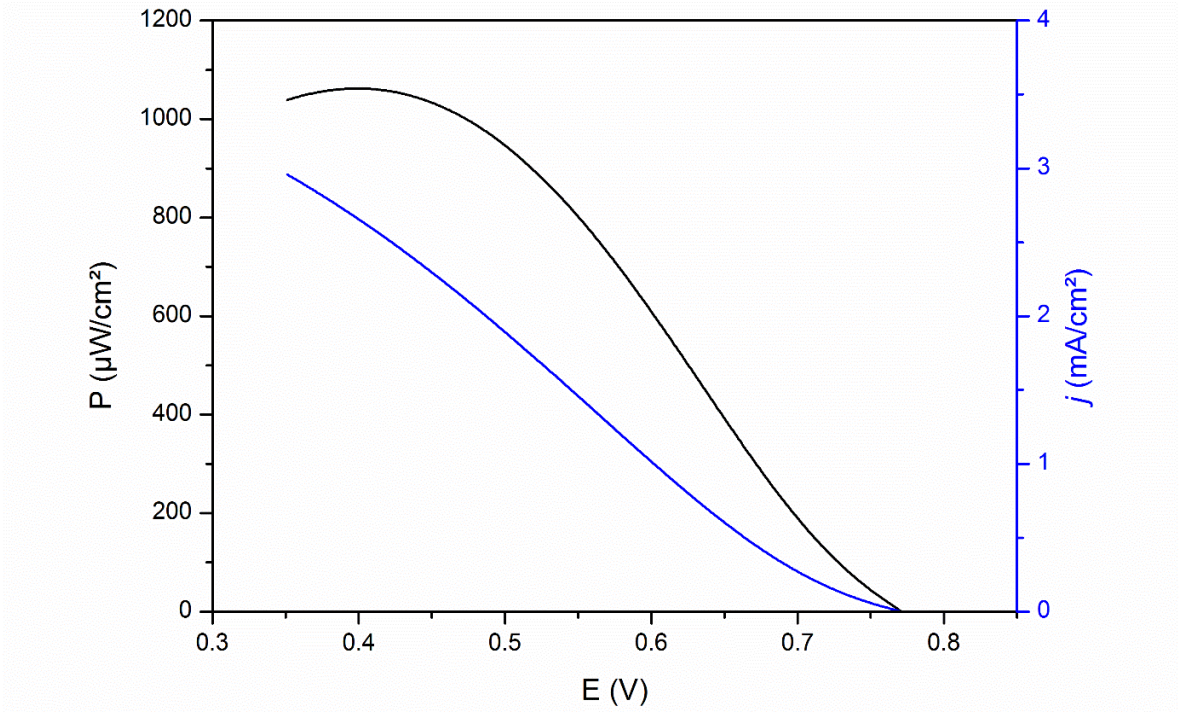

*Figure 5. Black: Polarization curve of a **CyArg**/Nafion/CoNC fuel cell. Blue: corresponding current densities. $P_{H2} = P_{O2} = 1$ atm, RT, S = 2 cm²*

At room temperature, under 1 atm of H_2 at the anode and 1 atm of O_2 at the cathode, with gas flows of 40 and 20 mL/min respectively and gases bubbling through 60°C MilliQ water, the best performing fuel cell obtained with those assembly parameters yielded a P_{max} = 1 mW/cm² at E = 0.4 V, as depicted in Figure 5. The bell shape appearing at E values from 0.425 V to 0.350 V is characteristic of mass-transport limitation, which we attribute to proton mass transport. Interestingly, no difference in performance was observed when the cathode fuel was changed from pure O_2 to air. This confirms the prediction from the model above and leads us to think that, even though the performances of the anode have been greatly improved during this project, it is still the limiting electrode. This performance is quite good, however it is much less than can be expected from the standalone benchmarking of the anode and cathode in half-cell experiments.

c. Performance with liquid electrolyte junction

The model presented in part a. was tested with a simple experiment in which the Nafion membrane of a 5cm² **CyArg**/CoNC fuel cell was replaced by a 10 mm-thick Teflon chamber filled with the electrolyte used in half-cell experiments, H_2SO_4 at 0.5 M in H_2O (see Figure 6).

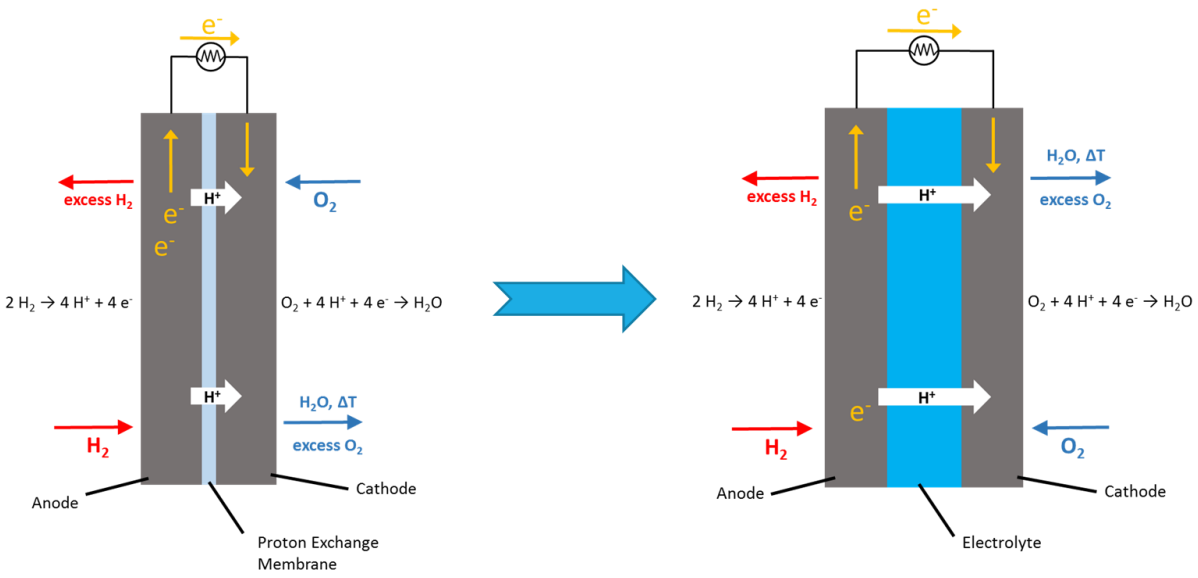

Figure 6. Scheme of the Nafion and liquid electrolyte junction for PEMFCs.

With this experiment, variables inherent to MEA assembly and compact fuel cell operation such as water management were removed. Using the same electrodes and experimental conditions as for the **CyArg**/CoNC compact fuel cell, a P_{max} of 15 mW/cm² was obtained, as shown in Figure 7. This is within experimental error identical to the 17 mW/cm² predicted from the model presented earlier.

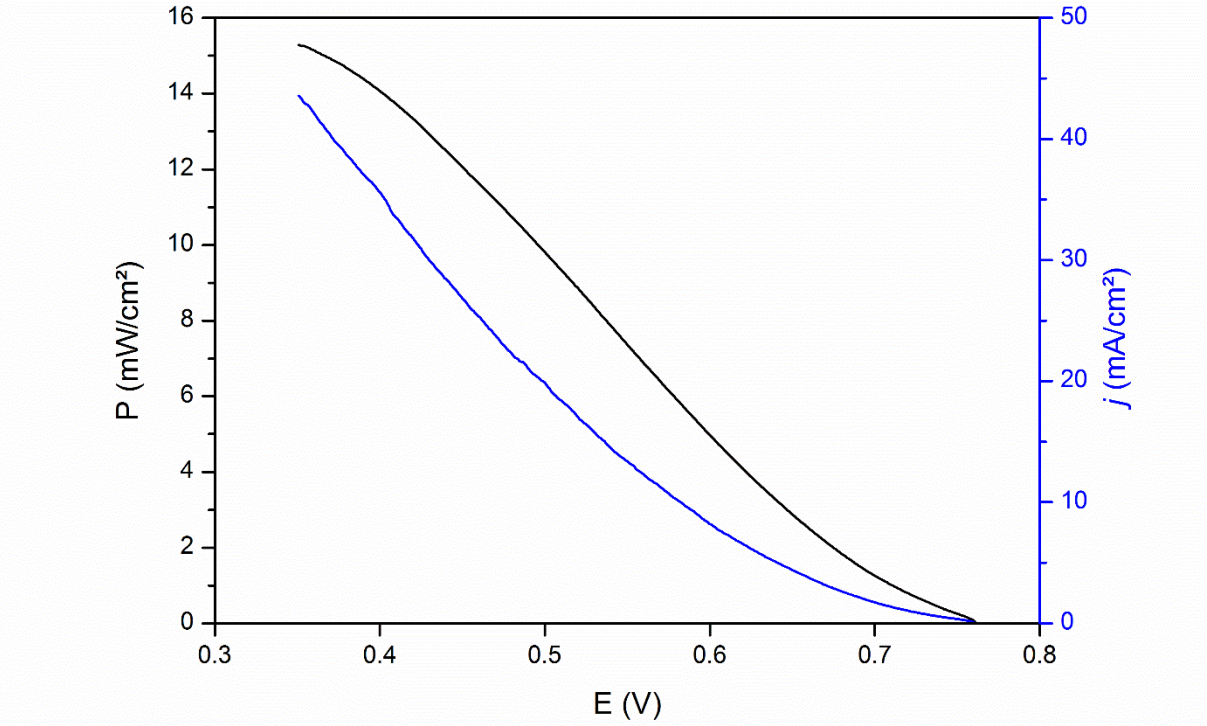

*Figure 7. Black: Polarization curve of a **CyArg**/H_2SO_4/CoNC fuel cell. Blue: corresponding current densities. $P_{H2} = P_{O2} = 1$ atm, RT, S = 5 cm²*

Here, the polarization curves around 0.3 V, also in line with the model presented earlier. The bell shape characteristic of mass-transport is not observed as strongly in this experiment and seems to start at lower overpotentials. Interestingly, the addition of a Nafion membrane on either the anode or cathode did not change this power output significantly, nor does it change the shape of the curve, further proof that the Nafion membrane in and of itself was not hindering the power output.

d. Stability over time and temperature

As previously mentioned in the general introduction, stability is likely the most important factor when considering technological applications. The compact **CyArg**/CoNC PEMFCs present an arguably quite poor stability over time, as well as when temperature is increased.

Time wise, when measuring a CA at 400mV of the compact PEMFC presented in paragraph b, current losses of up to 10 % are observed over ten minutes, with power output dropping from 0.95 to 0.85 mW/cm² (see Figure 8). However, the stability of both the standalone anode and cathode catalysts has been proven, under turnover conditions. Hence, even though the behaviour of the catalyst is expected to change in "dry" compact fuel cell conditions, we are not inclined to think that this loss in current is to be attributed to catalyst degradation.

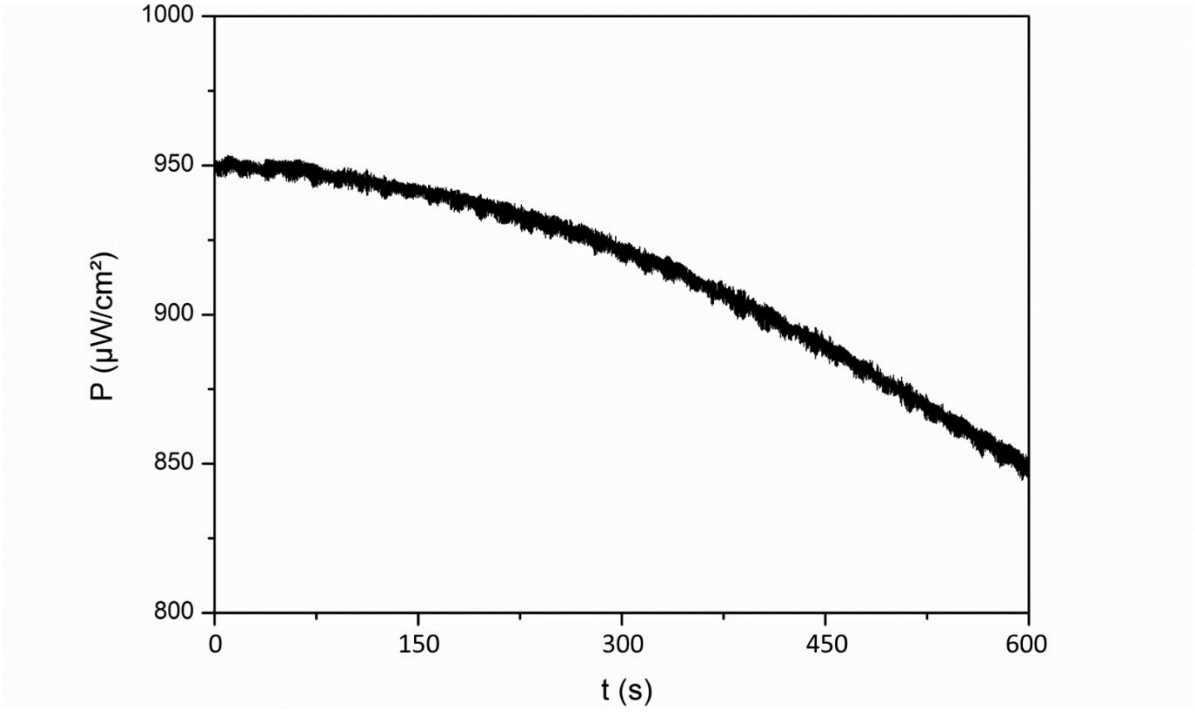

*Figure 8. Chronoamperometry of a compact **CyArg**/Nafion/CoNC PEMFC at 400 mV over 10 minutes. $P_{H2} = P_{O2} = 1$ atm, RT, S = 2 cm²*

When increasing temperature, erratic behaviour is observed above 45°C with current peaking and dropping sharply and no reproducible data could be obtained, while increasing the temperature of the fuel cell to 45°C did not increase activity significantly in the first place.

On the other hand, the liquid electrolyte **CyArg**/CoNC fuel cells described above show good stability at 13 mW/cm² over 2 hours at room temperature in the same conditions as above, with no discernible loss of activity over that period (Figure 9). No experiments have yet been carried on to study the effect of temperature in such a liquid electrolyte configuration.

This pooled information, along with the comparative experiments in which both a liquid electrolyte junction and Nafion membranes are used at the same time, leads us to formulate the hypothesis that the poor stability of our fuel cells over time or increase in temperature increase arises not from a degradation of the catalyst but rather from poor water management within the Nafion membrane. Indeed, as soon as liquid electrolyte is present, PEMFCs are much more reproducible, power output increases and they become much more stable. This hypothesis is also supported by the behaviour of Pt/Pt fuel cells made in the same conditions as the compact noble metal-free PEMFC. In those conditions, the Pt/Pt fuel cells show good stability over several hours at power densities of about 1 W/cm², sufficient to hydrate the membrane in-operando.

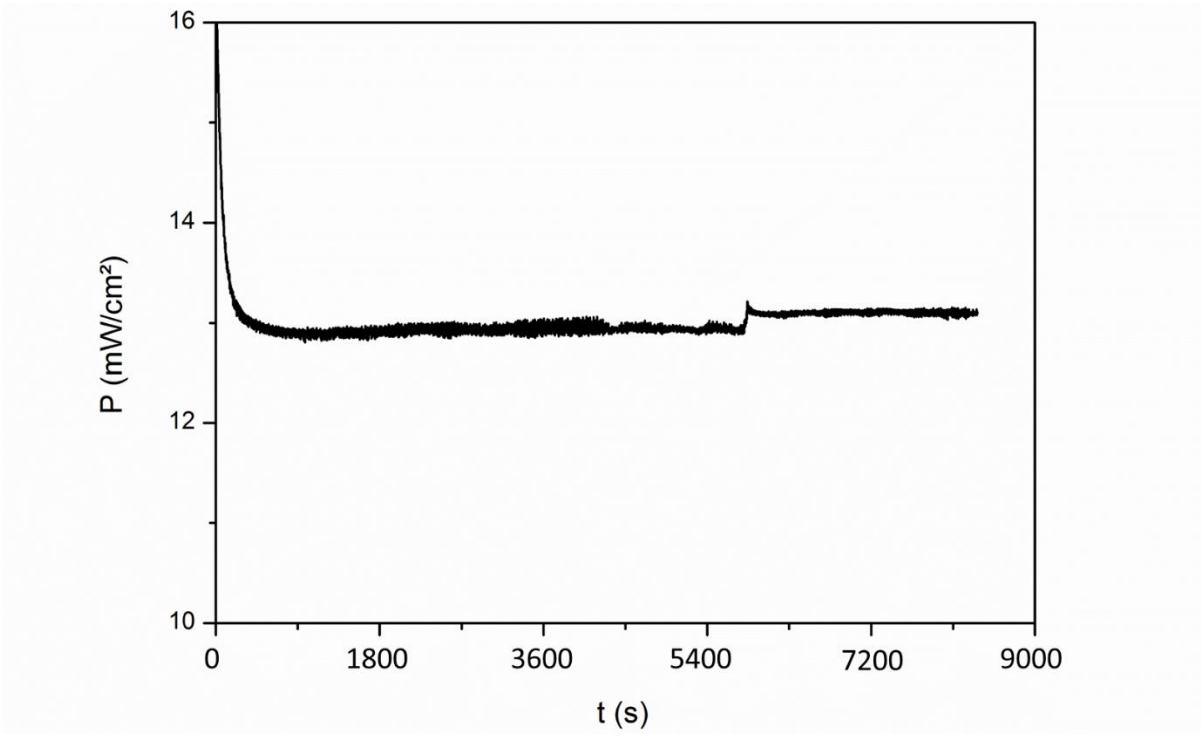

*Figure 9. Chronoamperometry of a liquid electrolyte junction **CyArg**/H_2SO_4/CoNC PEMFC at 400 mV over several hours. $P_{H2} = P_{O2} = 1$ atm, RT, S = 0.063 cm²*

While this is encouraging as to the possible implementation of bio-inspired materials in functional, technologically relevant fuel cells, it shows how important the conditions of benchmarking and environment are when assessing a new catalyst. This was already the message learned from chapters I and II, expanded now not only to the physical environment of the catalyst but also to the technological benchmarking apparatus and some device-level considerations. A lack of expertise on a technological issue can dramatically influence the assessment of the viability of a catalyst.

Another hypothesis could be the crossover of O_2 from the cathode to the anode, where it would react with the reduced form of the **CyArg** complex and inactivate it. Indeed, while **CyArg** is insensitive to oxygen in its resting state, it can be inactivated by exposure of some reduced intermediates to O_2 under turnover conditions.[82] However, we deem the water management hypothesis much more likely, as O_2 crossover would also be expected to happen in liquid electrolyte fuel cells. XAS studies could be led on an anode after catalysis in order to elucidate the oxidation levels of the phosphines of the active site, in order to verify this possibility. A recent report by the group of Pluméré showed that the Ni^0 intermediate of a DuBois complex, which occurs when an electronically insulated complex is presented with H_2, was capable of making H_2O from exposure to H_2 and O_2 and therefore show O_2 resistance, furthermore protecting the catalytically active DuBois complexes from O_2 crossover.[139]

e. Comparison to previous results and state of the art

Table 1 sums up the performance of the best noble metal-free and PEMFCs prepared in this work, in comparison with a Pt/Pt fuel cell made in our lab, the state of the art for PEMFCs with a DuBois catalyst at the anode from our group and a tungsten carbide/Pt fuel cell described in 2009. It has proven quite difficult to find a reference for a state of the art ULL-Pt fuel cell, as the benchmarking values are very different. The performance is rather expressed in mg_{Pt}/kW, the sum of the mass of Pt required at the anode and cathode to reach a power output of 1 kW.

Anode	Cathode	P_{max} (W/cm²)	E_P (mV)	T (°C)	Electrolyte	Year[ref]
CyArg	CoNC	1.10^{-3}	425	25	Nafion 25 µm	This work
CyArg	CoNC	15.10^{-3}	300	25	H_2SO_4 0.5 M	This work
Pt/C 0.5 mg/cm²	Pt/C 0.5 mg/cm²	1,25	300	25	Nafion 25 µm	This work
CyEster	CoNC	23.10^{-6}	350	80	Nafion 25 µm	2015[72]
CyArg	Pt	14.10^{-3}	450	60	Nafion 50 µm	2017[80]
WC	Pt/C	5.10^{-3}	200	25	Nafion 50 µm	2009[24,25]

Table 1. Comparison of the benchmarking values of different PEMFCs. E_P is the potential at which P_{max} is attained.

Our compact noble metal-free fuel cell displays a power output one order of magnitude less than a fuel cell with the same electrodes with an electrolyte junction and three orders of magnitude less than that of a compact Pt/Pt fuel cell with a loading of Pt/C = 0.5 mg/cm² in the same conditions.

The power output of the compact PEMFC prepared in this work is a fifty-fold improvement over the previous noble metal-free cell published by our group in 2015 (P_{max} = 23 µW/cm²).[72] More recently, a compact noble metal-free PEMFC was published by our group with a **CyArg**-based anode and Pt cathode with a power output of 14 mW/cm².[80] However, these results were incoherent with current densities obtained for half-cell experiments, which at the time did not reach more than 20 mA/cm² for HOR regardless of overpotential. Another major difference between our PEMFC and the one previously described is the pre-treatment of the Nafion membrane. In our work, the Nafion membrane was sonicated in H_2O_2, H_2O, H_2SO_4 and then sonicated three times in H_2O for rinsing. In the previous work, it was not sonicated in water at the end, resulting in a membrane doped with H_2SO_4. This was attempted during this work and while initially larger power outputs were reached (up to 4.5 times more power output), the performance was not stable over a few minutes and soon returned to stabilize at the normal value described above. We think that membrane conditioning is critical in the development of the fuel cell but that it can create a false sense of performance by artificially providing protons in an environment that cannot sustain the necessary proton relay by itself in the long term.

6. Conclusion

A model was developed to extrapolate theoretical power densities of a whole cell from the standalone anode and cathode in ideal, electrolyte conditions. Along with this model, a rigorous protocol was followed in order to pinpoint specific issues to specific steps of the process. This enables better troubleshooting and can direct future research efforts. In the case of our systems, water management within the MEA is the main point of weakness of the compact PEMFCs. The benchmarking results of our fuel cells were compared to the state of the art of both Pt and noble metal-free fuel cells. Much effort remains in order to fully understand the technological implications of all the factors described above, however these first results are very encouraging regarding the implementation of molecular, noble metal-free catalysts in fuel cells. Future work should include trying alternative membranes, which employ H_3PO_4 as a proton relay, trying to better control the humidification of the MEA operando and working in collaboration with MEA assembly experts in order to find the best technological conditions for this type of catalysts.

7. Experimental section

a. Benchmarking apparatus & electrochemical measurements

A 2.24 cm x 2.24 cm (5 cm²) active area Paxitech fuel cell enclave with serpentine gas channels and graphite current collectors was connected to gas, heating and potentiostat.

Steel gas tubing (Swagelock) was connected to BronkHorst mass flow controllers able to provide up to 80 mL/min H_2 or O_2 flow rates. The gases were passed through steel bubblers, filled with MilliQ water and fitted with heating sleeves connected to heat controllers (PID, RS Components) able to heat the bubbling water from RT to 100°C. Unless otherwise mentioned, gas flows were 80 mL/min and pressure 1 atm at both the anode and cathode, and the temperature of the bubblers was set at 80°C.

Heating cartridges (PID, RS Components) were connected to the fuel cell and allowed fine (2°C) control over the temperature of the cell as a whole.

Electrochemical measurements in whole-cell setup were performed as a classical two-electrode setup. The anode was the working electrode, and the cathode was both the counter and reference electrode. Electrochemical analysis was performed on a Bio-Logic SP-300 potentiostat and data was processed in Origin 8.5. The fuel cell was degassed with N_2 for 20 minutes prior to purging the anode and cathode with H_2 and O_2 respectively.

b. Membrane-electrode assembly for compact PEMFCs

The anode was a MWNT-COOH/**CyArg** electrode with fullerene and Nafion, prepared as follows: 5.4 mg of MWNT-COOH and 0.6 mg of C_{60} fullerene were dispersed by sonication in 1 mL of abs. EtOH in the presence of Nafion (1:1 Nafion 5 wt%:MWNT-COOH weight ratio). This suspension was mixed in a 3:1 ratio with a 3 mg/mL solution of **CyArg** in pH 6, aqueous, 0.01 M MES:HEPES (1:1) buffer. This ink was deposited at a loading of 320 µL/cm², and air-dried.

The Nafion membrane was pre-conditioned as described in Chapter II and kept in water until the moment when it was assembled in the MEA.

The cathode was prepared as described in previous work.[11,131,132] Co/N/CNT catalyst (20 mg) was dispersed under sonication in a mixture of EtOH:H_2O (3:1) (1.04 ml) in the presence of 5 wt% Nafion solution (160 µl). Before ink drop-casting, the solution was sonicated for 60 minutes. 400 µl of this solution were deposited on the GDL (5 cm^2) substrate and dried at 80°C

under ambient atmosphere leading to a final catalyst loading of around 1333 µg/cm^2. The drop-casting was repeated twice to get a final loading of 4 mg/cm^2.

The MEA was made by pressing the anode, Nafion membrane and cathode altogether, as follows: square 5 cm^2 sections of anode and cathode (about 2.2 x 2.2 cm) were cut with a sharp scalpel blade. The thickness of each electrode was measured and the electrodes were set in square, incompressible masks (Nylon-reinforced PEEK, RS Components) slightly larger than the electrodes (inner section of 2.3 x 2.3 cm). The thickness of the mask was chosen to be equal to 85 % of that of the electrode in order to allow for 15 % compression of the GDL. The electrodes were set on either side of a pre-conditioned square section of Nafion membrane (3 x 3 cm), with the catalytic layer facing the Nafion. This uncompressed assembly was laid between two layers of aluminium foil and placed between two bronze plates heated at 80°C, then the assembly is pressed together for 60 seconds in the modified IR press described in Chapter II. As soon as pressing was finished, the MEA was removed from the bronze plates and waved in air for cooling. The MEA was then put in the fuel cell enclave, along with PTFE gaskets on both electrodes, each gasket half the thickness of the whole MEA. The fuel cell was then closed with 2 N.m torque applied on the bolts with a dynamometric wrench.

c. Spray-coated compact PEMFC

A pre-conditioned 5 x 5 cm, 25µm thick Nafion membrane (Nafion 212, Sigma-Aldrich) was laid flat onto a glass plate heated at 120°C on a laboratory heat plate. Kapton tape was used to mask the outside border of the Nafion membrane, to yield a centred square of 5 cm². To make the anode, an argon spray gun was used to spray MWNT-COOH/**CyArg** catalytic ink to yield a surface loading of 160 µL/cm², over 10 layers. The anode was air-dried and the procedure was repeated for the cathode, this time spraying CoNC in order to obtain a loading in catalyst of 2 mg/cm², over 10 layers, followed by air-drying. The obtained MEA was then sandwiched between two GDLs of 5 cm^2 and set in the fuel cell enclave as described above.

d. Membrane-free compact PEMFC

Square, slightly larger than 5 cm^2 sections of anode and cathode (about 2.5 x 2.5 cm) were cut with a clean scalpel blade. Nafion ionomer as a 5 wt% solution in aliphatic alcohols was drop-casted in a single layer with a pipette onto the surface of each electrode: 65 µL were deposited on 5 cm² of the anode and 80 µL on 5 cm² of the cathode. A 15 µm thick, square 5 cm² gasket was made and inserted in-between the two electrodes in order to prevent short circuits and gas

crossover as well as define the active area. The assembly was then either pressed as described above, or simply set in the fuel cell without pressing. In either case, very weak OCVs (in the 0 to 20 mV region) were observed, indicative of short-circuits.

e. Liquid electrolyte fuel cell

The anode and cathode as described above were simply set on each side of a 10 mm thick Teflon electrolyte chamber made in house. This assembly was set in the fuel cell enclave and the chamber was filled with electrolyte (H_2SO_4 at 0.5 M in H_2O, pH = 0.3). The electrolyte was degassed with N_2 for 30 minutes before starting electrochemical measurements.

In the cases where a 25 µm thick Nafion membrane was added on either the anode or the cathode, the pressing protocol described in Chapter II was employed on the individual electrode before they were inserted in the fuel cell.

f. Stability over time and temperature of PEMFCs

Stability was assessed through CA measurements in which the temperature was controlled with a PID heating apparatus with two heating cartridges plugged into each endplate of the fuel cell.

g. Assessment of stability vs. temperature of DuBois complexes

The complex (either **CyPy** or **CyEster**) was suspended in O_2- or Ar-saturated H_2SO_4 at 0.5 M in H_2O (pH 0.3) and kept in the oven overnight at 80°C. ^{31}P NMR spectra were recorded both before and after this treatment. No significant displacement of the single peak was observed for either complex. $^{31}P[^1H]$ NMR (CD_3CN): **CyPy**, δ 3.4 ppm, s. **CyEster**, δ 6.3 ppm, s.

General conclusion

Through evolution, hydrogenase enzymes have developed gas channels as well as proton and electron relays to their active sites. With the knowledge of the requirements of a specific catalyst for turning over in ideal conditions, a proper environment can be designed in which a bio-inspired molecular catalyst can best perform. Bio-inspired synthetic chemistry and material science taken together can try to reproduce on one hand the functionality of the active site of an enzyme, and on the other an ideal matrix for this synthetic active site, yielding very promising molecular-engineered nanomaterials and presenting many catalytic possibilities for a variety of reactions.

In the continuation of research topics dear for the past ten years to what would become the SolHyCat team, bio inspired, noble metal-free molecular catalysts for hydrogen oxidation were attached onto carbon nanotubes to yield molecular engineered catalytic nanomaterials. In contrast with previous work in our group however, which focused mostly on molecular synthesis, a lot of this work was oriented towards technological aspects, such as ink formulation, materials engineering and integration in a full device. Nickel-based bis-diphosphine catalysts developed in the DuBois and Shaw groups were modified to be attached onto specifically modified carbon nanotubes, yielding very efficient molecular-engineered catalytic materials with activity for HOR and HER, occurring reversibly at the thermodynamic potential of the proton/hydrogen couple. This work aimed at further increasing performances for HOR, characterizing and finding useful activity descriptors for these new materials, and integrating them in functional noble metal-free PEMFCs.

Optimization of catalytic activity was multi-faceted. Usual strategies in our group such as increasing catalyst loading and electrode thickness were initially employed, however it soon appeared that mere increasing of site loading did not yield satisfactory increase in activity. Hence, a lot of the optimization work focused on increasing the amount of catalysts at an ideal "triple point" for catalysis, the interface of an electron, proton and gas networks. The effect of modifying the environment of the catalyst was studied by benchmarking a variety of ink formulations, deposition methods and support materials. In the carbon nanotube-based ink, in order to ensure efficient proton relay and gas diffusion, an equilibrium was found between Nafion, a proton-transport ionomer necessary for integration in fuel cells, and the carbon materials, which conduct electrons and provide gas diffusion channels. In the process of this optimization, it was found that a strong interaction between a hydrophilic catalyst and a

hydrophilic support nanotube should be preferred to other grafting strategies as it ensures stable catalyst with proper assembly of Nafion at the nano-scale to permit efficient proton transport to and from the catalytic site via the hydrophilic channels of Nafion. Furthermore, the addition of a small hydrophobic carbon component, fullerene, enhances gas diffusion to catalytic sites while retaining the proton transport properties of Nafion. This is likely due to a percolation of the hydrophobic backbone of Nafion by fullerene aggregates, yielding gas diffusion channels.

Electrochemical models are proposed to describe the catalytic behaviour of our electrodes based on supported molecular catalysts and allow for direct comparison with homogeneous catalysis and electrocatalysis. A mechanism similar to the Heyrovsky-Volmer pathway for HOR on Pt in basic media is proposed, and is coherent with the catalytic cycle of **CyArg** as determined in solution. In that sense, the descriptive gap between electro-assisted molecular catalysis and supported electrocatalysis was bridged for these systems. Intrinsic turnover frequencies for our grafted molecular catalysts are determined in different environments with the help of EIS. The grafted catalysts suffer from lower activity than in solution, in line with research on hydrogenase enzymes and coherent with previous results from our lab.

The best performing electrodes were integrated in a noble metal-free compact PEMFC, and while performance results were not up to par with that of the standalone anode and cathode, a model was proposed to calculate ideal power outputs, giving several leads for future work on optimization in PEMFCs. The most important part of this work lies probably in mastering water management and the membrane electrode assembly process.

A few important points can be taken from this work. First, one should not underestimate the importance of the environment on the performance of a grafted catalyst. The usual concerns, stability of grafting and electronic connection are of course important but not sufficient to provide a complete assessment of a grafted molecular catalyst. Second, advanced electrochemistry characterization can yield in-depth information about the limiting factors of a molecular-based catalytic material, and allow comparison to state of the art electrocatalysts. Finally, technological considerations should not be overlooked when going from the experimental setup to an integrated device.

In future work, several paths could be taken towards a better understanding, efficiency and integration of the bio-inspired catalytic materials described in this work. To complement electrochemical measurements, further techniques should be used to complete the characterization of our electrodes. A particular point of interest is the origin of synergy between fullerene and Nafion. Here, we tentatively attribute this synergy to a percolation of the PTFE side chains of Nafion by the hydrophobic fullerene but direct observation characterization is required. High resolution microscopic studies are planned on both standalone anodes and full PEMFCs within the BioPAC research program. Small-angle neutron scattering measurements are under way in collaboration with Dr Sandrine Lyonnard from SYMMES, INAC at CEA Grenoble, in order to characterize possible structuration changes of Nafion in the presence of fullerene. Alternative proton relays could be envisaged to ensure performance in compact fuel cells without the disadvantages inherent to Nafion. A molecular assembly approach could be used towards that goal. One very important parameter to understand, and the importance of which exceeds that of the electrodes presented in this work, is the reason (or reasons) behind the poor electronic connection of loaded catalytic sites. Grafting enzymes and molecular catalysts on carbon electrode materials has been shown to yield only 1 to 10 % of electronic connection, and is hence a major potential point of improvement. To improve performances in compact fuel cells, work in close collaboration between molecular chemists, materials scientists and fuel cell specialists will be critical to adapt the benchmarking environment to the new materials, especially regarding water management within the fuel cell.

Bibliography

1 Milani, B., Licini, G., Clot, E. & Albrecht, M. Small molecule activation. *Dalton Trans.* **45**, 14419-14420 (2016).

2 Helmont, J. B. v. *Ortus Medicinae*. (1648).

3 Armaroli, N. & Balzani, V. The Future of Energy Supply: Challenges and Opportunities. *Angew. Chem. Int. Ed.* **46**, 52-66 (2006).

4 Queyriaux, N., Kaeffer, N., Morozan, A., Chavarot-Kerlidou, M. & Artero, V. Molecular cathode and photocathode materials for hydrogen evolution in photoelectrochemical devices. *J. Photochem. Photobiol. C* **25**, 90-105 (2015).

5 Sealy, C. The problem with platinum. *Mater. Today* **11**, 65-68 (2008).

6 Gordon, R. B., Bertram, M. & Graedel, T. E. Metal stocks and sustainability. *Proc. Natl. Acad. Sci. USA* **103**, 1209-1214 (2006).

7 Vesborg, P. C. K. & Jaramillo, T. F. Addressing the terawatt challenge: scalability in the supply of chemical elements for renewable energy. *RSC Adv.* **2**, 7933-7947 (2012).

8 Appleby, A. J. From Sir William Grove to today: fuel cells and the future. *J. Power Sources* **29**, 3-11 (1990).

9 Winter, M. & Brodd, R. J. What Are Batteries, Fuel Cells, and Supercapacitors? *Chem. Rev.* **104**, 4245-4270 (2004).

10 Gottesfeld, S. *et al.* Anion exchange membrane fuel cells: Current status and remaining challenges. *J. Power Sources* **375**, 170-184 (2018).

11 Morozan, A., Campidelli, S., Filoramo, A., Jousselme, B. & Palacin, S. Catalytic activity of cobalt and iron phthalocyanines or porphyrins supported on different carbon nanotubes towards oxygen reduction reaction. *Carbon* **49**, 4839-4847 (2011).

12 Energy, U. S. D. o. (2017).

13 Priyadarshani, N. *et al.* Achieving Reversible H_2/H+ Interconversion at Room Temperature with Enzyme-Inspired Molecular Complexes: A Mechanistic Study. *ACS Catalysis* **6**, 6037-6049 (2016).

14 Abou Hamdan, A. *et al.* Understanding and Tuning the Catalytic Bias of Hydrogenase. *J. Am. Chem. Soc.* **134**, 8368-8371 (2012).

15 Meier, J. C. *et al.* Design criteria for stable Pt/C fuel cell catalysts. *Beilstein Journal of Nanotechnology* **5**, 44-67 (2014).

16 Costentin, C., Passard, G. & Savéant, J.-M. Benchmarking of Homogeneous Electrocatalysts: Overpotential, Turnover Frequency, Limiting Turnover Number. *J. Am. Chem. Soc.* **137**, 5461-5467 (2015).

17 Pandey, K., Islam, S. T. A., Happe, T. & Armstrong, F. A. Frequency and potential dependence of reversible electrocatalytic hydrogen interconversion by [FeFe]-hydrogenases. *Proc. Natl. Acad. Sci. USA* **114**, 3843-3848 (2017).

18 Jaouen, F. *et al.* Toward Platinum Group Metal-Free Catalysts for Hydrogen/Air Proton-Exchange Membrane Fuel Cells. *Johnson Matthey Technology Review* **62**, 231-255 (2018).

19 Steele, B. C. H. & Heinzel, A. Materials for fuel-cell technologies. *Nature* **414**, 345-352 (2001).

20 Jiao, X., Lin, C., Young, N. P., Batchelor-McAuley, C. & Compton, R. G. Hydrogen Oxidation Reaction on Platinum Nanoparticles: Understanding the Kinetics of Electrocatalytic Reactions via "Nano-Impacts". *J. Phys. Chem. C* **120**, 13148-13158 (2016).

21 Jaouen, F. *et al.* Recent advances in non-precious metal catalysis for oxygen-reduction reaction in polymer electrolyte fuel cells. *Energy Environ. Sci.* **4**, 114-130 (2011).

22 Holton, O. & Stevenson, J. The Role of Platinum in Proton Exchange Membrane Fuel Cells. *Platinum Met. Rev.* **57**, 259 (2013).

23 Zhuang, Z. *et al.* Nickel supported on nitrogen-doped carbon nanotubes as hydrogen oxidation reaction catalyst in alkaline electrolyte. *Nat. Commun.* **7**, 10141 (2016).

24 Sheng, W. *et al.* Non-precious metal electrocatalysts with high activity for hydrogen oxidation reaction in alkaline electrolytes. *Energy Environ. Sci.* **7**, 1719-1724 (2014).

25 Izhar, S., Yoshida, M. & Nagai, M. Characterization and performances of cobalt–tungsten and molybdenum–tungsten carbides as anode catalyst for PEFC. *Electrochim. Acta* **54**, 1255-1262 (2009).
26 Sheng, W., Gasteiger, H. A. & Shao-Horn, Y. Hydrogen Oxidation and Evolution Reaction Kinetics on Platinum: Acid vs Alkaline Electrolytes. *J. Electrochem. Soc.* **157**, B1529-B1536 (2010).
27 Nikolic, V. M. *et al.* On the tungsten carbide synthesis for PEM fuel cell application – Problems, challenges and advantages. *Int. J. Hydrogen Energy* **39**, 11175-11185 (2014).
28 Lubitz, W., Ogata, H., Rudiger, O. & Reijerse, E. Hydrogenases. *Chem. Rev.* **114**, 4081-4148 (2014).
29 Bachmeier, A. & Armstrong, F. Solar-driven proton and carbon dioxide reduction to fuels — lessons from metalloenzymes. *Curr. Opin. Chem. Biol.* **25**, 141-151 (2015).
30 Thauer, R. K. Hydrogenases and the Global H2 Cycle. *Eur. J. Inorg. Chem.* **2011**, 919-921.
31 Fontecilla-Camps, J. C., Volbeda, A., Cavazza, C. & Nicolet, Y. Structure/function relationships of [NiFe]- and [FeFe]-hydrogenases. *Chem. Rev.* **107**, 4273-4303 (2007).
32 Berggren, G. *et al.* Biomimetic assembly and activation of [FeFe]-hydrogenases. *Nature* **499**, 66-69 (2013).
33 Hidalgo, R., Ash, P. A., Healy, A. J. & Vincent, K. A. Infrared Spectroscopy During Electrocatalytic Turnover Reveals the Ni-L Active Site State During H2 Oxidation by a NiFe Hydrogenase. *Angew. Chem. Int. Ed.* **54**, 7110-7113 (2015).
34 Evans, R. M. *et al.* Mechanism of hydrogen activation by [NiFe] hydrogenases. *Nat. Chem. Biol.* **12**, 46-50 (2016).
35 Lubitz, W., Ogata, H., Rüdiger, O. & Reijerse, E. Hydrogenases. *Chem. Rev.* **114**, 4081-4148 (2014).
36 Adamska-Venkatesh, A. *et al.* Spectroscopic Characterization of the Bridging Amine in the Active Site of [FeFe] Hydrogenase Using Isotopologues of the H-Cluster. *J. Am. Chem. Soc.* **137**, 8998-9005 (2015).
37 Gilbert-Wilson, R. *et al.* Spectroscopic Investigations of [FeFe] Hydrogenase Maturated with [(57)Fe2(adt)(CN)2(CO)4](2.). *J. Am. Chem. Soc.* **137**, 8998-9005 (2015).
38 Pandelia, M. E., Infossi, P., Stein, M., Giudici-Orticoni, M. T. & Lubitz, W. Spectroscopic characterization of the key catalytic intermediate Ni-C in the O-2-tolerant [NiFe] hydrogenase I from Aquifex aeolicus: evidence of a weakly bound hydride. *Chem. Commun.* **48**, 823-825 (2012).
39 Foerster, S., van Gastel, M., Brecht, M. & Lubitz, W. An orientation-selected ENDOR and HYSCORE study of the Ni-C active state of Desulfovibrio vulgaris Miyazaki F hydrogenase. *J. Biol. Inorg. Chem.* **10**, 51-62 (2005).
40 Ogata, H., Nishikawa, K. & Lubitz, W. Hydrogens detected by subatomic resolution protein crystallography in a [NiFe] hydrogenase. *Nature* **520**, 571-574 (2015).
41 Fontecave, M. & Artero, V. Bioinspired catalysis at the crossroads between biology and chemistry: A remarkable example of an electrocatalytic material mimicking hydrogenases. *C. R. Chim.* **14**, 362-371 (2011).
42 Coutard, N., Kaeffer, N. & Artero, V. Molecular engineered nanomaterials for catalytic hydrogen evolution and oxidation. *Chem. Commun.* (2016).
43 Tang, H. & Hall, M. B. Biomimetics of [NiFe]-Hydrogenase: Nickel- or Iron-Centered Proton Reduction Catalysis? *J. Am. Chem. Soc.* **139**, 18065-18070 (2017).
44 Wilson, A. D. *et al.* Hydrogen Oxidation and Production Using Nickel-Based Molecular Catalysts with Positioned Proton Relays. *J. Am. Chem. Soc.* **128**, 358-366 (2006).
45 Rakowski Dubois, M. & Dubois, D. L. Development of Molecular Electrocatalysts for CO_2 Reduction and H_2 Production/Oxidation. *Acc. Chem. Res.* **42**, 1974-1982 (2009).
46 Rakowski DuBois, M. & DuBois, D. L. The roles of the first and second coordination spheres in the design of molecular catalysts for H_2 production and oxidation. *Chem. Soc. Rev.* **38**, 62-72 (2009).
47 Yang, J. Y. *et al.* Mechanistic Insights into Catalytic H2 Oxidation by Ni Complexes Containing a Diphosphine Ligand with a Positioned Amine Base. *J. Am. Chem. Soc.* **131**, 5935-5945 (2009).

48 Yang, J. Y. *et al.* Reduction of oxygen catalyzed by nickel diphosphine complexes with positioned pendant amines. *Dalton Trans.* **39**, 3001-3010 (2010).
49 Helm, M. L., Stewart, M. P., Bullock, R. M., DuBois, M. R. & DuBois, D. L. A Synthetic Nickel Electrocatalyst with a Turnover Frequency Above 100,000 s-1 for H2 Production. *Science* **333**, 863-866 (2011).
50 Kilgore, U. J. *et al.* Studies of a Series of [Ni(PR2NPh2)2(CH3CN)]2+ Complexes as Electrocatalysts for H2 Production: Substituent Variation at the Phosphorus Atom of the P2N2 Ligand. *Inorg. Chem.* **50**, 10908-10918 (2011).
51 DuBois, D. L. Development of Molecular Electrocatalysts for Energy Storage. *Inorg. Chem.* **53**, 3935-3960 (2014).
52 Dutta, A., DuBois, D. L., Roberts, J. A. S. & Shaw, W. J. Amino acid modified Ni catalyst exhibits reversible H2 oxidation/production over a broad pH range at elevated temperatures. *Proc. Natl. Acad. Sci. USA* **111**, 16286 (2014).
53 Gilbert-Wilson, R. *et al.* Spectroscopic Investigations of [FeFe] Hydrogenase Maturated with [(57)Fe2(adt)(CN)2(CO)4](2.). *Journal of the American Chemical Society* **137**, 8998-9005 (2015).
54 Le Goff, A. *et al.* From Hydrogenases to Noble Metal-Free Catalytic Nanomaterials for H-2 Production and Uptake. *Science* **326**, 1384-1387 (2009).
55 Das, A. K., Engelhard, M. H., Bullock, R. M. & Roberts, J. A. S. A Hydrogen-Evolving Ni(P2N2)2 Electrocatalyst Covalently Attached to a Glassy Carbon Electrode: Preparation, Characterization, and Catalysis. Comparisons with the Homogeneous Analogue. *Inorg. Chem.* **53**, 6875-6885 (2014).
56 Kellett, R. M. & Spiro, T. G. Cobalt porphyrin electrode films as hydrogen catalysts. *Inorg. Chem.* **24**, 2378-2382 (1985).
57 Cosnier, S., Deronzier, A. & Vlachopoulos, N. Carbon Poly(Pyrrole-[(C5me5)Rhiii(Bpy)Cl]+) Modified Electrodes - a Molecularly-Based Material for Hydrogen Evolution (Bpy = 2,2'-Bipyridine). *J. Chem. Soc., Chem. Commun.*, 1259-1261 (1989).
58 Ibrahim, S. K., Liu, X., Tard, C. & Pickett, C. J. Electropolymeric materials incorporating subsite structures related to iron-only hydrogenase: active ester functionalised poly(pyrroles) for covalent binding of {2Fe3S}-carbonyl/cyanide assemblies. *Chem. Commun.*, 1535-1537 (2007).
59 Plumeré, N. *et al.* A redox hydrogel protects hydrogenase from high-potential deactivation and oxygen damage. *Nature Chemistry* **6**, 822 (2014).
60 Tran, P. D., Artero, V. & Fontecave, M. Water electrolysis and photoelectrolysis on electrodes engineered using biological and bio-inspired molecular systems. *Energy Environ. Sci.* **3**, 727 (2010).
61 Pinson, J. & Podvorica, F. Attachment of organic layers to conductive or semiconductive surfaces by reduction of diazonium salts. *Chem. Soc. Rev.* **34**, 429-439 (2005).
62 Vijaikanth, V., Capon, J. F., Gloaguen, F., Schollhammer, P. & Talarmin, J. Chemically modified electrode based on an organometallic model of the [FeFe] hydrogenase active center. *Electrochem. Commun.* **7**, 427-430 (2005).
63 Rodriguez-Macia, P., Dutta, A., Lubitz, W., Shaw, W. J. & Rudiger, O. Direct comparison of the performance of a bio-inspired synthetic nickel catalyst and a [NiFe]-hydrogenase, both covalently attached to electrodes. *Angew. Chem. Int. Ed.* **54**, 12303-12307 (2015).
64 Elgrishi, N., Griveau, S., Chambers, M. B., Bedioui, F. & Fontecave, M. Versatile functionalization of carbon electrodes with a polypyridine ligand: metallation and electrocatalytic H(+) and CO2 reduction. *Chem. Commun.* **51**, 2995-2998 (2015).
65 Andreiadis, E. S. *et al.* Molecular engineering of a cobalt-based electrocatalytic nanomaterial for H(2) evolution under fully aqueous conditions. *Nat. Chem.* **5**, 48-53 (2013).
66 Queyriaux, N., Kaeffer, N., Morozan, A., Chavarot-Kerlidou, M. & Artero, V. Molecular cathode and photocathode materials for hydrogen evolution in photoelectrochemical devices. *J. Photochem. Photobiol. C* **25**, 90-105 (2015).
67 Le Goff, A. *et al.* Immobilization of FeFe hydrogenase mimics onto carbon and gold electrodes by controlled aryldiazonium salt reduction: An electrochemical, XPS and ATR-IR study. *Int. J. Hydrogen Energy* **35**, 10719-10724 (2010).

68 Tran, P. D. *et al.* Noncovalent modification of carbon nanotubes with pyrene-functionalized nickel complexes: carbon monoxide tolerant catalysts for hydrogen evolution and uptake. *Angew Chem Int Ed Engl* **50**, 1371-1374 (2011).
69 Goff, A. L. *et al.* Facile and tunable functionalization of carbon nanotube electrodes with ferrocene by covalent coupling and π-stacking interactions and their relevance to glucose bio-sensing. *J. Electroanal. Chem.* **641**, 57-63 (2010).
70 Jane, R. T., Tran, P. D., Andreiadis, E. S., Pécaut, J. & Artero, V. A simple method for preparation of bio-inspired nickel bisdiphosphine hydrogen-evolving catalysts. *C. R. Chimie* **18** 752-757 (2015).
71 Lalaoui, N. *et al.* A membraneless air-breathing hydrogen biofuel cell based on direct wiring of thermostable enzymes on carbon nanotube electrodes. *Chem. Commun.* **51**, 7447-7450 (2015).
72 Tran, P. D. *et al.* A noble metal-free proton-exchange membrane fuel cell based on bio-inspired molecular catalysts. *Chem. Sci.* **6**, 2050-2053 (2015).
73 Stephens, I. E. L., Rossmeisl, J. & Chorkendorff, I. Toward sustainable fuel cells. *Science* **354**, 1378-1379 (2016).
74 R. Kucernak, A. & Toyoda, E. Studying the oxygen reduction and hydrogen oxidation reactions under realistic fuel cell conditions. **10**, 1728-1731 (2008).
75 Zalitis, C. M., Sharman, J., Wright, E. & Kucernak, A. R. Properties of the hydrogen oxidation reaction on Pt/C catalysts at optimised high mass transport conditions and its relevance to the anode reaction in PEFCs and cathode reactions in electrolysers. *Electrochim. Acta* **176**, 763-776 (2015).
76 Huan, T. N. *et al.* Bio-inspired noble metal-free nanomaterials approaching platinum performances for H_2 evolution and uptake. *Energy Environ. Sci.* **9**, 940-947 (2016).
77 Durst, J., Simon, C., Hasche, F. & Gasteiger, H. A. Hydrogen Oxidation and Evolution Reaction Kinetics on Carbon Supported Pt, Ir, Rh, and Pd Electrocatalysts in Acidic Media. *J. Electrochem. Soc.* **162**, F190-F203 (2014).
78 Neyerlin, K. C., Gu, W., Jorne, J. & Gasteiger, H. A. Study of the Exchange Current Density for the Hydrogen Oxidation and Evolution Reactions. *J. Electrochem. Soc.* **154**, B631-B635 (2007).
79 Tran, P. D. *et al.* Noncovalent Modification of Carbon Nanotubes with Pyrene-Functionalized Nickel Complexes: Carbon Monoxide Tolerant Catalysts for Hydrogen Evolution and Uptake. *Angew. Chem. Int. Ed.* **50**, 1371-1374 (2011).
80 Gentil, S. *et al.* Carbon-Nanotube-Supported Bio-Inspired Nickel Catalyst and Its Integration in Hybrid Hydrogen/Air Fuel Cells. *Angew. Chem. Int. Ed.* **56**, 1845-1849 (2017).
81 Le Goff, A. *et al.* From Hydrogenases to Noble Metal-Free Catalytic Nanomaterials for H_2 Production and Uptake. *Science* **326**, 1384-1387 (2009).
82 Dutta, A., Roberts, J. A. S. & Shaw, W. J. Arginine-Containing Ligands Enhance H_2 Oxidation Catalyst Performance. *Angew. Chem. Int. Ed.* **53**, 6487-6491 (2014).
83 Chenevier, P. *et al.* Hydrogenase enzymes: Application in biofuel cells and inspiration for the design of noble-metal free catalysts for H2 oxidation. *C. R. Chim.* **16**, 491-505 (2013).
84 Hitaishi, V. *et al.* Controlling Redox Enzyme Orientation at Planar Electrodes. *Catalysts* **8**, 192 (2018).
85 Artero, V. & Fontecave, M. Solar fuels generation and molecular systems: is it homogeneous or heterogeneous catalysis? *Chem. Soc. Rev.* **42**, 2338-2356 (2013).
86 Kaeffer, N. *et al.* The Dark Side of Molecular Catalysis: Diimine–Dioxime Cobalt Complexes Are Not the Actual Hydrogen Evolution Electrocatalyst in Acidic Aqueous Solutions. *ACS Catalysis* **6**, 3727-3737 (2016).
87 Bartczak *et al. Adsorption of Ni(II) from model solutions using co-precipitated inorganic oxides*. Vol. 19 (2013).
88 Iulianelli, A. & Basile, A. Sulfonated PEEK-based polymers in PEMFC and DMFC applications: A review. *Int. J. Hydrogen Energy* **37**, 15241-15255 (2012).
89 Mauritz, K. A. & Moore, R. B. State of Understanding of Nafion. *Chem. Rev.* **104**, 4535-4586 (2004).
90 Schalenbach, M. *et al.* Gas Permeation through Nafion. Part 1: Measurements. *J. Phys. Chem. C* **119**, 25145-25155 (2015).

91 Schalenbach, M., Hoeh, M. A., Gostick, J. T., Lueke, W. & Stolten, D. Gas Permeation through Nafion. Part 2: Resistor Network Model. *J. Phys. Chem. C* **119**, 25156-25169 (2015).
92 Chlistunoff, J. & Sansiñena, J.-M. Nafion Induced Surface Confinement of Oxygen in Carbon-Supported Oxygen Reduction Catalysts. *J. Phys. Chem. C* **120**, 28038-28048 (2016).
93 Modestino, M. A., Kusoglu, A., Hexemer, A., Weber, A. Z. & Segalman, R. A. Controlling Nafion Structure and Properties via Wetting Interactions. *Macromolecules* **45**, 4681-4688 (2012).
94 Wood, D. L., Chlistunoff, J., Majewski, J. & Borup, R. L. Nafion Structural Phenomena at Platinum and Carbon Interfaces. *J. Am. Chem. Soc.* **131**, 18096-18104 (2009).
95 Maillard, F., Simonov, P. & Savinova, E. R. *Carbon materials as support for fuel cell electrocatalysts*. 429-480 (John Wiley & Sons, Inc, 2009).
96 Luo, C. *et al.* Flexible Carbon Nanotube−Polymer Composite Films with High Conductivity and Superhydrophobicity Made by Solution Process. *Nano Lett.* **8**, 4454-4458 (2008).
97 Damasceno Borges, D., Gebel, G., Franco, A. A., Malek, K. & Mossa, S. Morphology of Supported Polymer Electrolyte Ultrathin Films: A Numerical Study. *J. Phys. Chem. C* **119**, 1201-1216 (2015).
98 Mamedov, A. A. *et al.* Molecular design of strong single-wall carbon nanotube/polyelectrolyte multilayer composites. *Nat. Mater.* **1**, 190-194 (2002).
99 Shao, M., Chang, Q., Dodelet, J.-P. & Chenitz, R. Recent Advances in Electrocatalysts for Oxygen Reduction Reaction. *Chem. Rev.* **116**, 3594-3657 (2016).
100 Costentin, C., Dridi, H. & Savéant, J.-M. Molecular Catalysis of O2 Reduction by Iron Porphyrins in Water: Heterogeneous versus Homogeneous Pathways. *J. Am. Chem. Soc.* **137**, 13535-13544 (2015).
101 Iron, M. A. & Szpilman, A. M. Mechanism of the Copper/TEMPO-Catalyzed Aerobic Oxidation of Alcohols. *Chem. Eur. J.* **23**, 1368-1378 (2017).
102 Kongkanand, A. & Mathias, M. F. The Priority and Challenge of High-Power Performance of Low-Platinum Proton-Exchange Membrane Fuel Cells. *J. Phys. Chem. Lett.* **7**, 1127-1137 (2016).
103 Asset, T. *et al.* Electrochemical Stability of Pt Nanoparticles Supported on a Wide Library of Carbon Supports, Either Used Bare, or Modified By Fluorination or Tin Oxide Deposits. *Meeting Abstracts* **MA2018-01**, 1733 (2018).
104 Griveau, S., Mercier, D., Vautrinul, C. & Chausse, A. Electrochemical grafting by reduction of 4-aminoethylbenzenediazonium salt: Application to the immobilization of (bio)molecules. *Electrochem. Commun.* **9**, 2768-2773 (2007).
105 Bruno, M. & Viva, F. *Carbon Materials for Fuel Cells*. (2014).
106 Wang, X. L. *et al.* Micro-porous layer with composite carbon black for PEM fuel cells. *Electrochim. Acta* **51**, 4909-4915 (2006).
107 Damasceno Borges, D., Franco, A. A., Malek, K., Gebel, G. & Mossa, S. Inhomogeneous Transport in Model Hydrated Polymer Electrolyte Supported Ultrathin Films. *ACS Nano* **7**, 6767-6773 (2013).
108 Kraytsberg, A. & Ein-Eli, Y. Review of Advanced Materials for Proton Exchange Membrane Fuel Cells. *Energy Fuels* **28**, 7303-7330 (2014).
109 Evans, R. M. *et al.* Mechanism of hydrogen activation by [NiFe] hydrogenases. *Nat Chem Biol* **12**, 46-50 (2016).
110 Simmons, T. R., Berggren, G., Bacchi, M., Fontecave, M. & Artero, V. Mimicking hydrogenases: From biomimetics to artificial enzymes. *Coord. Chem. Rev.* **270-271**, 127-150 (2014).
111 Vermeijlen, J. J. T. T. & Janssen, L. J. J. Mass transport in a hydrogen gas diffusion electrode. *J. Appl. Electrochem.* **23**, 1237-1243 (1993).
112 Watanabe, M., Igarashi, H. & Yosioka, K. An experimental prediction of the preparation condition of Nafion-coated catalyst layers for PEFCs. *Electrochim. Acta* **40**, 329-334 (1995).
113 Watanabe, M., Igarashi, H., Uchida, H. & Hirasawa, F. Experimental analysis of water behavior in Nafion® electrolyte under fuel cell operation. *J. Electroanal. Chem.* **399**, 239-241 (1995).
114 Artero, V. Bioinspired catalytic materials for energy-relevant conversions. *Nat. Energy* **2**, 17131 (2017).

115 Izhar, S. & Nagai, M. Cobalt molybdenum carbides as anode electrocatalyst for proton exchange membrane fuel cell. *J. Power Sources* **182**, 52-60 (2008).
116 Adams, M. W. & Mortenson, L. E. The physical and catalytic properties of hydrogenase II of Clostridium pasteurianum. A comparison with hydrogenase I. *J. Biol. Chem.* **259**, 7045-7055 (1984).
117 Hexter, S. V., Grey, F., Happe, T., Climent, V. & Armstrong, F. A. Electrocatalytic mechanism of reversible hydrogen cycling by enzymes and distinctions between the major classes of hydrogenases. *Proc. Natl. Acad. Sci. USA* **109**, 11516-11521 (2012).
118 Fourmond, V. *et al.* The mechanism of inhibition by H2 of H2-evolution by hydrogenases. *Chem. Commun.* **49**, 6840-6842 (2013).
119 Vilekar, S. A., Fishtik, I. & Datta, R. Kinetics of the Hydrogen Electrode Reaction. *J. Electrochem. Soc.* **157**, B1040-B1050 (2010).
120 Zhu, Y. *et al.* High-efficiency electrochemical hydrogen evolution based on the intermetallic Pt2Si compound prepared by magnetron-sputtering. *RSC Advances* **7**, 1553-1560 (2017).
121 Costentin, C., Drouet, S., Robert, M. & Savéant, J.-M. Turnover Numbers, Turnover Frequencies, and Overpotential in Molecular Catalysis of Electrochemical Reactions. Cyclic Voltammetry and Preparative-Scale Electrolysis. *J. Am. Chem. Soc.* **134**, 11235-11242 (2012).
122 Costentin, C., Drouet, S., Robert, M. & Saveant, J. M. A Local Proton Source Enhances CO2 Electroreduction to CO by a Molecular Fe Catalyst. *Science* **338**, 90-94 (2012).
123 Andrieux, C. P., Costentin, C., Di Giovanni, C., Savéant, J.-M. & Tard, C. Conductive Mesoporous Catalytic Films. Current Distortion and Performance Degradation by Dual-Phase Ohmic Drop Effects. Analysis and Remedies. *J. Phys. Chem. C* **120**, 21263-21271 (2016).
124 Park, S.-M. & Yoo, J.-S. Peer Reviewed: Electrochemical Impedance Spectroscopy for Better Electrochemical Measurements. *Anal. Chem.* **75**, 455 A-461 A (2003).
125 Boukamp, B. A. & Bouwmeester, H. J. M. Interpretation of the Gerischer impedance in solid state ionics. *Solid State Ionics* **157**, 29-33 (2003).
126 González-Cuenca, M., Zipprich, W., Boukamp, B. A., Pudmich, G. & Tietz, F. Impedance Studies on Chromite-Titanate Porous Electrodes under Reducing Conditions. *Fuel Cells* **1**, 256-264 (2002).
127 Singh, R. K., Devivaraprasad, R., Kar, T., Chakraborty, A. & Neergat, M. Electrochemical Impedance Spectroscopy of Oxygen Reduction Reaction (ORR) in a Rotating Disk Electrode Configuration: Effect of Ionomer Content and Carbon-Support. *J. Electrochem. Soc.* **162**, F489-F498 (2015).
128 Hidalgo, R., Ash, P. A., Healy, A. J. & Vincent, K. A. Infrared Spectroscopy During Electrocatalytic Turnover Reveals the Ni-L Active Site State During H2 Oxidation by a NiFe Hydrogenase. *Angew. Chem. Int. Ed.* **54**, 7110-7113 (2015).
129 Ash, P. A. *et al.* Electrochemical and Infrared Spectroscopic Studies Provide Insight into Reactions of the NiFe Regulatory Hydrogenase fromRalstonia eutrophawith O2and CO. *J. Phys. Chem. B* **119**, 13807-13815 (2015).
130 Shaw, W. J., Helm, M. L. & DuBois, D. L. A modular, energy-based approach to the development of nickel containing molecular electrocatalysts for hydrogen production and oxidation. *Biochim. Biophys. Acta Bioenerg.* **1827**, 1123-1139 (2013).
131 Morozan, A., Jegou, P., Jousselme, B. & Palacin, S. Electrochemical performance of annealed cobalt-benzotriazole/CNTs catalysts towards the oxygen reduction reaction. *Phys. Chem. Chem. Phys.* **13**, 21600-21607 (2011).
132 Morozan, A., Jousselme, B. & Palacin, S. Low-platinum and platinum-free catalysts for the oxygen reduction reaction at fuel cell cathodes. *Energy Environ. Sci.* **4**, 1238-1254 (2011).
133 Danzer, M. A., Wittmann, S. J. & Hofer, E. P. Prevention of fuel cell starvation by model predictive control of pressure, excess ratio, and current. *J. Power Sources* **190**, 86-91 (2009).
134 Herrera, O. E., Wilkinson, D. P. & Mérida, W. Anode and cathode overpotentials and temperature profiles in a PEMFC. *J. Power Sources* **198**, 132-142 (2012).
135 Orfanidi, A. *et al.* The Key to High Performance Low Pt Loaded Electrodes. *J. Electrochem. Soc.* **164**, F418-F426 (2017).
136 Yuan, X.-Z., Sun, J. C., Wang, H. & Li, H. Accelerated conditioning for a proton exchange membrane fuel cell. *J. Power Sources* **205**, 340-344 (2012).

137 Klingele, M., Breitwieser, M., Zengerle, R. & Thiele, S. Direct deposition of proton exchange membranes enabling high performance hydrogen fuel cells. *J. Mater. Chem. A* **3**, 11239-11245 (2015).
138 Zitolo, A. *et al.* Identification of catalytic sites for oxygen reduction in iron- and nitrogen-doped graphene materials. *Nat. Mater.* **14**, 937 (2015).
139 Oughli, A. A. *et al.* Dual properties of a hydrogen oxidation Ni-catalyst entrapped within a polymer promote self-defense against oxygen. *Nat. Commun.* **9**, 864 (2018).

Annex to Chapter I

Ni-K pre-edge positions for each XAS sample

	Edge position	**Oxidation number**
CyEster P4	8342,75 eV	1,6
CyEster P2	8343,55 eV	2,1
CyEster grafted	8343,94 eV	2,3
CyEster after turnover	8344,14 eV	2,4
CyArg	8342,87 eV	1,7
CyArg grafted	8343,38 eV	2,0
CyArg after turnover	8343,60 eV	2,1

Fits of reference spectra

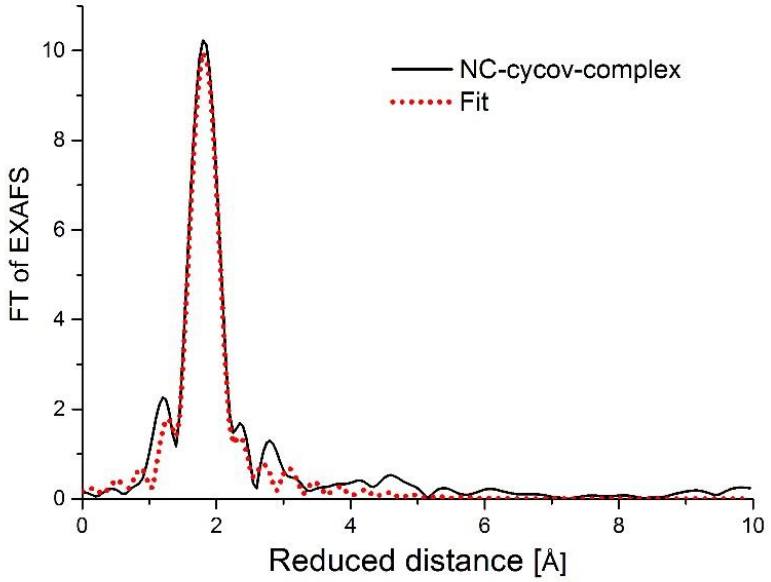

Fourier transform (FT) of experimental EXAFS-spectra of CyEster P4 with the respective fit by curve simulations.

CyEster P4		
#	Ni-P	R_f
R [Å]	2.215 (4)	13.5%

N	4.2 (3)	
σ [Å]	0.0068 (10)	

Fit results for the EXAFS-spectrum of NC-cycov-complex. ΔE0 = 1.32, S02=0.76

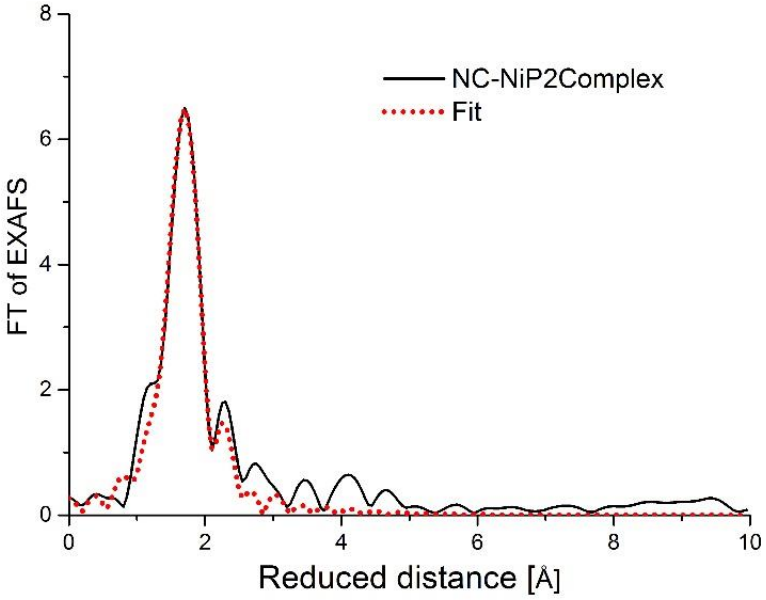

Fourier transform (FT) of experimental EXAFS-spectra of CyEster P2 with the respective fit by curve simulations.

CyEster P2				
#	Ni-O	Ni-P	Ni-N	R_f
R [Å]	1.90 (3)	2.18 (2)	2.68 (4)	17.8%
N	1.3 (4)	1.8 (6)	1,0 (6)	
σ [Å]	0.004 (4)	0.004*	0.004*	

Fit results for the EXAFS-spectrum of NC-NiP2-complex. ΔE0 = -1.35, $S0^2$=0.76.

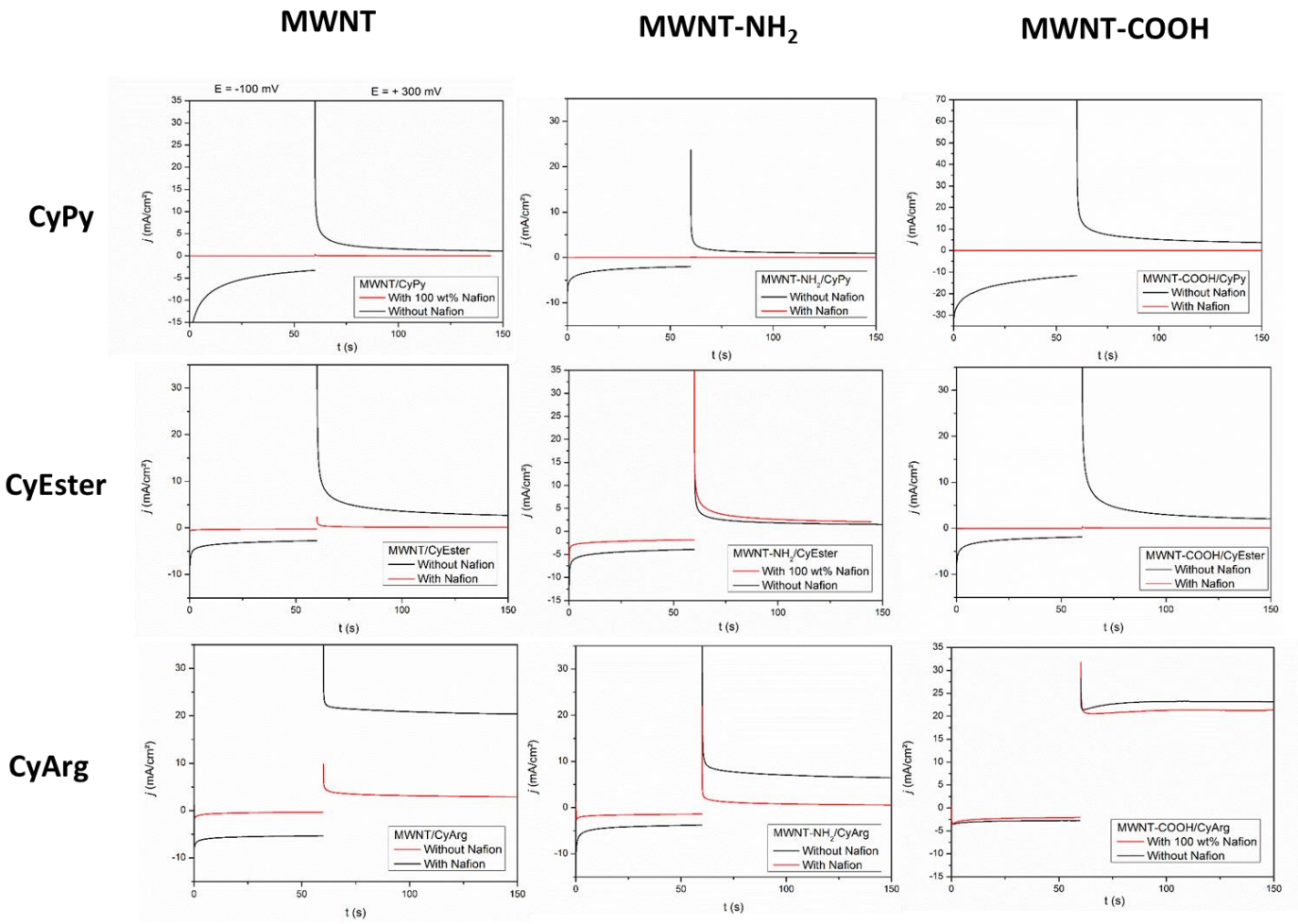

Annex to Table 5: Effect of Nafion addition on HOR for 9 different nanotube/catalyst pairs. Half-cell setup, S = 0.063 cm², electrolyte is H_2SO_4 0.5 M in H_2O, pH 0.3, 298K and P_{H2} = 1 atm. Electrode is first poised at -100 mV vs. SHE to trigger HER, then at +300 mV to trigger HOR.

Annex to Chapter III

EIS fit values for Nafion-containing electrodes

In red, data for which E_{IRcorr} is negative or below the modulation amplitude of the modulation signal. R_G ant t_G are averaged and fixed.

E (mV)	R1 (Ω)	RG1 (Ω)	tG1 (s)	C2 (mF)	R2 (Ω)	I (mA)	IR (mV)	Eircorr (mV)
2	200	372	0.36	2.8	44	0.012	2.4	-0.4
5	200	399	0.36	3.5	50	0.016	3.2	1.8
10	200	384	0.36	2.5	72	0.021	4.2	5.8
20	200	373	0.36	2.3	54	0.034	6.8	13.2
30	200	348	0.36	1.7	57	0.046	9.2	20.8
50	200	308	0.36	1	58	0.075	15	35
100	200	334	0.36	1.4	56	0.147	29.4	70.6
150	200	316	0.36	0.9	109	0.215	43	107
200	200	282	0.36	0.7	187	0.28	56	144
250	200	242	0.36	0.6	280	0.33	66	184

EIS fit values for MWNT-COOH/CyArg + Nafion electrode. Half-cell setup, S = 0.063 cm², electrolyte is H_2SO_4 0.5 M in H_2O, pH 0.3, 298K and P_{H2} = 1 atm.

E (mV)	R1 (Ω)	RG1 (Ω)	tG1 (s)	C2 (mF)	R2 (Ω)	I (mA)	IR (mV)	Eircorr (mV)
2	92	252	0.36	N/A	N/A	0.0085	0.782	1.218
5	92	190	0.36	10	27	0.0185	1.702	3.298
10	92	176	0.36	8.4	25	0.033	3.036	6.964
20	92	158	0.36	4.8	20	0.065	5.98	14.02
30	92	144	0.36	3.3	18	0.095	8.74	21.26
50	92	109	0.36	1.4	26	0.175	16.1	33.9
100	92	98	0.36	1.1	28	0.375	34.5	65.5
150	92	99	0.36	1.2	40	0.575	52.9	97.1
200	92	109	0.36	1.3	60	0.725	66.7	133.3
250	92	105	0.36	1.2	97	0.825	75.9	174.1

EIS fit values for MWNT-COOH/CyArg + Nafion + fullerene electrode. Half-cell setup, S = 0.063 cm², electrolyte is H_2SO_4 0.5 M in H_2O, pH 0.3, 298K and P_{H2} = 1 atm.

EIS fit values for Nafion-free electrodes

In red, data for which E_{IRcorr} is negative or below the modulation amplitude of the modulation signal. R_G ant t_G are averaged and fixed.

E (mV)	R1 (Ω)	RG1 (Ω)	tG1 (s)	C2 (mF)	R2 (Ω)	I (mA)	IR (mV)	Eircorr (mV)
2	50	170	0.24	2.6	28	0.01	0.5	1.5
5	50	167	0.24	2.4	38	0.02	1	4
10	50	160	0.24	2.6	34	0.038	1.9	8.1
20	50	159	0.24	3.3	19	0.077	3.85	16.15
30	50	145	0.24	3	15	0.1175	5.875	24.125
50	50	145	0.24	2.7	1	0.206	10.3	39.7
100	50	146	0.24	2.8	69	0.425	21.25	78.75
150	50	162	0.24	1.1	280	0.55	27.5	122.5
200	50	148	0.24	0.9	690	0.62	31	169
250	50	132	0.24	0.5	1150	0.64	32	218

EIS fit values for MWNT-COOH/CyArg electrode. Half-cell setup, S = 0.063 cm², electrolyte is H_2SO_4 0.5 M in H_2O, pH 0.3, 298K and P_{H2} = 1 atm.

E (mV)	R1 (Ω)	RG1 (Ω)	tG1 (s)	C2 (mF)	R2 (Ω)	I (mA)	IR (mV)	Eircorr (mV)
2	57	140	0.24	N/A	N/A	0.04	2.28	-0.28
5	57	142	0.24	177	32	0.05	2.85	2.15
10	57	137	0.24	120	13	0.075	4.275	5.725
20	57	121	0.24	155	13	0.12	6.84	13.16
30	57	110	0.24	124	11	0.175	9.975	20.025
50	57	92	0.24	58	11	0.28	15.96	34.04
100	57	79	0.24	8	37	0.6	34.2	65.8
150	57	84	0.24	1.8	145	0.825	47.025	102.975
200	57	68	0.24	0.9	441	0.925	52.725	147.275
250	57	68	0.24	0.8	850	0.975	55.575	194.425

EIS fit values for MWNT-COOH/CyArg + fullerene electrode. Half-cell setup, S = 0.063 cm², electrolyte is H_2SO_4 0.5 M in H_2O, pH 0.3, 298K and P_{H2} = 1 atm.

Abstract

The use of new energy vectors as alternatives to the fossil and nuclear fuels is necessary for the transition to renewable energies. These intermittent energy sources can be stored in fuels, such as hydrogen gas which stands out for its energy density and participation in the virtuous water splitting cycle. Controlled H_2 oxidation can be done in so-called fuel cells, which oxidize hydrogen at the anode and reduce oxygen at the cathode to produce electrical power, with water and heat as the sole by-products of the reaction. Those mature technologies employ platinum group metals as catalysts at both the anode and cathode. However, as worldwide energy demands keep increasing, these limited resources will not be sufficient for a worldwide adoption of H_2 as an energy vector. In this work, materials containing noble metal-free, bio-inspired catalysts for H_2 oxidation are optimized and integrated in functional fuel cells. Their behaviour in technologically-relevant conditions is studied and compared to that of state of the art platinum catalysts. The best-performing materials are thoroughly characterized with various advanced electrochemistry techniques, yielding leads for further optimization as well as insight on the benchmarking of novel catalytic materials.

Résumé

L'utilisation de nouveaux vecteurs énergétiques comme alternative aux combustibles fossiles et nucléaires est nécessaire pour la transition énergétique. Ces sources d'énergie intermittentes peuvent être stockées dans des carburants, tels que le dihydrogène (H_2) qui se distingue par sa densité énergétique. L'oxydation contrôlée de H_2 peut être effectuée dans des piles à combustible, qui oxydent l'hydrogène à l'anode et réduisent l'oxygène à la cathode et fournissent de l'énergie électrique, formant pour seuls sous-produits de la réaction de l'eau et de la chaleur. Ces technologies, matures, emploient des métaux du groupe du platine en tant que catalyseurs à l'anode et à la cathode. Cependant, alors que les demandes énergétiques mondiales ne cessent d'augmenter, les ressources limitées en métaux nobles ne seront pas suffisantes pour une adoption mondiale de l'hydrogène comme vecteur énergétique. Dans ce travail, des matériaux contenant des catalyseurs bio-inspirés et sans métaux nobles pour l'oxydation de H_2 sont optimisés et intégrés dans des piles à combustible fonctionnelles. Leur comportement en conditions technologiques est étudié et comparé à celui de l'état de l'art des catalyseurs au platine. Les matériaux les plus performants sont caractérisés en détail par diverses techniques, donnant des pistes pour une optimisation future ainsi qu'un aperçu de ce que requièrent les tests de performance de nouveaux matériaux catalytiques.